nature portfolio

https://doi.org/10.1038/s41560-021-00962-y

Supplementary information

Rational solvent molecule tuning for high-performance lithium metal battery electrolytes

In the format provided by the authors and unedited

Supplementary Information

Rational solvent molecule tuning for high-performance lithium metal battery electrolytes

Zhiao Yu,[1,2] Paul E. Rudnicki,[1] Zewen Zhang,[3] Zhuojun Huang,[3] Hasan Celik,[4] Solomon T. Oyakhire,[1] Yuelang Chen,[1,2] Xian Kong,[1] Sang Cheol Kim,[3] Xin Xiao,[3] Hansen Wang,[3] Yu Zheng,[1,2] Gaurav A. Kamat,[1] Mun Sek Kim,[1,3] Stacey F. Bent,[1] Jian Qin,[1,*] Yi Cui,[3,5,*] and Zhenan Bao[1,*]

[1]Department of Chemical Engineering and [2]Department of Chemistry, Stanford University, Stanford, CA 94305, USA. [3]Department of Materials Science and Engineering, Stanford University, Stanford, CA 94305, USA. [4]College of Chemistry Nuclear Magnetic Resonance Facility (CoC-NMR), University of California, Berkeley, CA 94720, USA. [5]Stanford Institute for Materials and Energy Sciences, SLAC National Accelerator Laboratory, Menlo Park, CA 94025, USA.

*Corresponding author e-mails: jianq@stanford.edu; yicui@stanford.edu; zbao@stanford.edu.

Supplementary Tables 1-5, Figures 1-66, References 1-31.

1. Supplementary Tables

Supplementary Table 1. Physicochemical properties of developed solvents and electrolytes.

	DEE	F3DEE	F6DEE	F4DEE	F5DEE
Molecular weight ($g\ mol^{-1}$)	118.17	172.15	226.12	190.14	208.13
Density ($g\ mL^{-1}$)	0.842	1.07	1.40	1.24	1.29
Boiling point at ~1 kPa (°C)	<20	~40	~40	~60	~60
Boiling point at 1 atm (°C)*	122	~161	~161	~186	~186
Closed-cup flash point (°C)	<25	31	63	>70	60-70

	1.2 M LiFSI/ DEE	1.2 M LiFSI/ F3DEE	1.2 M LiFSI/ F6DEE	1.2 M LiFSI/ F4DEE	1.2 M LiFSI/ F5DEE
Density ($g\ mL^{-1}$)	0.972	1.21	1.54	1.38	1.42
Viscosity (cp at 25 °C)	1.46	2.21	3.61	6.97	3.39
Conductivity ($mS\ cm^{-1}$) without separator	11.0±0.5	6.18±0.04	4.48±0.21	4.76±0.007	5.01±0.09
Conductivity ($mS\ cm^{-1}$) with swelled Celgard separator	0.336±0.006	0.166±0.011	0.045±0.0004	0.178±0.014	0.101±0.002
LTN**	0.223	0.316	0.483	0.234	0.398
Li^+ conductivity ($mS\ cm^{-1}$) = conductivity without separator × LTN	2.45	1.95	2.16	1.11	1.99

* Boiling points at 1 atm were estimated from those under vacuum using Sigma-Aldrich Pressure-Temperature Nomograph Interactive Tool (https://www.sigmaaldrich.com/chemistry/solvents/learning-center/nomograph.html?gclid=CjwKCAjw9r-DBhBxEiwA9qYUpctOuvLP40XzFVLCoWHjYl6vEho6xQ1V2uNm3QzJUdEsakSbSvpuOxoCsFoQAvD_BwE).

** LTN: Li^+ transference number measured using Li || Li symmetric cells under potentiostatic polarization[1].

Supplementary Table 2. Fitting and calculation results from DOSY NMR[2,3].

Solution	$D_{toluene}$*	D_{FDMB}*	D_{Li+}*	α_{FDMB}	Coordinating solvent number**
FDMB	12.37	8.810	N/A	N/A	N/A
1 M LiFSI/FDMB	7.049	4.060	1.613	0.281	**1.77**

Solution	$D_{toluene}$*	D_{DEE}*	D_{Li+}*	α_{DEE}	Coordinating solvent number**
DEE	24.87	21.20	N/A	N/A	N/A
1.2 M LiFSI/DEE	11.86	8.269	3.511	0.306	**2.20**

Solution	$D_{toluene}$*	D_{F3DEE}*	D_{Li+}*	α_{F3DEE}	Coordinating solvent number**
F3DEE	20.26	14.94	N/A	N/A	N/A
1.2 M LiFSI/F3DEE	10.18	5.830	2.770	0.354	**2.19**

Solution	$D_{toluene}$*	D_{F6DEE}*	D_{Li+}*	α_{F6DEE}	Coordinating solvent number**
F6DEE	15.29	9.779	N/A	N/A	N/A
1.2 M LiFSI/F6DEE	8.239	4.280	1.361	0.253	**1.57**

Solution	$D_{toluene}$*	D_{F4DEE}*	D_{Li+}*	α_{F4DEE}	Coordinating solvent number**
F4DEE	9.028	5.765	N/A	N/A	N/A
1.2 M LiFSI/F4DEE	4.290	2.193	1.122	0.337	**2.20**

Solution	$D_{toluene}$*	D_{F5DEE}*	D_{Li+}*	α_{F5DEE}	Coordinating solvent number**
F5DEE	12.06	8.035	N/A	N/A	N/A
1.2 M LiFSI/F5DEE	6.098	3.137	1.289	0.333	**2.06**

* Diffusion coefficients are in the unit of 10^{-6} cm^2 s^{-1}.

** Coordinating solvent number was calculated by multiplying the coordination ratio (α) with the molar number of the solvent.

Supplementary Table 3. Information about industrial pouch cells.

Information	Cu || single-crystal NMC532	Cu || micro-LFP	Li || poly-crystal NMC811
Cu foil thickness	8 μm Cu	7 μm Cu with 1 μm carbon coating	No Cu current collector, Pristine 50 μm free-standing Li foil towards double-sided NMC811
Al foil thickness	12 μm		
Separator thickness	12 μm thick PE coated with alumina		
Package foil thickness	~80 μm		
Active material : Carbon : Binder	94.0 : 4.0 : 2.0	96.7 : 1.5 : 1.8	95.5 : 2.7 : 1.8
Areal capacity*	~3.1 mAh cm^{-2}	~2.1 mAh cm^{-2}	3.8 mAh cm^{-2}
Total capacity*	200 mAh (0.3C discharge)	210 mAh (0.3C discharge) 170 mAh (2C discharge)	120 mAh (0.5C discharge)
Electrolyte/Cathode ratio (E/C, g Ah^{-1})	2.4	2.4	2.5
External temperature	Uncontrolled room temperature (18-25 ºC)		
Pressure	~1000 kPa		

* The capacities were based on the corresponding cycling ranges: Cu || NMC532: 3.0-4.4 V; Cu || LFP: 2.5-3.8 V; Li || NMC811: 2.8-4.4 V.

Supplementary Table 4. Comparison of the state-of-the-art high-voltage Li metal full battery performances.

Electrolyte	Electrolyte Amount	Cell Condition	Cycling Condition & Capacity Retention
7 M LiFSI in FEC (ref.[4])	Not mentioned	2.5 mAh cm^{-2} Li || 1.83 mAh cm^{-2} LNMO N/P = 1.37	70% after 140 cycles
1LiFSI-3TMS-3TTE (ref.[5])	40 mL Ah^{-1}	50 μm Li || 1.5 mAh cm^{-2} NMC111 N/P = 6.67	C/3 cycling, 80% after 300 cycles
1.2 M LiFSI/DMC-BTFE (ref.[6])	80 mL Ah^{-1}	450 μm Li || 2 mAh cm^{-2} NMC111 N/P = 45	0.5C charge 2C discharge, 80% after 700 cycles
1 M $LiPF_6$/FEC-FEMC-HFE (ref.[7])	50 g Ah^{-1}	2 mAh cm^{-2} Li || 2 mAh cm^{-2} NMC811 coin cell N/P = 1	C/2 cycling, 95% after 120 cycles
1LiFSI-1.2DME-3TTE (ref.[8])	3 g Ah^{-1}	50 μm Li || ~4.2 mAh cm^{-2} NMC811 coin cell N/P = 2.38	C/3 cycling, 80% after 155 cycles
1M LiFSI/DME/TFEO (ref.[9])	50 g Ah^{-1}	50 μm Li || ~1.5 mAh cm^{-2} NMC811 coin cell N/P = 6.67	C/3 cycling, 80% after 300 cycles
1LiFSI-1.3DME-2TFEO (ref.[10])	~4.5 g Ah^{-1}	50 μm Li || ~4.2 mAh cm^{-2} NMC811 coin cell N/P = 2.38	0.1C charge 0.3C discharge, 80% after ~210 cycles
1 M LiFSI/FSA (ref.[11])	25 mL Ah^{-1}	60 μm Li || 1.6 mAh cm^{-2} NMC622 N/P = 7.5	89% after 200 cycles
1 m LiFSI in DMTMSA (ref.[12])	~12 mL Ah^{-1}	60 μm Li || ~1.7 mAh cm^{-2} NMC811 N/P = 7.06	4.7 V, 0.5C cycling, 88% after 100 cycles
1 M $LiPF_6$/EC-DEC with 10 mM $In(OTf)_3$ and 0.5 M $LiNO_3$ (ref.[13])	8.4 g Ah^{-1}	50 μm Li || ~4.3 mAh cm^{-2} NMC811 coin cell N/P = 2.33	0.3C charge 0.5C discharge, 80% after 160 cycles
1 M $LiPF_6$/FEC-EMC with 3 wt% $LiNO_3$ and 1 wt% TPFPB (ref.[14])	3.4 g Ah^{-1}	50 μm Li || ~3.4 mAh cm^{-2} NMC811 coin cell N/P = 2.94	0.1C charge 0.3C discharge, 80% after 140 cycles

1 M LiFSI/FDMB (ref.[1])	~6 g Ah^{-1}	20 µm Li || 1.6 mAh cm^{-2} NMC532 coin cell N/P = 2.5	C/3 cycling, 100% after 210 cycles
This work: **1.2 M LiFSI/F3DEE** **1.2 M LiFSI/F6DEE** **1.2 M LiFSI/F4DEE** **1.2 M LiFSI/F5DEE**	**~2.5 g Ah^{-1}**	**25 µm Li || 3.8 mAh cm^{-2}** **NMC811 industrial pouch cells** **N/P = 1.32**	**0.2C charge 0.5C discharge** **F3DEE, 80% after 135 cycles** **F6DEE, 80% after 110 cycles** **F4DEE, 80% after 105 cycles** **F5DEE, 85% after 150 cycles**
This work: **1.2 M LiFSI/F3DEE** **1.2 M LiFSI/F6DEE** **1.2 M LiFSI/F4DEE** **1.2 M LiFSI/F5DEE**	**~8 g Ah^{-1}**	**50 µm Li || 4.9 mAh cm^{-2}** **NMC811 coin cells** **N/P = 2.04**	**0.2C charge 0.3C discharge** **F3DEE, 80% after 125 cycles** **F6DEE, 80% after 130 cycles** **F4DEE, 80% after 180 cycles** **F5DEE, 80% after >200 cycles**
This work: **1.2 M LiFSI/F4DEE** **1.2 M LiFSI/F5DEE**	**~8 g Ah^{-1}**	**50 µm Li || 4.9 mAh cm^{-2}** **NMC811 coin cells** **N/P = 2.04**	**0.1C charge 0.3C discharge** **F4DEE, 80% after 180 cycles** **F5DEE, 80% after 270 cycles**

Supplementary Table 5. Comparison of anode-free Li metal battery (zero Li excess) performances.

Electrolyte	Electrolyte Amount	Cell Condition	Cycling Condition & Capacity Retention
4 M LiFSI in DME (ref.[15])	~44 g Ah^{-1}	Cu || LFP coin cell, 1.71 mAh cm^{-2}	~C/8 charge/discharge, 60% after 50 cycles
1 M LiTFSI + 2 M LiFSI + 3 wt% $LiNO_3$ in DME/DOL (ref.[16])	Not mentioned	Cu || LFP coin cell, 0.85 mAh cm^{-2}	39% after 100 cycles
1.7 M LiFSI in MeTHF/TTE (ref.[17])	4.0 g Ah^{-1}	Cu || LFP pouch cell, 2.7 mAh cm^{-2}, 560 mAh	0.3C charge 0.5C discharge, 41.6% after 150 cycles
7 M LiFSI in FEC (ref.[4])	Not mentioned	Cu || LNMO coin cell, 1.43 mAh cm^{-2}	54% after 50 cycles
2 M $LiPF_6$ in EC/DEC + 50% FEC (ref.[18])	Not mentioned	Cu || NMC111 coin cell, ~1.6 mAh cm^{-2}	~C/8 charge/discharge, 40% after 50 cycles
1 M $LiPF_6$ in FEC/FEMC/HFE (ref.[7])	~47 g Ah^{-1}	Cu || NMC811 coin cell, ~2.0 mAh cm^{-2}	~C/4 charge/discharge, 50% after 30 cycles
1LiFSI-1.2DME-3TTE (ref.[8])	3 g Ah^{-1}	Cu || NMC811 coin cell, ~4.2 mAh cm^{-2}	C/10 charge C/3 discharge, 77% after 70 cycles
0.6 or 1 M LiDFOB + 0.6 or 0.2 M $LiBF_4$ in FEC/DEC (ref.[19])	~2 g Ah^{-1}	Cu || NMC532 pouch cell, ~245 mAh	~80% DOD (depth of discharge), C/5 charge C/2 discharge, 40 ^oC, 80% after 80 or 90 cycles (low pressure)
High concentration, 1.8 M LiDFOB + 0.4 M $LiBF_4$ in FEC/DEC (ref.[20])	~2 g Ah^{-1}	Cu || NMC532 pouch cell, ~210 mAh	~70% DOD, C/5 charge C/2 discharge, 40 ^oC hot formation, 80% after 90 cycles (low pressure) / 80% after 195 cycles (high pressure)
0.6 M LiDFOB + 0.6 M $LiBF_4$ in FEC/DEC (ref.[20])	~2 g Ah^{-1}	Cu || NMC532 pouch cell, ~210 mAh	~70% DOD, C/5 charge C/2 discharge, controlled 20 ^oC, 80% after ~16 cycles (low pressure) / 80% after 50-60 cycles (high pressure)

High concentration, 2.0 M LiDFOB and 1.4 M $LiBF_4$ in FEC/DEC (ref.[21])	~2.6 g Ah^{-1}	Cu || NMC532 pouch cell, ~210 mAh	~70% DOD, C/5 charge C/2 discharge, controlled 20 °C, 80% after 200 cycles (high pressure)
1 m LiFSI in N,N-dimethyltrifluoromethane-sulfonamide (DMTMSA) (ref.[12])	~3 g Ah^{-1}	Cu || NMC811 coin cell, 4.5 mAh cm^{-2}	100% DOD (3-4.5 V), C/10 charge C/3 discharge, 73% after 65 cycles
1 M LiFSI/FDMB (ref.[1])	~2 g Ah^{-1}	Cu || NMC532, Cu || NMC622, and Cu || NMC811 pouch cells, 200-250 mAh	100% DOD, C/5 charge C/3 discharge, uncontrolled room temperature (18-25 °C), 80% after 100 cycles (low pressure)
This work: **1.2 M LiFSI/F4DEE** **1.2 M LiFSI/F5DEE**	**~2.4 g Ah^{-1}**	**Cu || micro-LFP pouch cells that have never been tried in the field, ~170 mAh at 2C discharge**	**Fast cycling:** **100% DOD, uncontrolled room temperature (18-25 °C),** **0.2C charge 2C discharge, 80% after 140 cycles (high pressure) /** **0.5C charge 2C discharge, 80% after 110 cycles (high pressure) /** **1C charge 2C discharge, 80% after 90 cycles (high pressure)**

2. Supplementary Figures

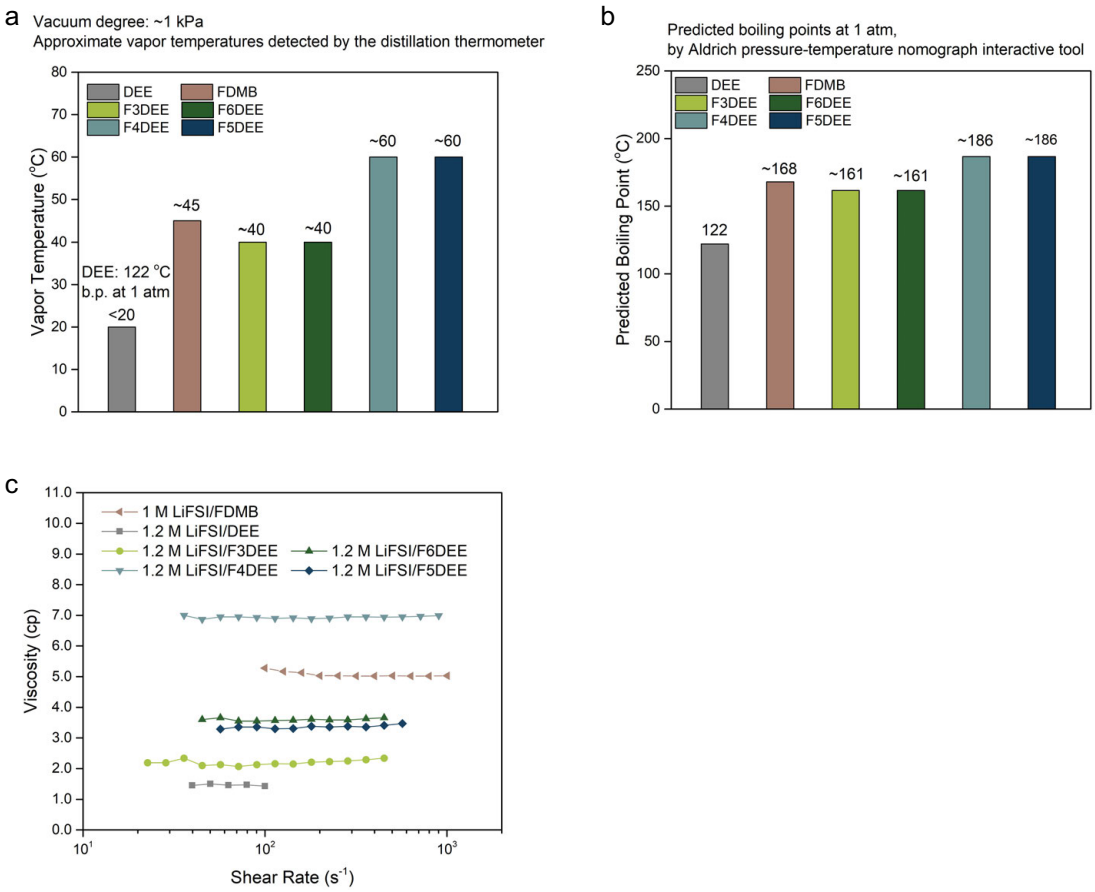

Supplementary Fig. 1. (a,b) Boiling points of synthesized fluorinated-DEEs: vapor temperatures measured during vacuum distillation (a) and estimated boiling points at 1 atm (b). (c) Viscosities of 1.2 M LiFSI in fluorinated-DEEs versus shear rate, measured by rheology.

Note: The same as those in Supplementary Table 1, boiling points at 1 atm were estimated from those under vacuum using Sigma-Aldrich Pressure-Temperature Nomograph Interactive Tool (https://www.sigmaaldrich.com/chemistry/solvents/learning-center/nomograph.html?gclid=CjwKCAjw9r-DBhBxEiwA9qYUpctOuvLP40XzFVLCoWHjYl6vEho6xQ1V2uNm3QzJUdEsakSbSvpuOxoCsFoQAvD_BwE).

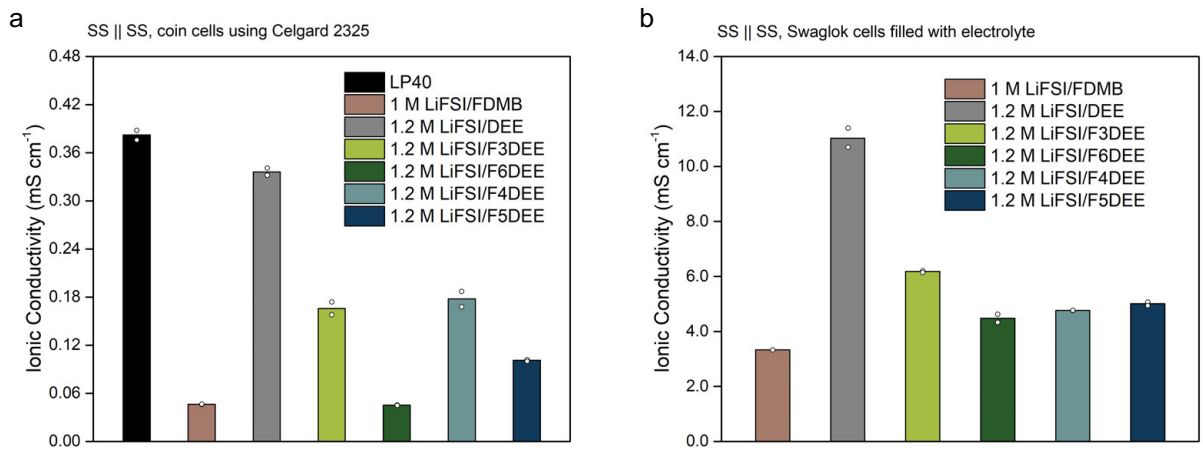

Supplementary Fig. 2. Ionic conductivities of developed electrolytes and control electrolytes measured with (a) and without (b) Celgard 2325 separators. Each bar stands for the mean of two replicated ion conductivity measurements and every single measurement is shown with hollow dots.

Note: Swagelok cells measure the conductivities of pure electrolyte liquids without separator, while coin cells measure the Celgard 2325 separators swelled by the electrolytes. The latter ones mimic the situation in realistic cells. The 1 M LiFSI/FDMB data in (b) was extracted from ref.[1]. From (a), we can see that the ion conductivity of 1.2 M LiFSI/DEE is similar to that of LP40 (1 M $LiPF_6$ in EC/DEC [1/1]) electrolyte, while that of F3DEE or F4DEE was as ~60% high as the DEE one. The conductivity of 1.2 M LiFSI/F5DEE was ~40% that of 1.2 M LiFSI/DEE, but 1.2 M LiFSI/F6DEE and 1 M LiFSI/FDMB were similarly low.

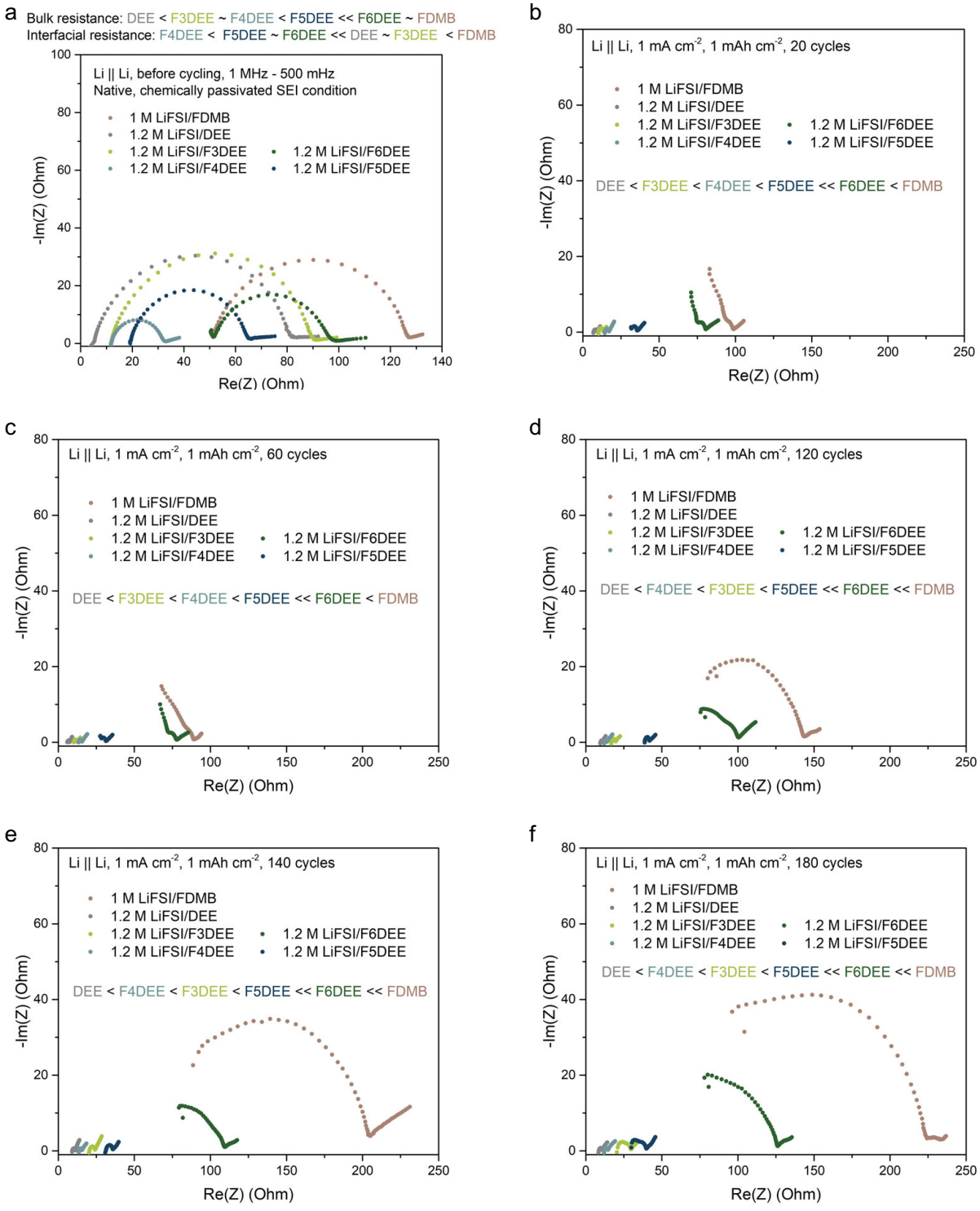

Supplementary Fig. 3. EIS plots of Li || Li symmetric cells with cycling: before cycling (a), and after 20 cycles (b), 60 cycles (c), 120 cycles (d), 140 cycles (e), 180 cycles (f).

Note: Generally, the impedance evolution of Li || Li cells with cycling follows the overpotential trend. The overall impedances of DEE, F3DEE, F4DEE, and F5DEE cells were maintained to be low, while those of F6DEE and FDMB cells increased vastly with cycling.

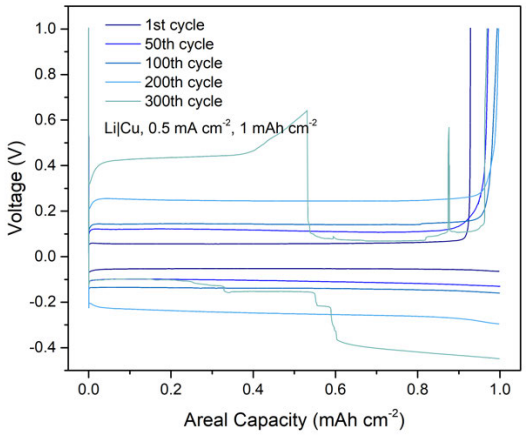

Supplementary Fig. 4. Voltage profiles of Li || Cu half cell using 1 M LiFSI/FDMB at different cycle numbers.

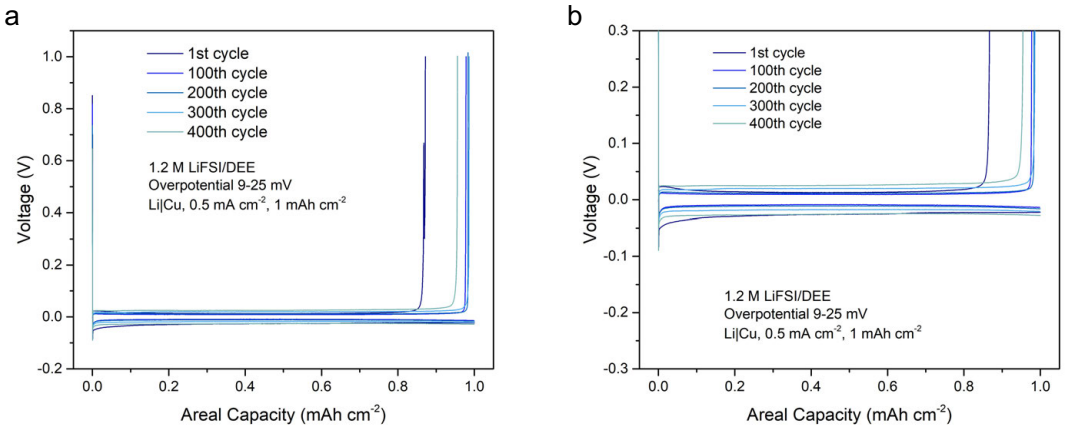

Supplementary Fig. 5. Voltage profiles of Li || Cu half cell using 1.2 M LiFSI/DEE at different cycle numbers.

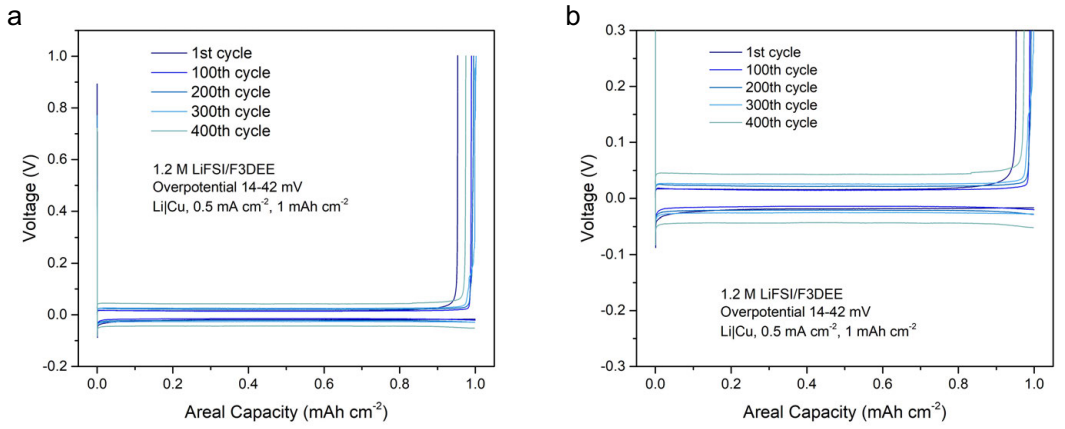

Supplementary Fig. 6. Voltage profiles of Li || Cu half cell using 1.2 M LiFSI/F3DEE at different cycle numbers.

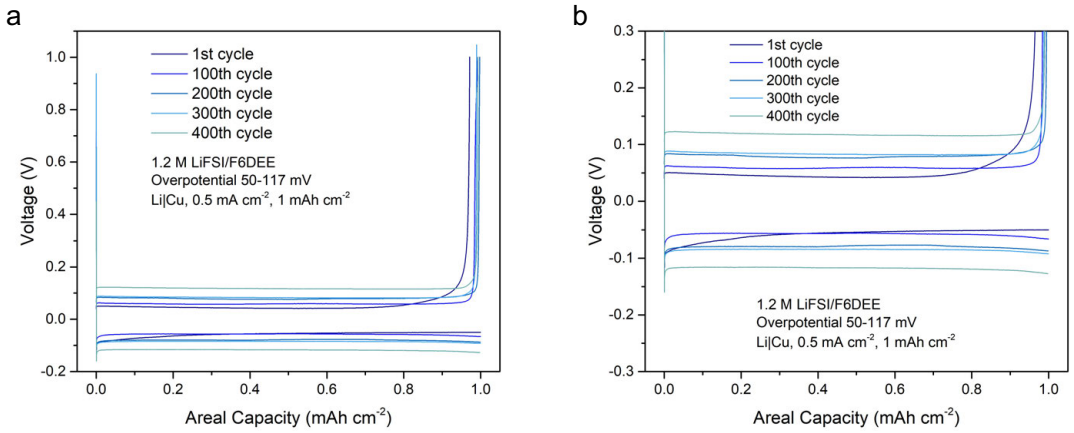

Supplementary Fig. 7. Voltage profiles of Li || Cu half cell using 1.2 M LiFSI/F6DEE at different cycle numbers.

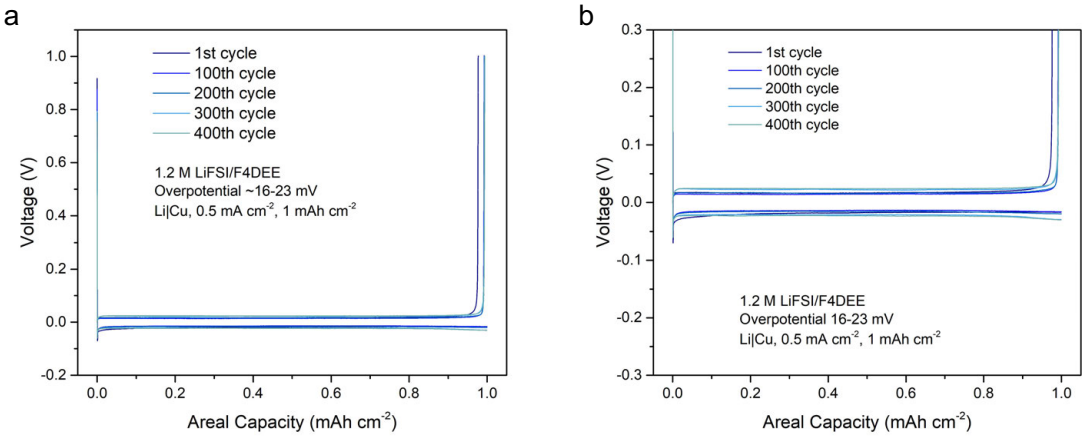

Supplementary Fig. 8. Voltage profiles of Li || Cu half cell using 1.2 M LiFSI/F4DEE at different cycle numbers.

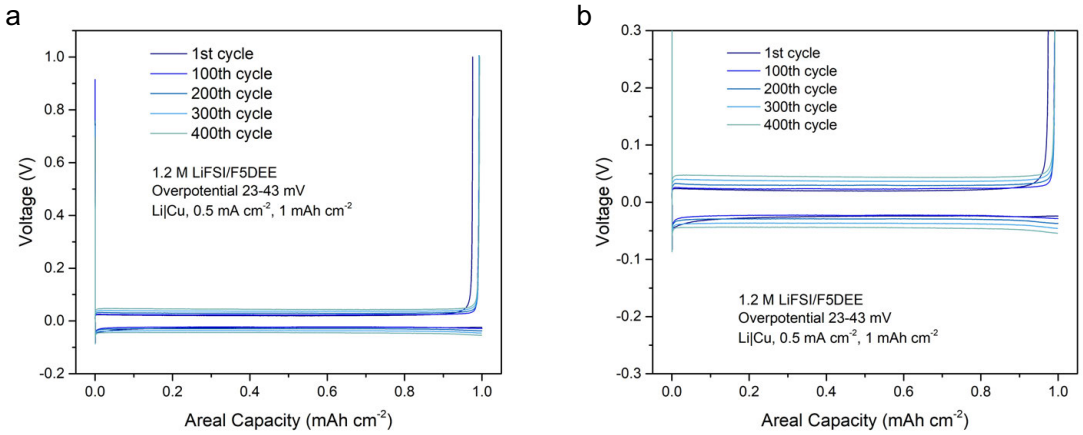

Supplementary Fig. 9. Voltage profiles of Li || Cu half cell using 1.2 M LiFSI/F5DEE at different cycle numbers.

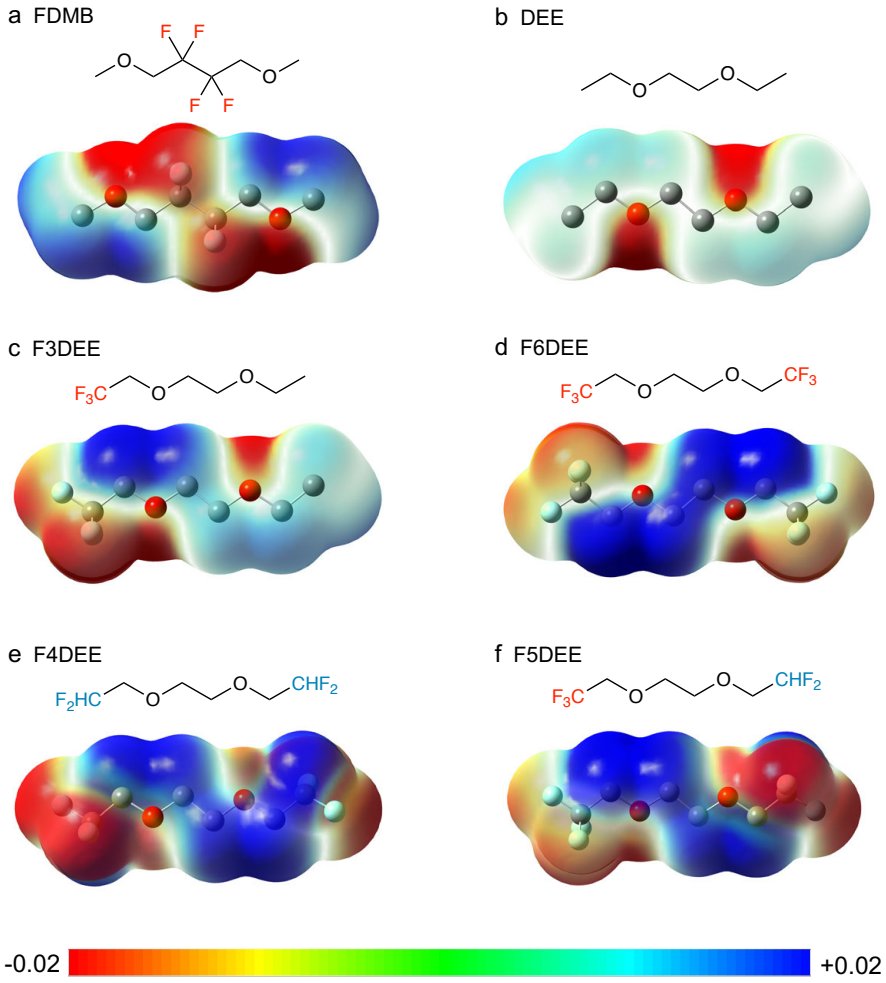

Supplementary Fig. 10. Electrostatic potential (ESP) of different solvent molecules.

Note: Generally, the negative charge was more located on O and F atoms of these molecules. However, fine difference can be observed when comparing the ESP of $–CF_3$ and $–CHF_2$. At the same isopotential scale, the $–CHF_2$ group showed more concentrated negative charge (darker red color) while the symmetric $–CF_3$ group showed slightly less negative charge (more yellowish color), especially when one compares the $–CF_3$ and $–CHF_2$ in F5DEE, or compares F4DEE and F6DEE. This observation is consistent with the stronger coordination capability of $–CHF_2$ than $–CF_3$, as elaborated in the manuscript.

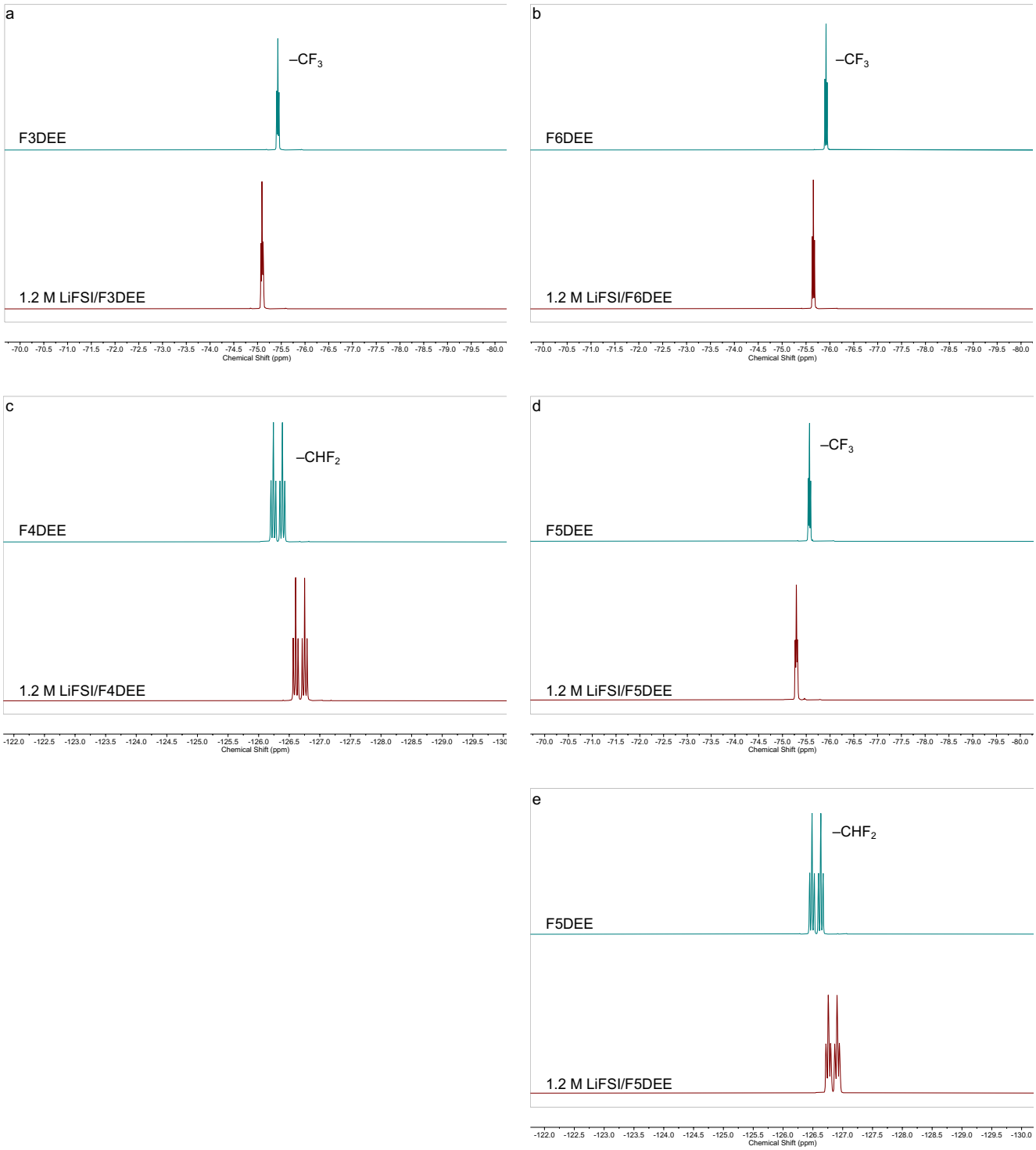

Supplementary Fig. 11. ^{19}F-NMR (376 MHz) spectra of pure fluorinated-DEEs and 1.2 M LiFSI in fluorinated-DEES. (a) –CF_3 on F3DEE and 1.2 M LiFSI/F3DEE. (b) –CF_3 on F6DEE and 1.2 M LiFSI/F6DEE. (c) –CHF_2 on F4DEE and 1.2 M LiFSI/F4DEE. (d) –CF_3 on F5DEE and 1.2 M LiFSI/F5DEE. (e) –CHF_2 on F5DEE and 1.2 M LiFSI/F5DEE.

Note: All –CF_3 groups on fluorinated-DEEs showed downfield shift while the –CHF_2 ones showed upfield shift. The upfield shift was recognized as an indication of strong Li–F interaction[1,22–24] since Li^+ ions and their attached (surrounding) FSI^- anions are close to these F atoms on –CHF_2 groups, leading to anion shielding effect.

a

FSI^-	FDMB	Probability (%)
0	3	0.342
0	4	1.411
1	2	2.926
1	3	4.715
1	4	0.425
2	1	8.665
2	2	25.807
2	3	5.949
3	0	1.552
3	1	22.575
3	2	13.294
3	3	0.607
4	0	3.391
4	1	6.131
4	2	0.82
5	0	0.721
5	1	0.495

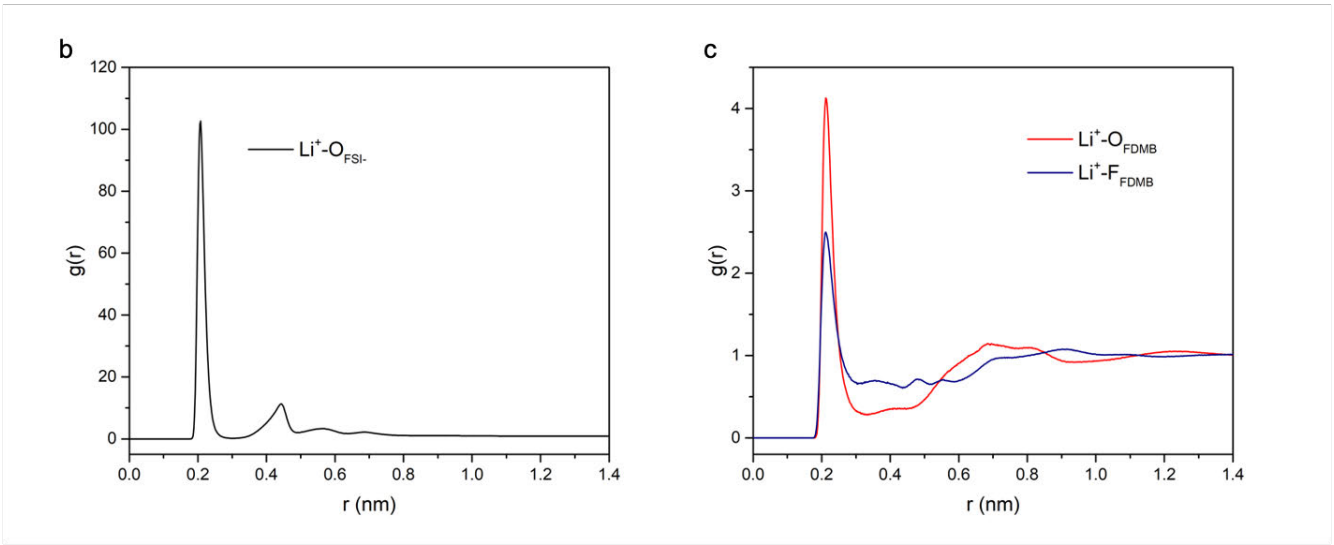

Supplementary Fig. 12. MD simulation results of 1 M LiFSI/FDMB. (a) Probabilities of different Li^+ solvates (with different anion and solvent numbers in the first solvation sheath). Blue: solvent surrounded Li^+ (SSL, i.e. $Li^+(FSI)_0$); green: Li^+–anion single pair (LASP, i.e. $Li^+(FSI)_1$); yellow: Li^+–anion cluster (LAC, i.e. $Li^+(FSI)_{\geq 2}$). (b) RDF between Li^+ and O atoms on FSI^-. (c) RDF between Li^+ and O/F atoms on FDMB solvent.

Note: These results were from newly conducted MD simulations where "scaled charges" were used for solvent molecules to maximize the electrostatic effect contributed by the solvents. Therefore the results here are different from those in ref.[1].

a

FSI^-	DEE	Probability (%)
0	2	11.732
0	3	0.241
1	2	37.613
2	1	47.883
2	2	0.804
3	1	1.699

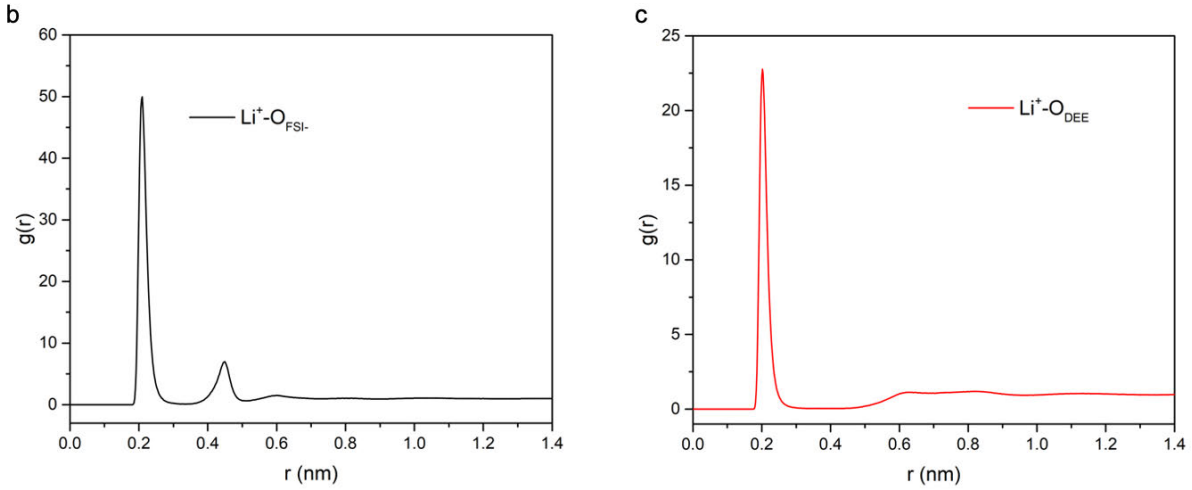

Supplementary Fig. 13. MD simulation results of 1.2 M LiFSI/DEE. (a) Probabilities of different Li^+ solvates (with different anion and solvent numbers in the first solvation sheath). Blue: SSL; green: LASP; yellow: LAC. (b) RDF between Li^+ and O atoms on FSI^-. (c) RDF between Li^+ and O atoms on DEE solvent.

a

FSI^-	F3DEE	Probability (%)
0	2	4.389
0	3	0.494
1	2	29.585
1	3	1.85
2	1	31.539
2	2	12.083
2	3	0.73
3	0	2.852
3	1	12.676
3	2	1.542
4	0	1.627
4	1	0.403

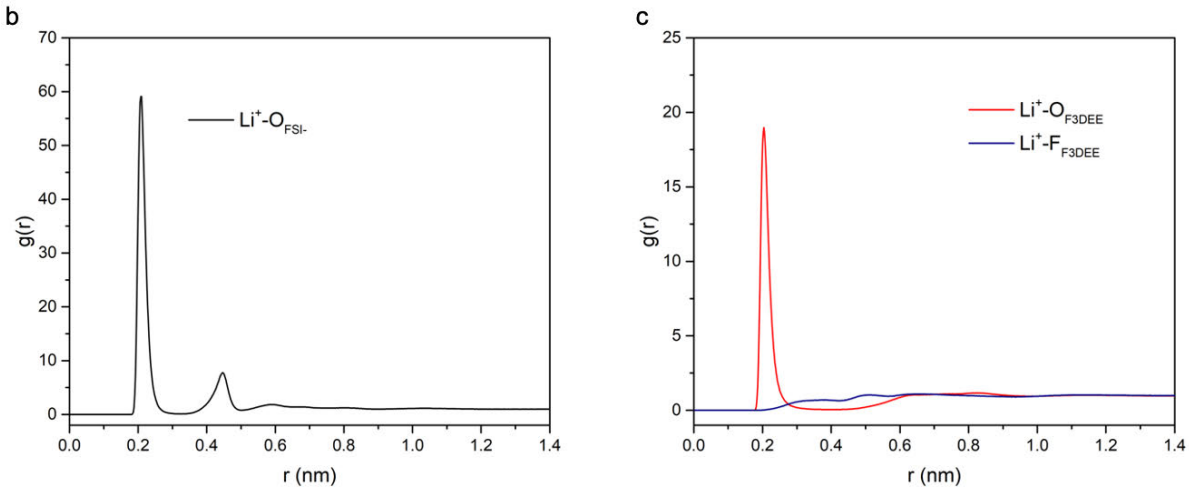

Supplementary Fig. 14. MD simulation results of 1.2 M LiFSI/F3DEE. (a) Probabilities of different Li^+ solvates (with different anion and solvent numbers in the first solvation sheath). Blue: SSL; green: LASP; yellow: LAC. (b) RDF between Li^+ and O atoms on FSI^-. (c) RDF between Li^+ and O/F atoms on F3DEE solvent.

a

FSI^-	F6DEE	Probability (%)
0	2	0.349
1	2	8.296
1	3	0.645
2	1	50.758
2	2	15.066
2	3	0.905
3	1	19.173
3	2	2.383
4	0	1.319
4	1	0.737

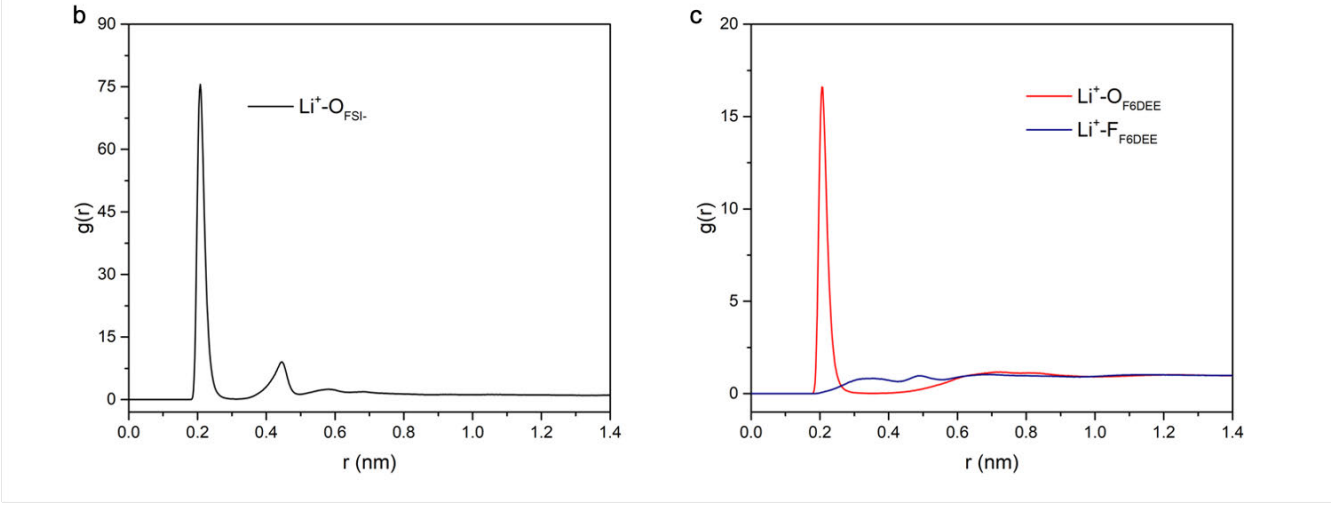

Supplementary Fig. 15. MD simulation results of 1.2 M LiFSI/F6DEE. (a) Probabilities of different Li^+ solvates (with different anion and solvent numbers in the first solvation sheath). Blue: SSL; green: LASP; yellow: LAC. (b) RDF between Li^+ and O atoms on FSI^-. (c) RDF between Li^+ and O/F atoms on F6DEE solvent.

a

FSI^-	F4DEE	Probability (%)
0	2	8.945
0	3	0.58
1	1	0.227
1	2	7.534
1	3	2.36
1	4	0.165
2	1	45.692
2	2	11.872
2	3	1.068
3	0	1.203
3	1	10.763
3	2	2.306
3	3	0.118
4	0	3.677
4	1	2.954
4	2	0.319

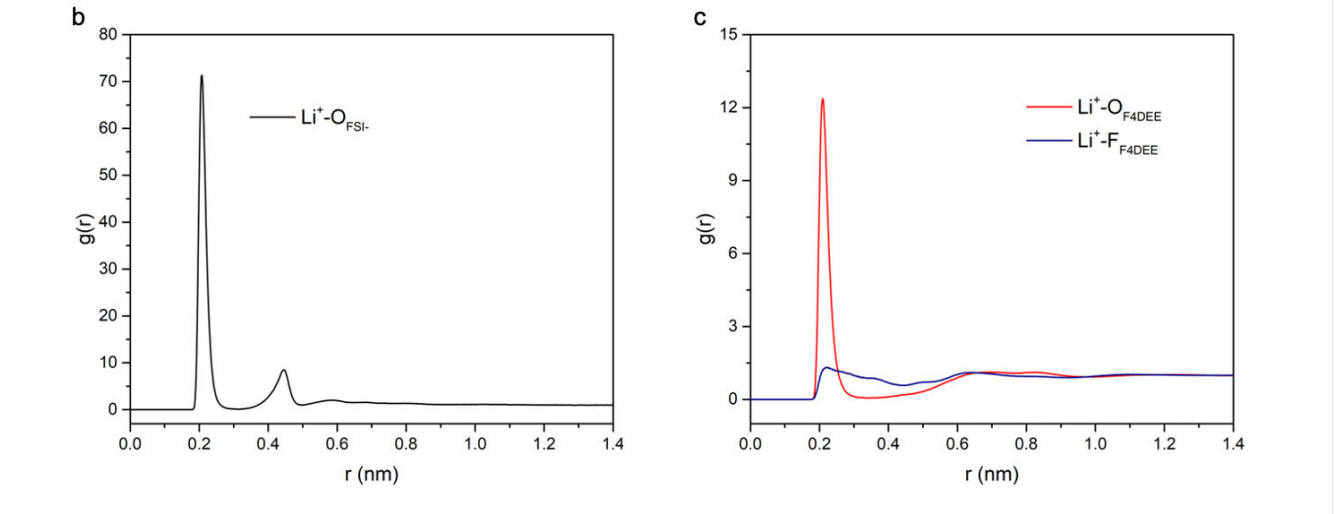

Supplementary Fig. 16. MD simulation results of 1.2 M LiFSI/F4DEE. (a) Probabilities of different Li^+ solvates (with different anion and solvent numbers in the first solvation sheath). Blue: SSL; green: LASP; yellow: LAC. (b) RDF between Li^+ and O atoms on FSI^-. (c) RDF between Li^+ and O/F atoms on F4DEE solvent.

Note: Compared with the Li-F_{F6DEE} RDF (Supplementary Fig. 15c), the Li-F_{F4DEE} showed higher peak around 0.2 nm, indicating stronger Li-F interaction between Li^+ and $–CHF_2$ than $–CF_3$. This is consistent with our design logic.

a

FSI^-	F5DEE	Probability (%)
0	2	7.21
0	3	0.286
1	1	0.127
1	2	9.5
1	3	2.119
1	4	0.159
2	1	42.398
2	2	11.433
2	3	0.847
3	0	1.539
3	1	16.987
3	2	1.805
4	0	3.297
4	1	1.897
4	2	0.215

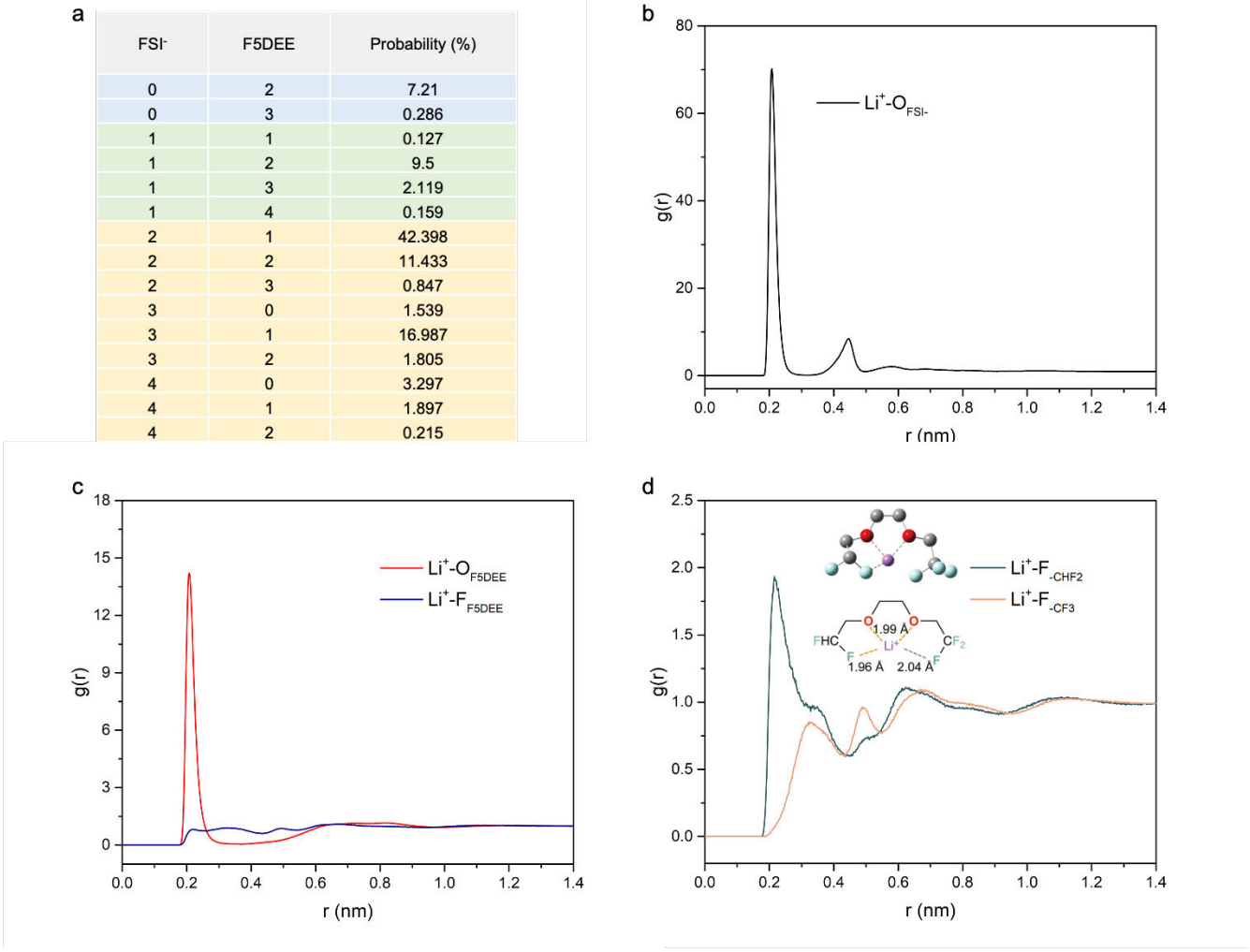

Supplementary Fig. 17. MD simulation results of 1.2 M LiFSI/F5DEE. (a) Probabilities of different Li^+ solvates (with different anion and solvent numbers in the first solvation sheath). Blue: SSL; green: LASP; yellow: LAC. (b) RDF between Li^+ and O atoms on FSI^-. (c) RDF between Li^+ and O/F atoms on F5DEE solvent. (d) Separated RDF between Li^+ and F atoms on $–CHF_2$ than $–CF_3$.

Note: As shown in Supplementary Fig. 17d, the Li-$F_{–CHF2}$ RDF peak is much higher than Li-$F_{–CF3}$ one at around 0.2 nm, indicating more F atoms on $–CHF_2$ participating into the Li^+ solvation than the ones on $–CF_3$. Such stronger interaction between Li^+ and $–CHF_2$ matches well with the DFT results (lower distance between Li^+ and $–CHF_2$ than $–CF_3$). This confirms the benefit of $–CHF_2$ incorporation, and is consistent with our design.

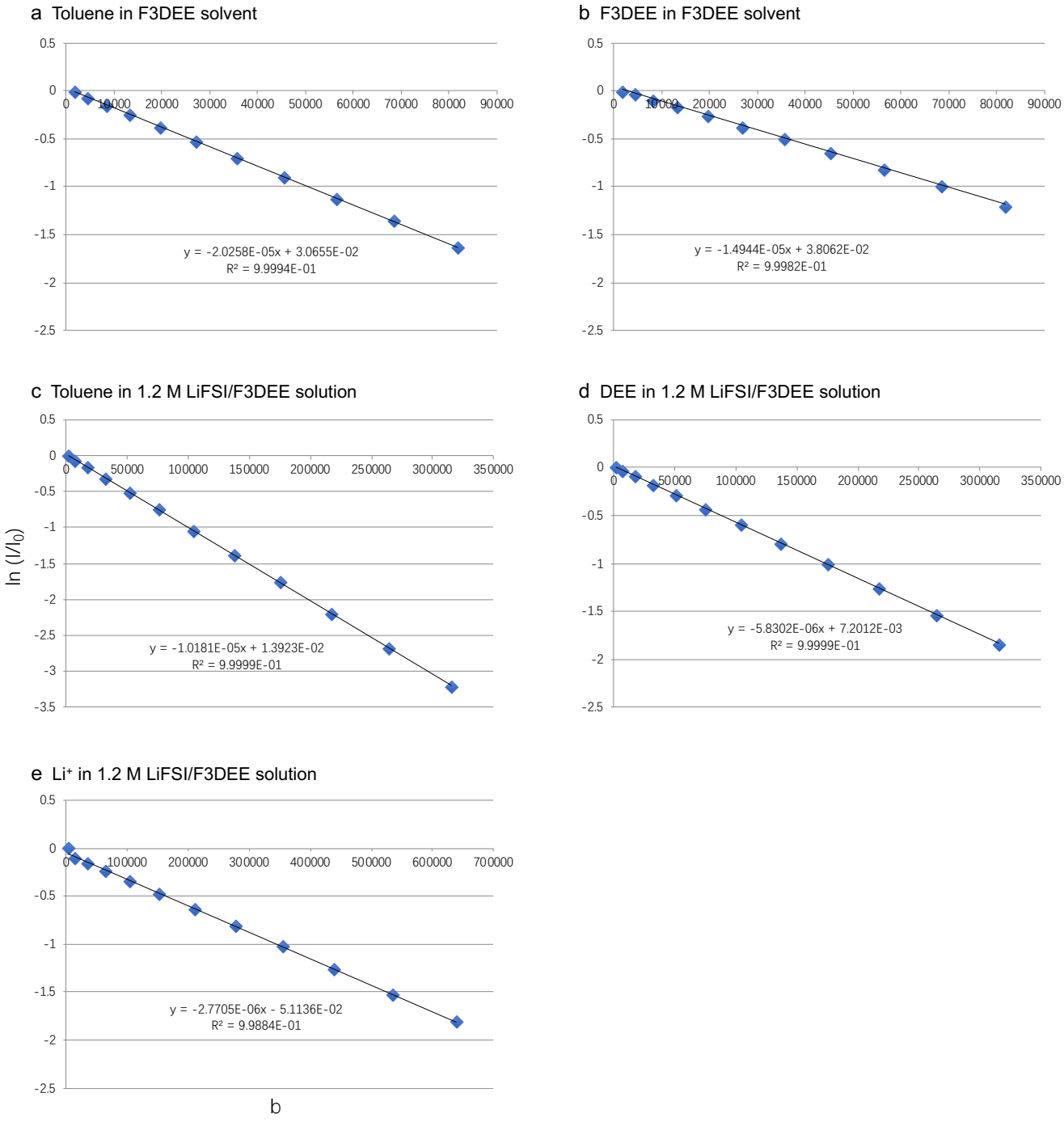

Supplementary Fig. 18. Fitting results of internal reference DOSY NMR (taking the pair of F3DEE and 1.2 M LiFSI/F3DEE as an example here). All the results were summarized in Supplementary Table 2. The method was previously developed by Amine et al.[2,3] to determine the Li^+ coordination number in electrolyte solution.

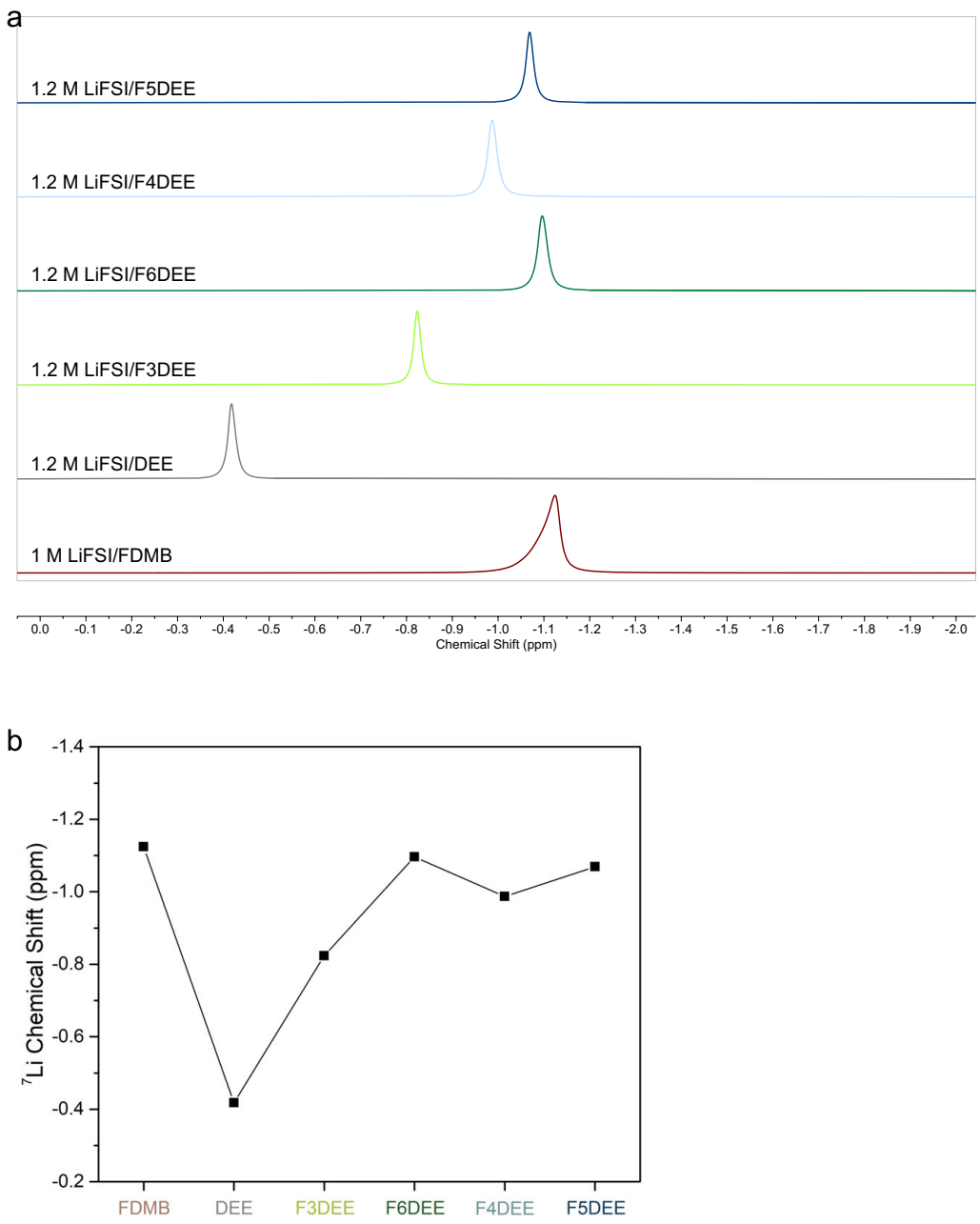

Supplementary Fig. 19. ^{7}Li NMR (194 MHz) results of 1 M LiFSI/FDMB (extracted from ref.[1]) and 1.2 M LiFSI in fluorinated-DEEs. The chemical shift positions were plotted in (b), following the design flow (the x-axis order is different from that in main Fig. 3).

Note: The more negative the ^{7}Li shift is (upfield shift), the more shielded the Li^{+} ion is. Usually this indicates more anions surrounding Li^{+} ions since negatively charged anions provide more shielding effect for Li^{+}. In ^{7}Li-NMR spectra, more upfield shift was observed for 1 M LiFSI/FDMB and 1.2 M LiFSI/F6DEE, indicating weakly-solvated anion-shielded Li^{+} (i.e. close Li^{+}-FSI^{-} clustering); on the contrary, downfield chemical shifts in DEE, F3DEE and F4DEE electrolytes confirmed their strong solvation ability (i.e. separating Li^{+}-FSI^{-} ion pairs)[25].

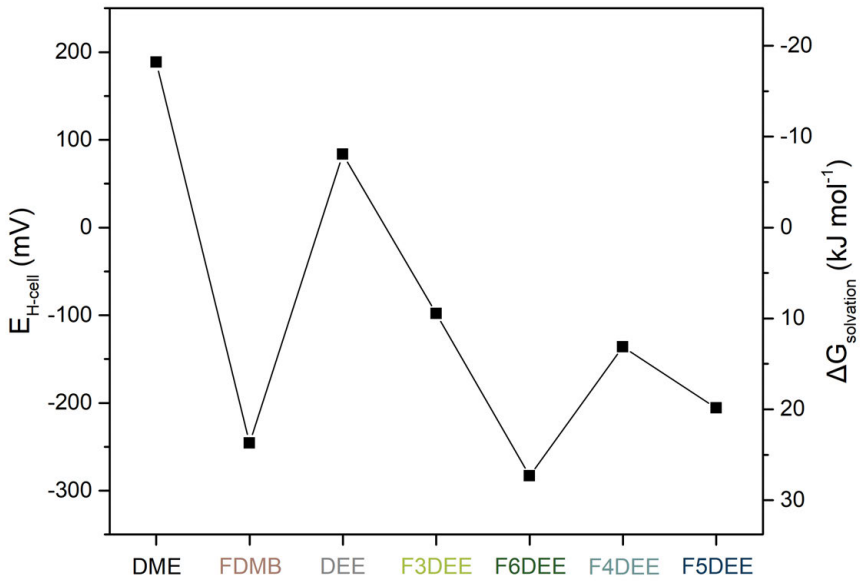

Supplementary Fig. 20. Solvation energy ($\Delta G_{solvation}$) measurements of fluorinated-DEE electrolytes following the design flow (the x-axis order is different from that in main Fig. 3).

Note: The solvation Gibbs free energy ($\Delta G_{solvation}$) was converted from the measured H-cell open circuit voltage ($E_{H\text{-}cell}$) using equation: $\Delta G = -nFE$. The detailed method and rationales were described in Kim and Cui et al. unpublished. Regardless of the measurement technique, the solvation Gibbs free energy is an overall evaluation of the binding strength (how much the Gibbs energy decreases) between Li^+ and surrounding species (both solvent and anion). Since the anion is fixed as FSI^- in the measured electrolytes, stronger binding solvents (e.g. DME and DEE herein) will participate more into the Li^+ solvation sheath and lead to more negative solvation energies, indicating more Li^+-anion dissociation (or less ion pairing). This argument is consistent with both theoretical and other experimental results as well as the discussions in the manuscript.

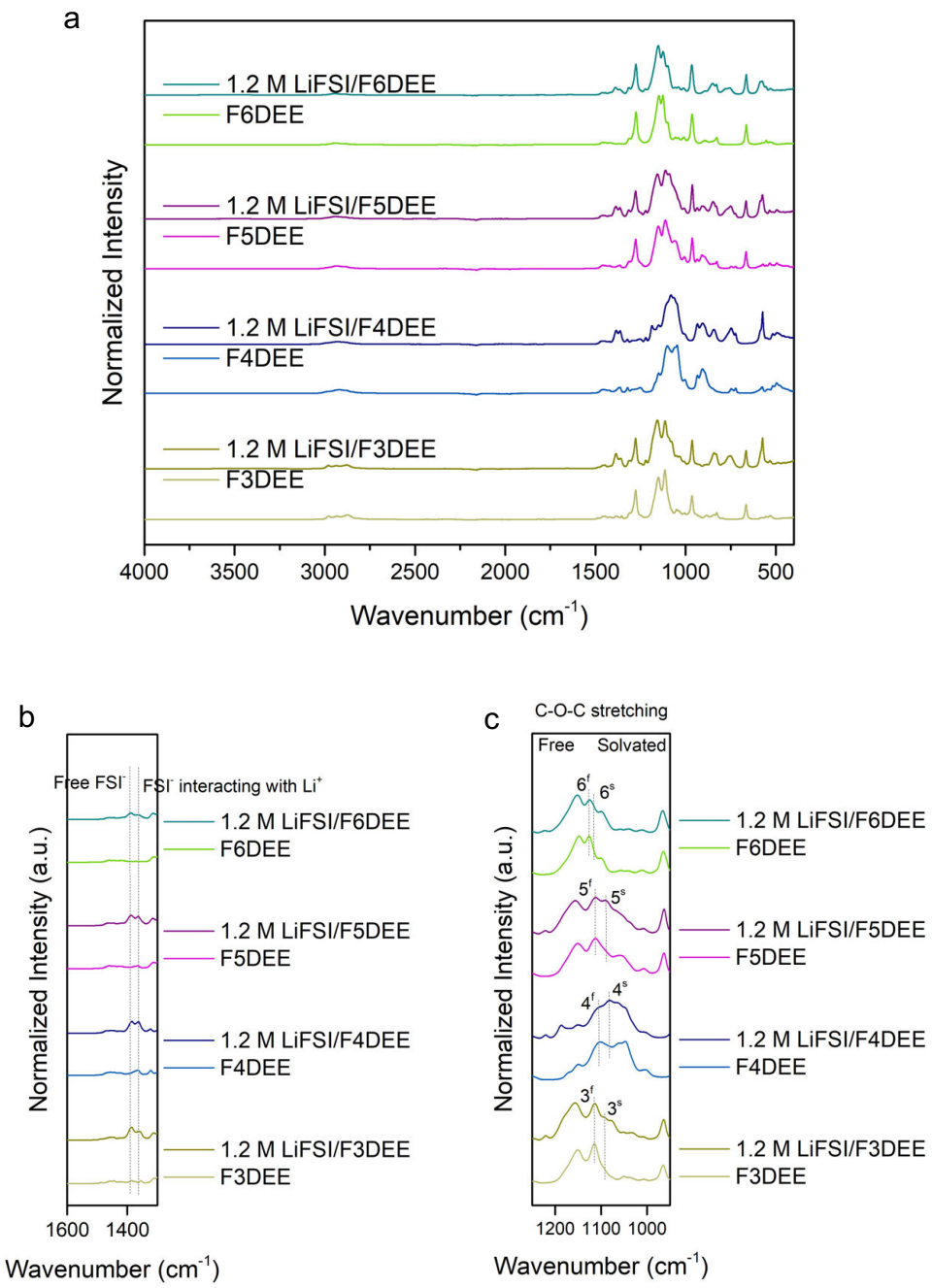

Supplementary Fig. 21. FTIR results of 1.2 M LiFSI in fluorinated-DEEs. (a) The whole spectra. (b) Zoomed-in region of FSI^- anion peaks. (c) Zoomed-in region of ether group peaks.

Note: The zoomed-in region of C-O-C stretching showed higher "solvated" ether peaks in F3DEE (3^s), F4DEE (4^s), and F5DEE (5^s) electrolytes compared to F6DEE one (6^s), indicating more solvating solvents in the former three electrolytes. In F6DEE, even only "free" solvent (6^f) can be observed.

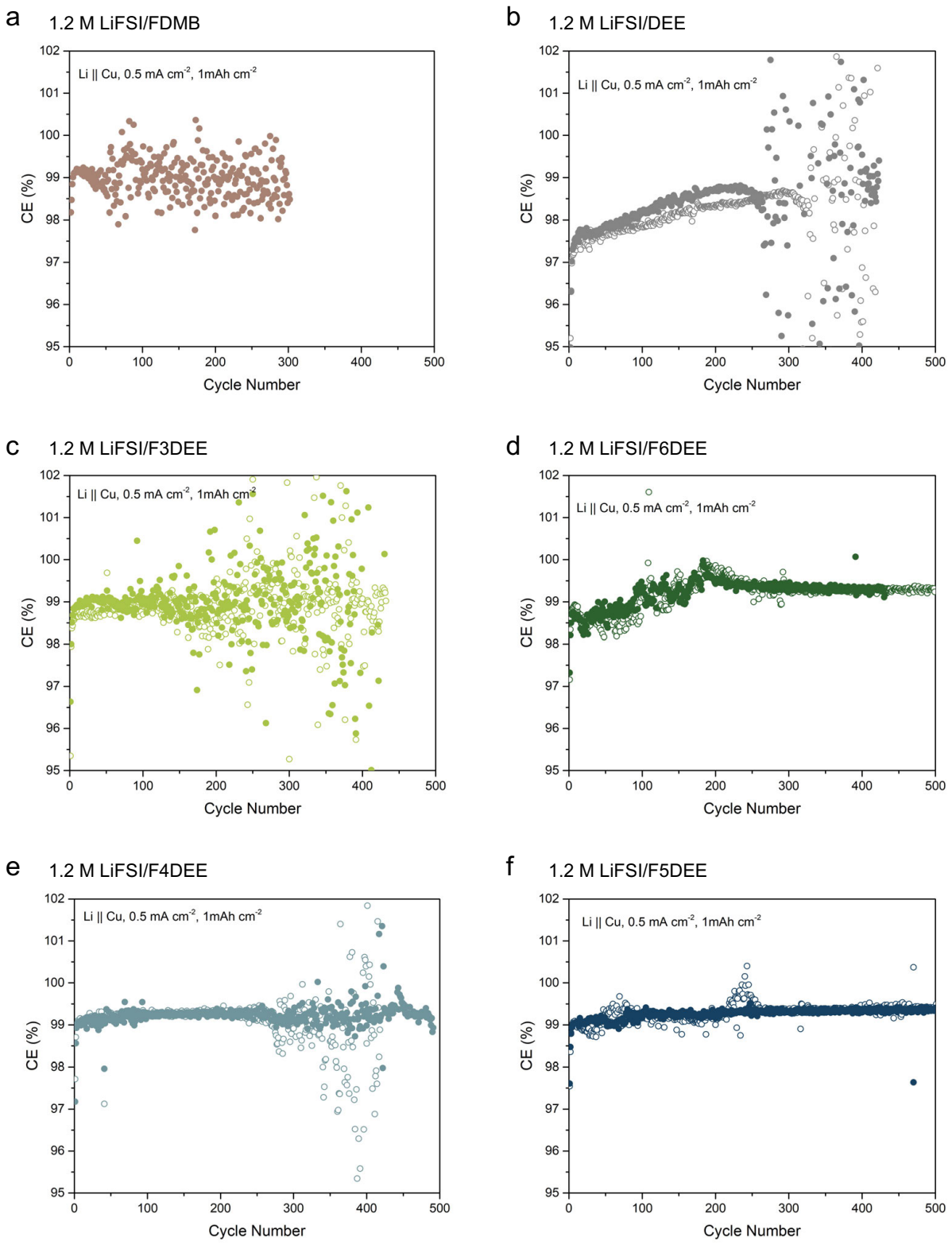

Supplementary Fig. 22. Long cycling of conventional (thin spring) Li || Cu half cells at 0.5 mA cm^{-2} and 1 mAh cm^{-2}, using fluorinated-DEE electrolytes: 1 M LiFSI/FDMB (a, extracted from ref.[1]), 1.2 M LiFSI/DEE (b), 1.2 M LiFSI/F3DEE (c), 1.2 M LiFSI/F6DEE (d), 1.2 M LiFSI/F4DEE (e), and 1.2 M LiFSI/F5DEE (f). Two parallel cells were shown in each electrolyte.

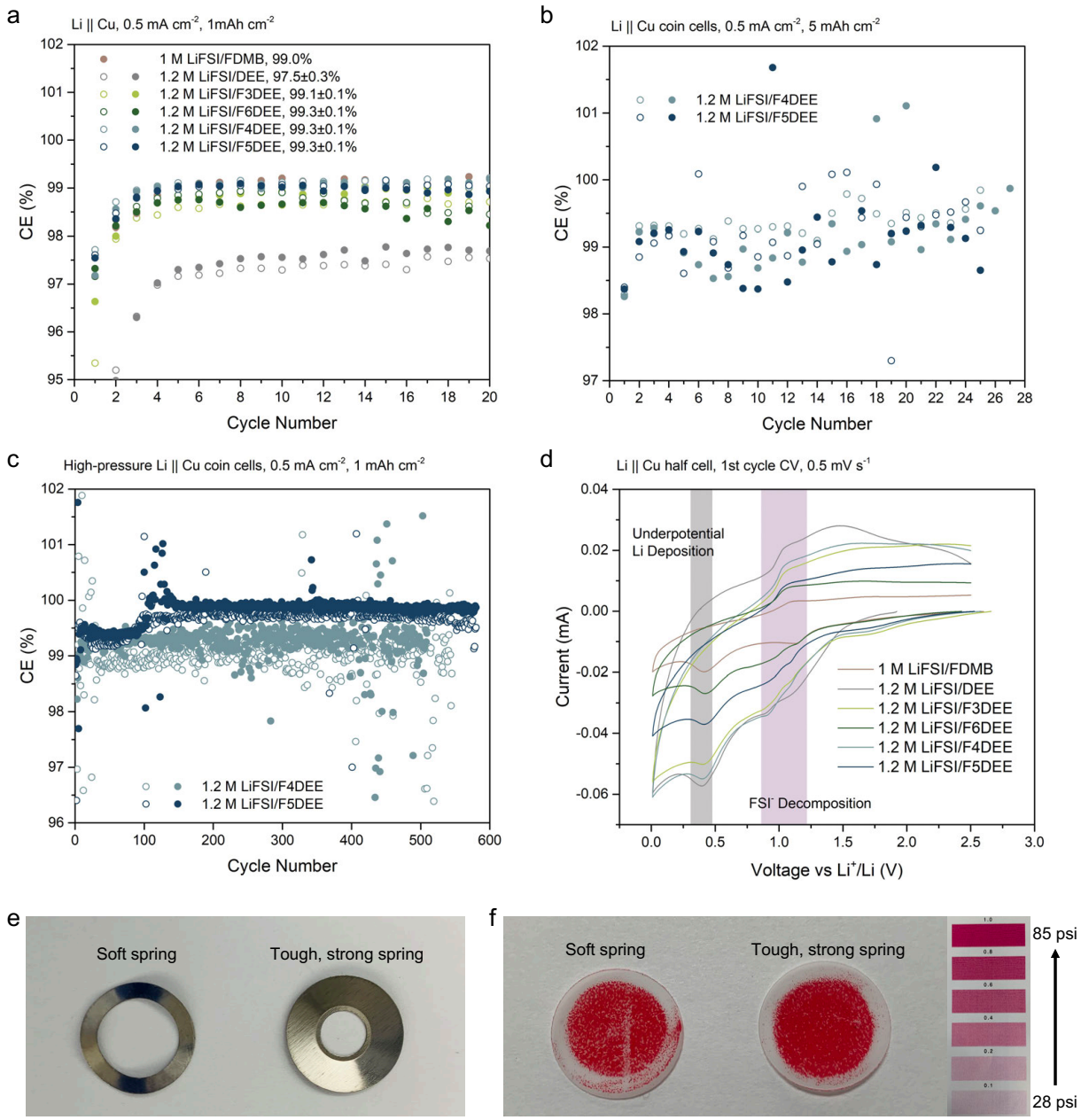

Supplementary Fig. 23. (a,b) Initial cycling of Li || Cu half cells at 0.5 mA cm^{-2} and 1 mAh cm^{-2} (a) and 0.5 mA cm^{-2} and 5 mAh cm^{-2} (b). (c) Long cycling of high-pressure (tough spring shown in (e)) Li || Cu half cells at 0.5 mA cm^{-2} and 1 mAh cm^{-2}. (d) CV curves of Li || Cu cells using different electrolytes in this work. (e) Images of soft and strong springs. Parallel cell results were given in each case. (f) Pressure inside coin cells with different springs measured by pressure-indicating films (Fujifilm Prescale® LLLW, 28-85 psi).

Note: Under different conditions, the F4DEE and F5DEE electrolytes enabled high CE in Li || Cu half cells. Particularly, the CE of Li || Cu half cells using F5DEE under high pressure reached 99.8-99.9% during long cycling. Figure (d) showed FSI^- anion decomposition peaks for all electrolytes when scanning CV for Li || Cu half cells, indicating anion-derived SEI; however, 1.2 M LiFSI/DEE showed earlier and easier FSI^- decomposition (gray curve, >1.3 V) compared to fluorinated-DEE electrolytes, which may be responsible for worse Li metal stability in DEE. Figure (f) showed that the strong spring provided higher and more uniform internal pressure for coin cells than the soft one.

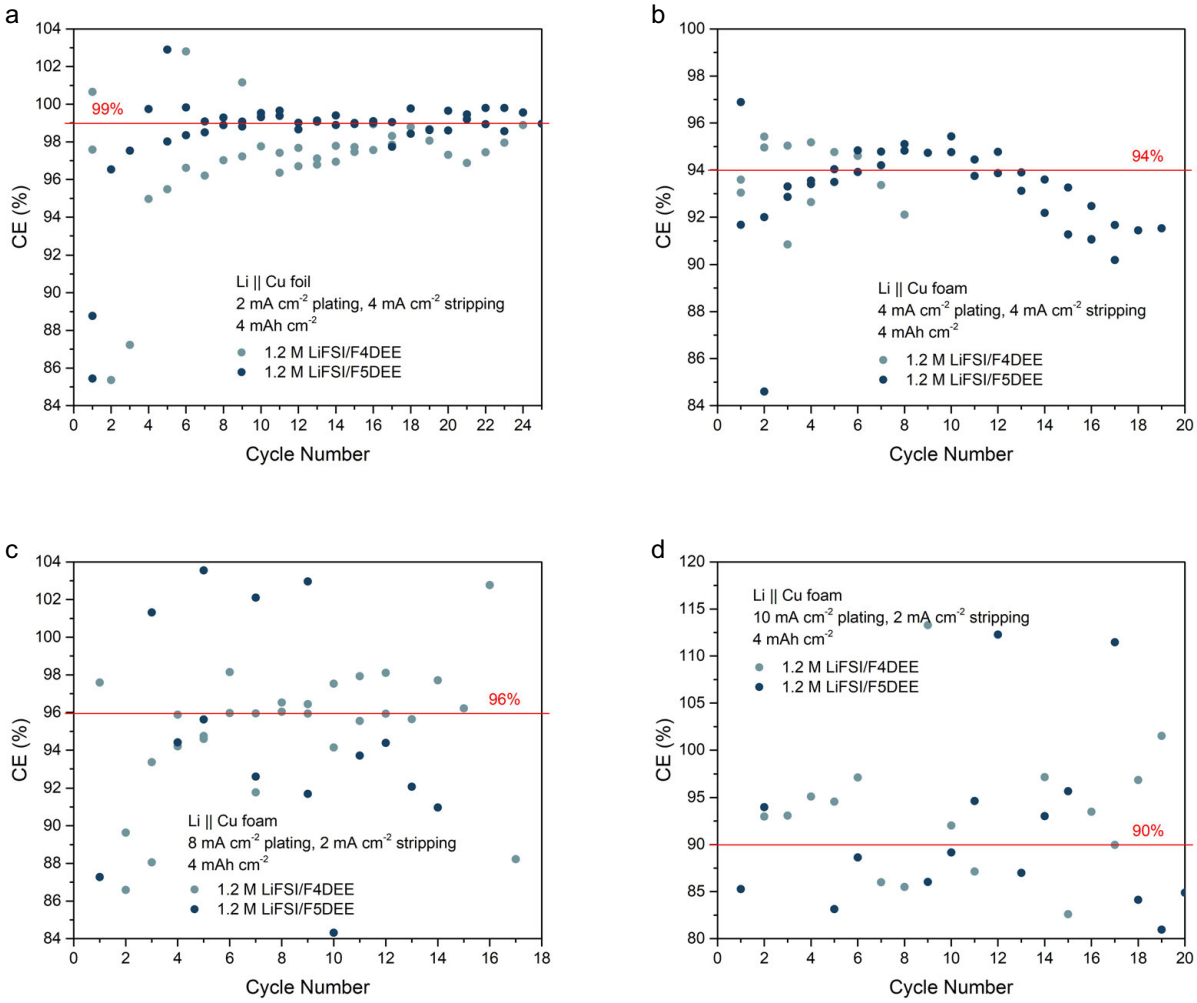

Supplementary Fig. 24. Cycling CE of Li || Cu half cells at high currents and high capacities. (a) Cu foil, 2 mA cm^{-2} plating, 4 mA cm^{-2} stripping and 4 mAh cm^{-2} capacity. (b) Cu foam, 4 mA cm^{-2} plating, 4 mA cm^{-2} stripping and 4 mAh cm^{-2} capacity. (c) Cu foam, 8 mA cm^{-2} plating, 2 mA cm^{-2} stripping and 4 mAh cm^{-2} capacity. (d) Cu foam, 10 mA cm^{-2} plating, 2 mA cm^{-2} stripping and 4 mAh cm^{-2} capacity.

Note: In Li || Cu half cells, higher currents (>4 mA cm^{-2}) can lead to a reasonable decrease in Li metal CE compared to lower currents (Supplementary Fig. 23). However, at 2 mA cm^{-2} plating, 4 mA cm^{-2} stripping and 4 mAh cm^{-2} capacity which are harsher than the cycling condition in anode-free Cu || LFP cells (main text Fig. 5i-k), the cycling CE using 1.2 M LiFSI/F4DEE or 1.2 M LiFSI/F5DEE was still maintained as high as ~99%.

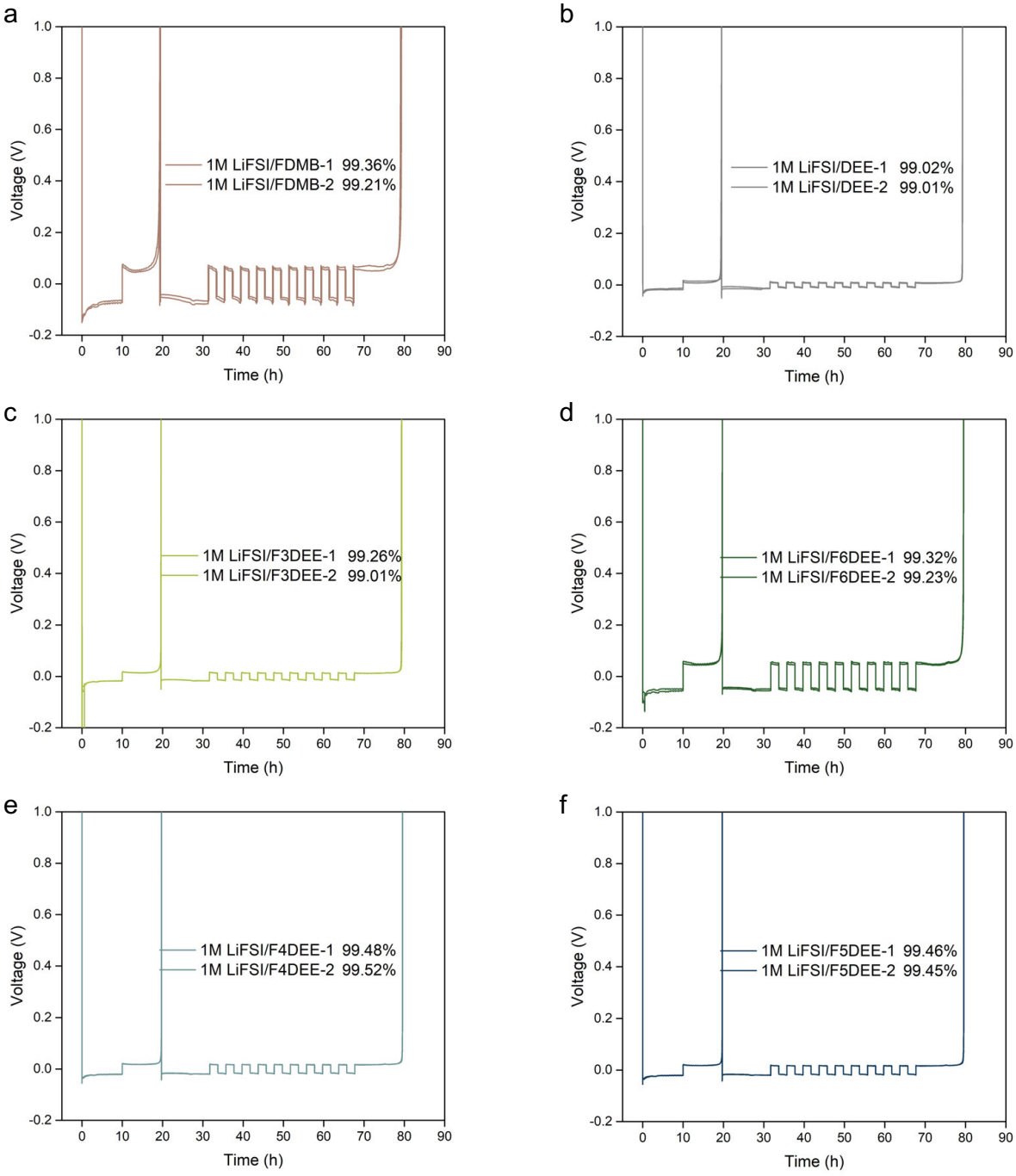

Supplementary Fig. 25. Aurbach method[26,27] using repeated Li || Cu half cells to obtain average CEs for the fluorinated-DEE based electrolytes: 1 M LiFSI/FDMB (a), 1.2 M LiFSI/DEE (b), 1.2 M LiFSI/F3DEE (c), 1.2 M LiFSI/F6DEE (d), 1.2 M LiFSI/F4DEE (e), and 1.2 M LiFSI/F5DEE (f).

Note: For each electrolyte, two parallel cells were tested to show repeatability of Aurbach method. Both cells for each electrolyte showed similar average Li metal CE and similar overpotential.

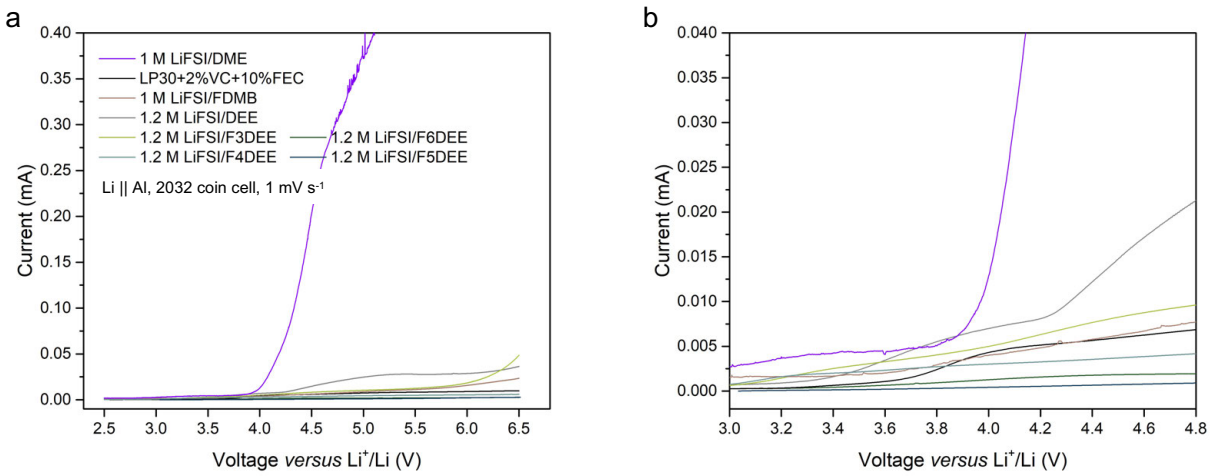

Supplementary Fig. 26. LSV of Li || Al coin cells using fluorinated-DEE electrolytes, in which the data of 1 M LiFSI/FDMB and 1 M LiFSI/DME were extracted from ref.[1].

Note: The leaking current is an indication of Al corrosion at high voltage, which is a critical factor for the stability of cathodes and functionality of high-voltage batteries.

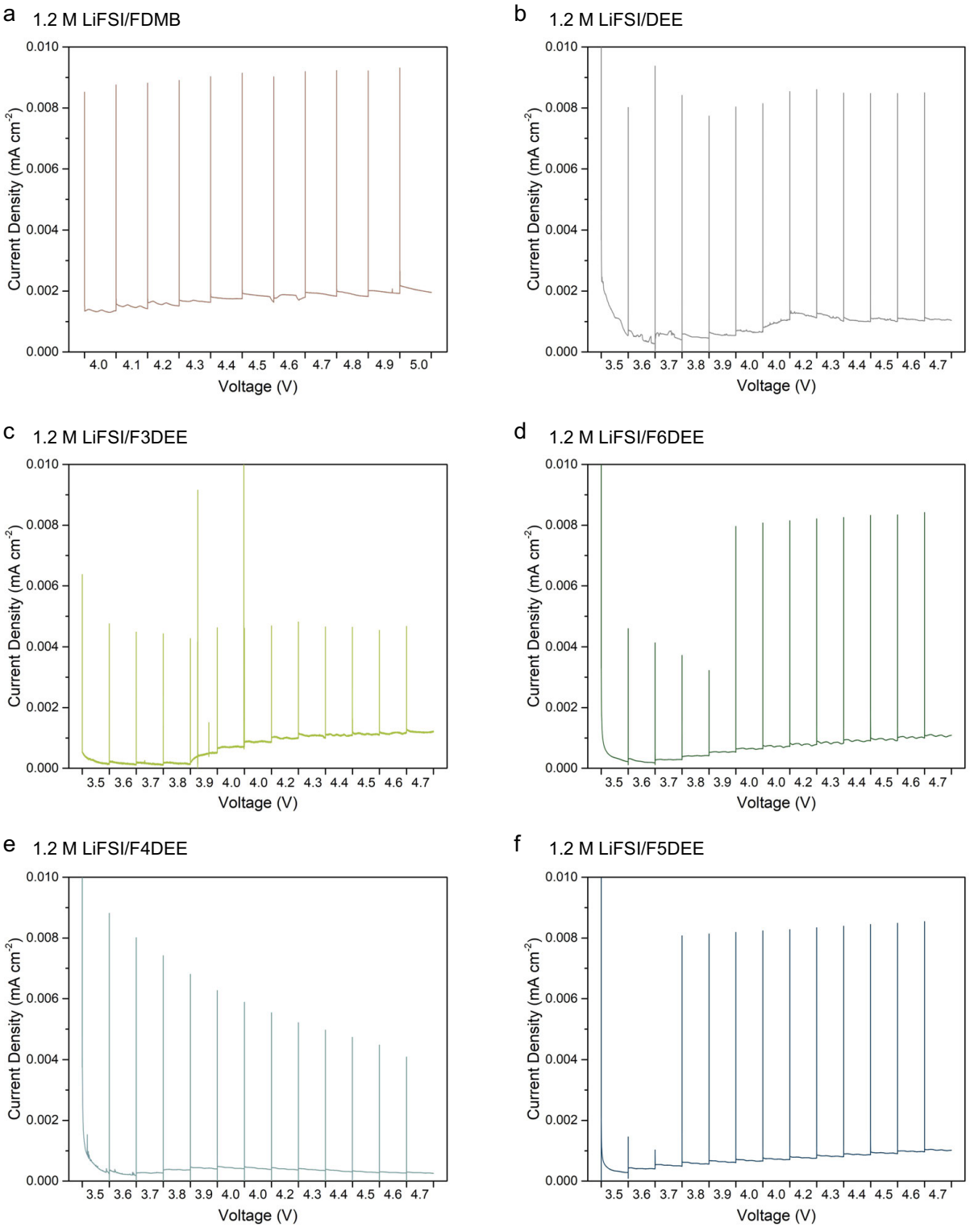

Supplementary Fig. 27. Potatiostatic polarization of Li || Al coin cells using fluorinated-DEE electrolytes: 1 M LiFSI/FDMB (a, extracted from ref.[1]), 1.2 M LiFSI/DEE (b), 1.2 M LiFSI/F3DEE (c), 1.2 M LiFSI/F6DEE (d), 1.2 M LiFSI/F4DEE (e), and 1.2 M LiFSI/F5DEE (f).

Note: All developed electrolytes, except 1.2 M LiFSI/DEE and 1.2 M LiFSI/F3DEE, showed decent oxidative stability in these potatiostatic polarization tests by exhibiting either decaying or plateaued current during each voltage holding step.

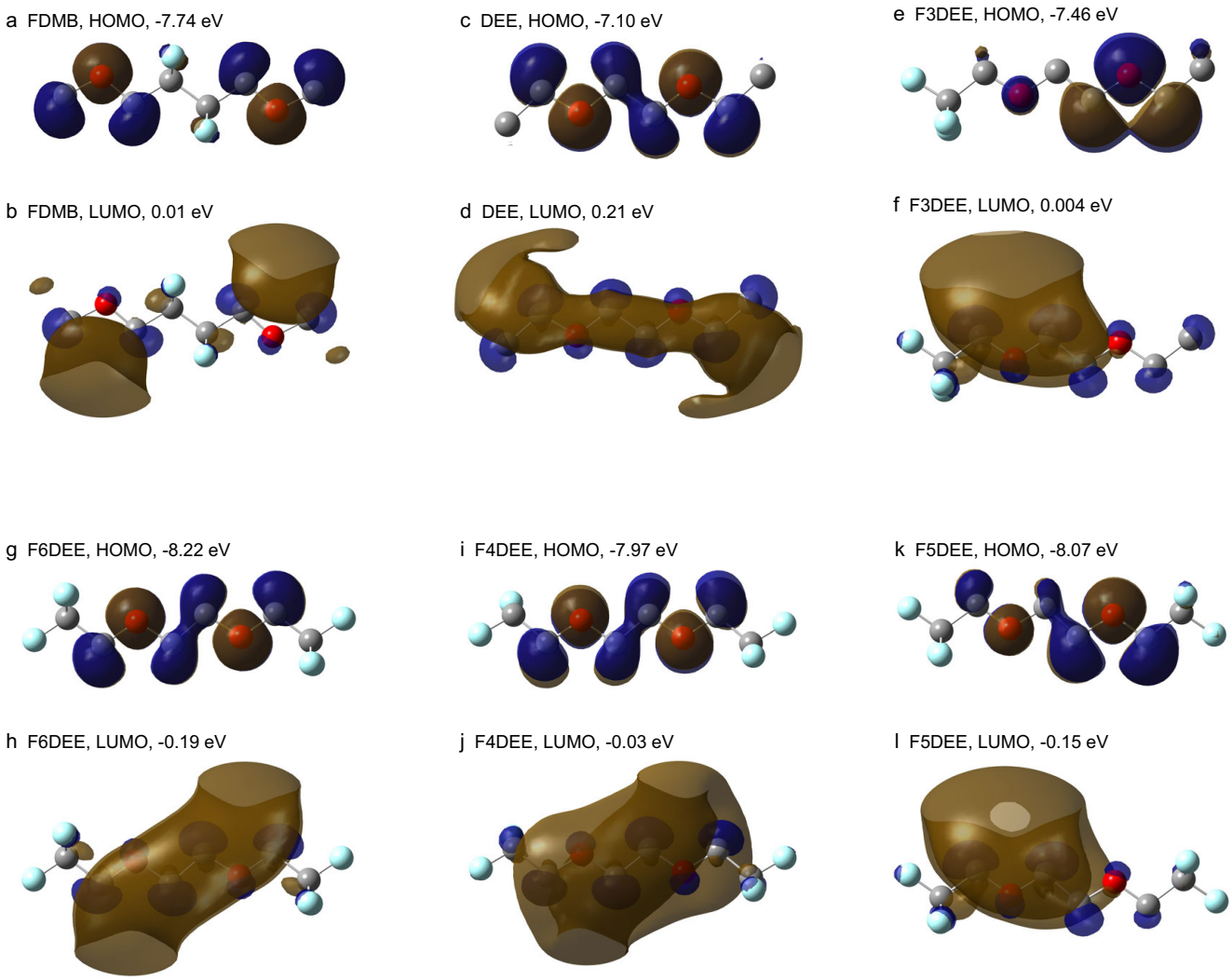

Supplementary Fig. 28. HOMO and LUMO levels of different fluorinated-DEE molecules.

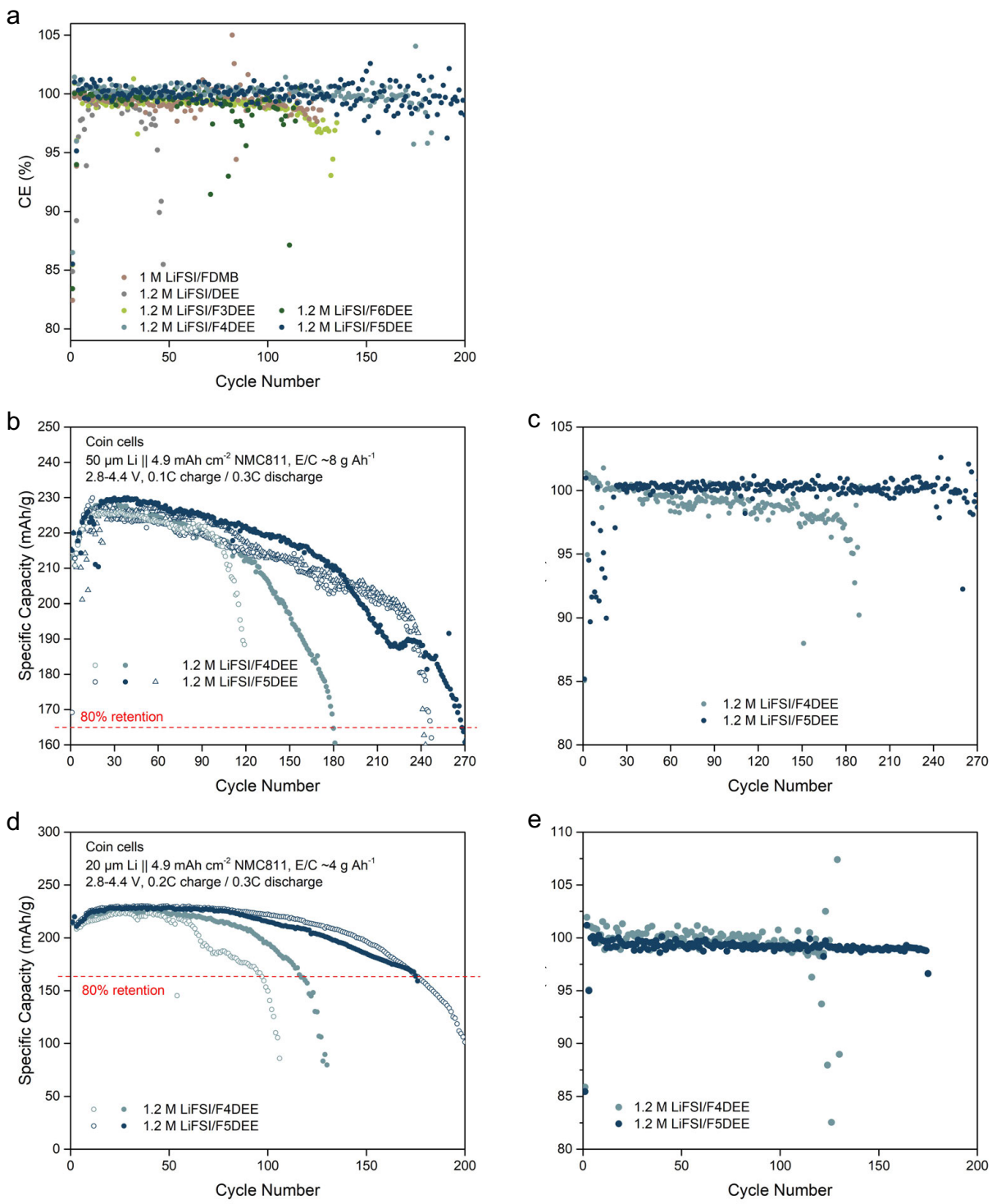

Supplementary Fig. 29. Cycling performance of thin Li || 4.9 mAh cm^{-2} NMC811 coin cells using fluorinated-DEE electrolytes. (a) CEs of 50 μm Li || 4.9 mAh cm^{-2} NMC811 cells at 0.2C charge 0.3C discharge, which were extracted from the testing results in main text Fig. 5c. (b,c) Capacity retention (b) and CEs (c) of 50 μm Li || 4.9 mAh cm^{-2} NMC811 cells at 0.1C charge 0.3C discharge. (d,e) Capacity retention (d) and CEs (e) of 20 μm Li || 4.9 mAh cm^{-2} NMC811 cells at 0.2C charge 0.3C discharge. Replicated cell data were shown here.

Note: The 50 μm Li || 4.9 mAh cm^{-2} NMC811 cells at 0.1C charge 0.3C discharge using 1.2 M LiFSI/F5DEE showed CE fluctuation at the early stage, which was caused by the instrument shutdown and temperature fluctuation.

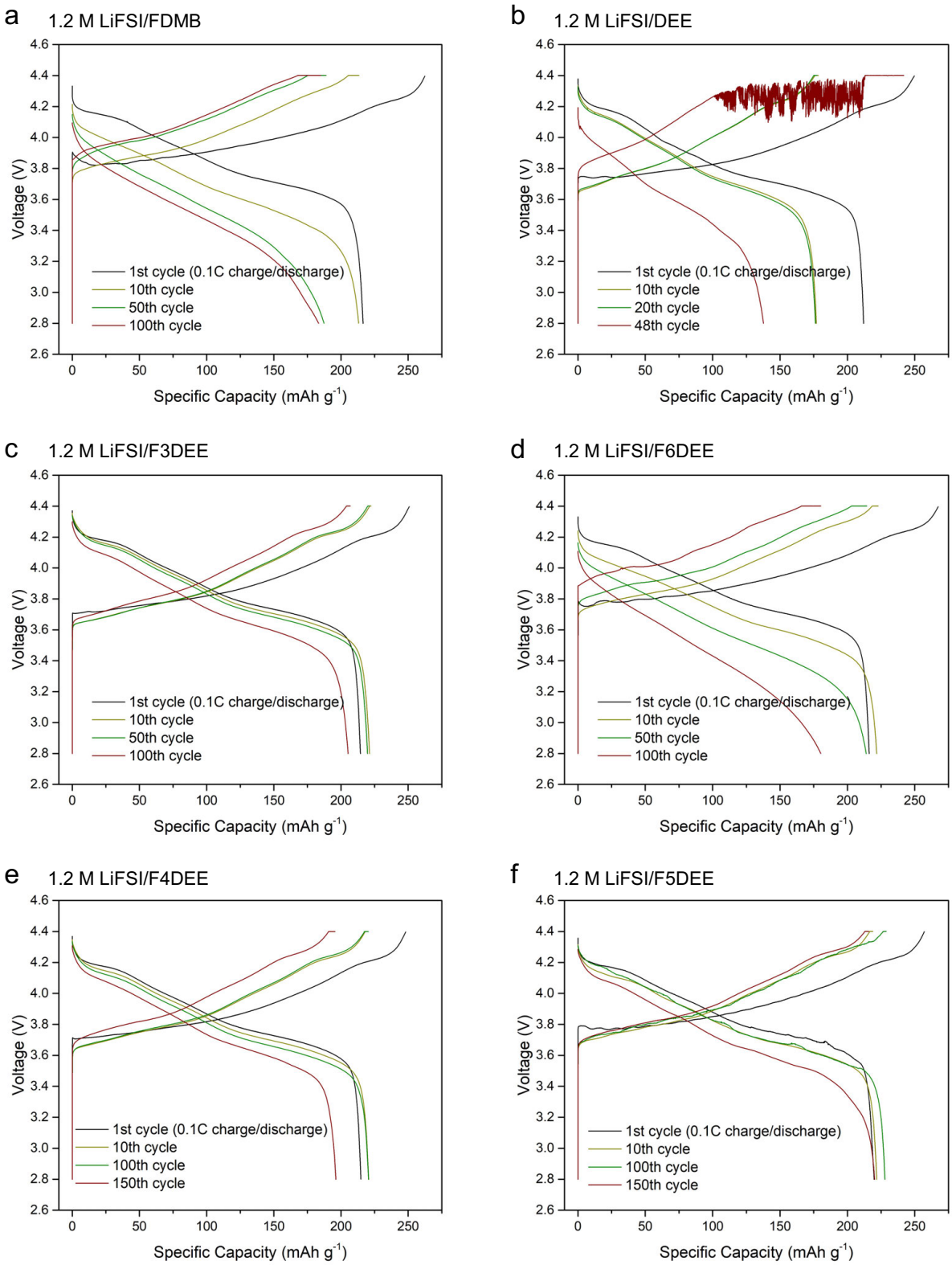

Supplementary Fig. 30. Charge/discharge curves of 50 μm Li || ~4.9 mAh cm^{-2} NMC811 coin cells using fluorinated-DEE electrolytes at 0.2C charge 0.3C discharge.

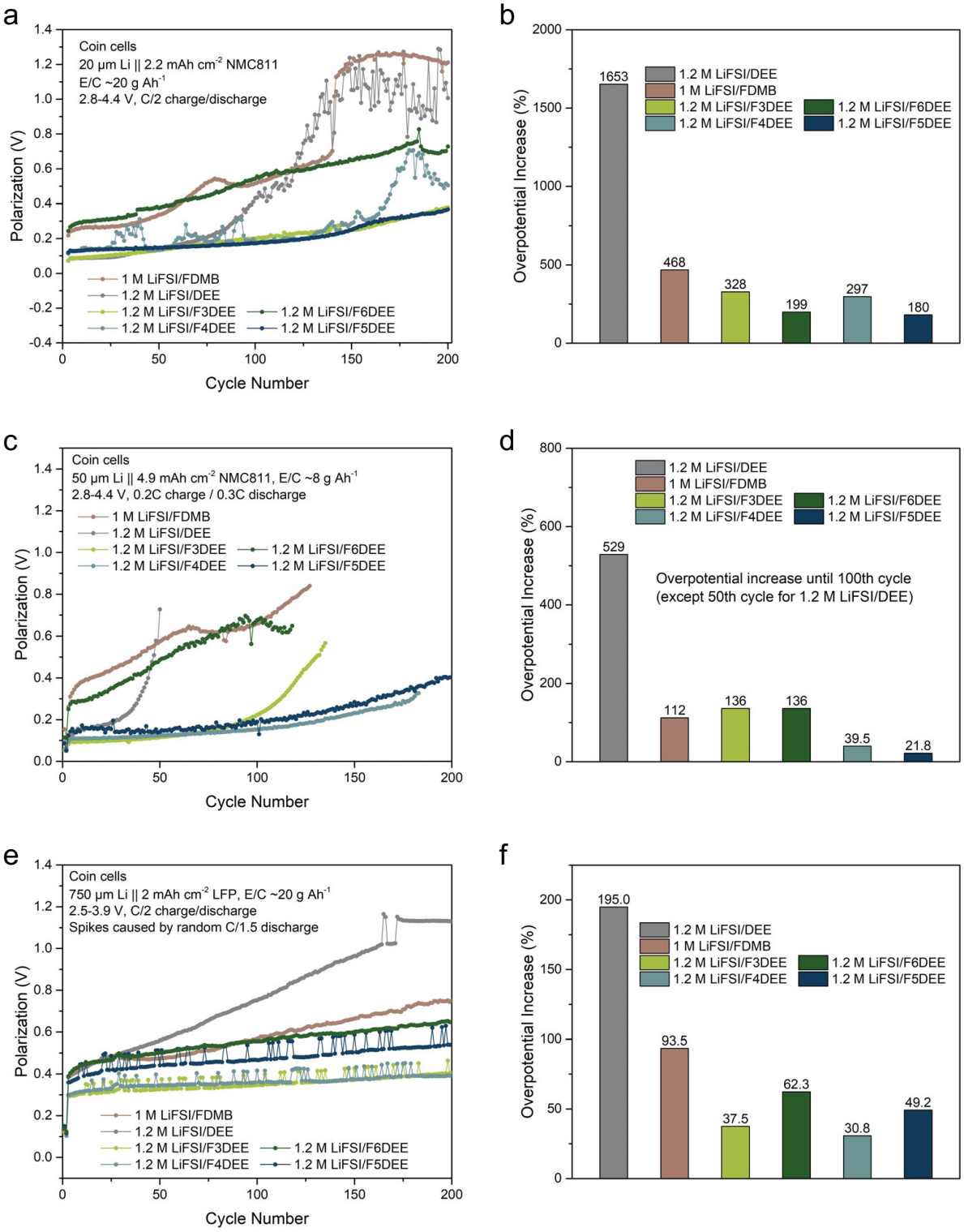

Supplementary Fig. 31. Voltage polarization of Li || NMC811 or microparticle-LFP coin cells. (a,b) 20 μm Li || ~2.2 mAh cm^{-2} NMC811. (c,d) 50 μm Li || ~4.9 mAh cm^{-2} NMC811. (e,f) 750 μm Li || ~2 mAh cm^{-2} microparticle-LFP. (b,d,f) showed the overpotential increase percentage.

a

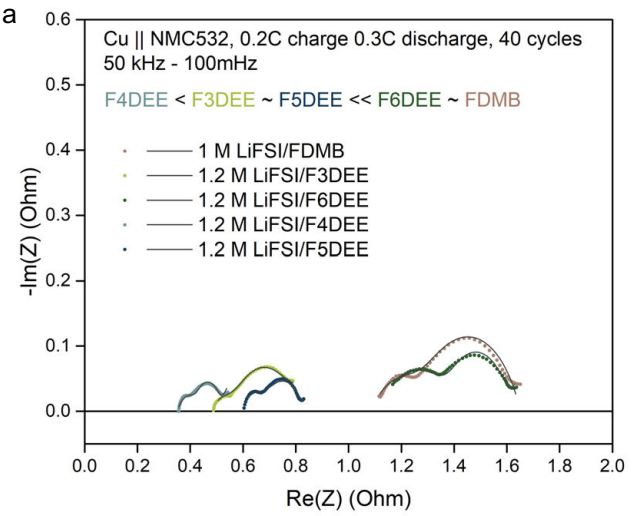

b

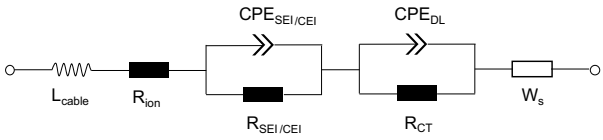

c

	R_{ion} (Ω)	$R_{interface}$ (Ω)*
1 M LiFSI/FDMB	1.05	0.614
1.2 M LiFSI/F3DEE	0.392	0.317
1.2 M LiFSI/F6DEE	1.11	0.490
1.2 M LiFSI/F4DEE	0.350	0.159
1.2 M LiFSI/F5DEE	0.508	0.239

Supplementary Fig. 32. EIS plots (a) and fitting results (b,c) of Cu || NMC532 pouch cells after 40 cycles at 0.2C charge 0.3C discharge. The fitting is based on simplified equivalent circuit[28]. The $R_{interface}$ was the sum of SEI, CEI, and charge transfer resistance, serving as the overall estimation of interfacial impedance.

Note: Similar to the overpotential trend in Li || NMC811 cells (Supplementary Fig. 30 and 31), the EIS of anode-free Cu || NMC532 cells showed impedance trend of FDMB ~ F6DEE >> F5DEE ~ F3DEE > F4DEE.

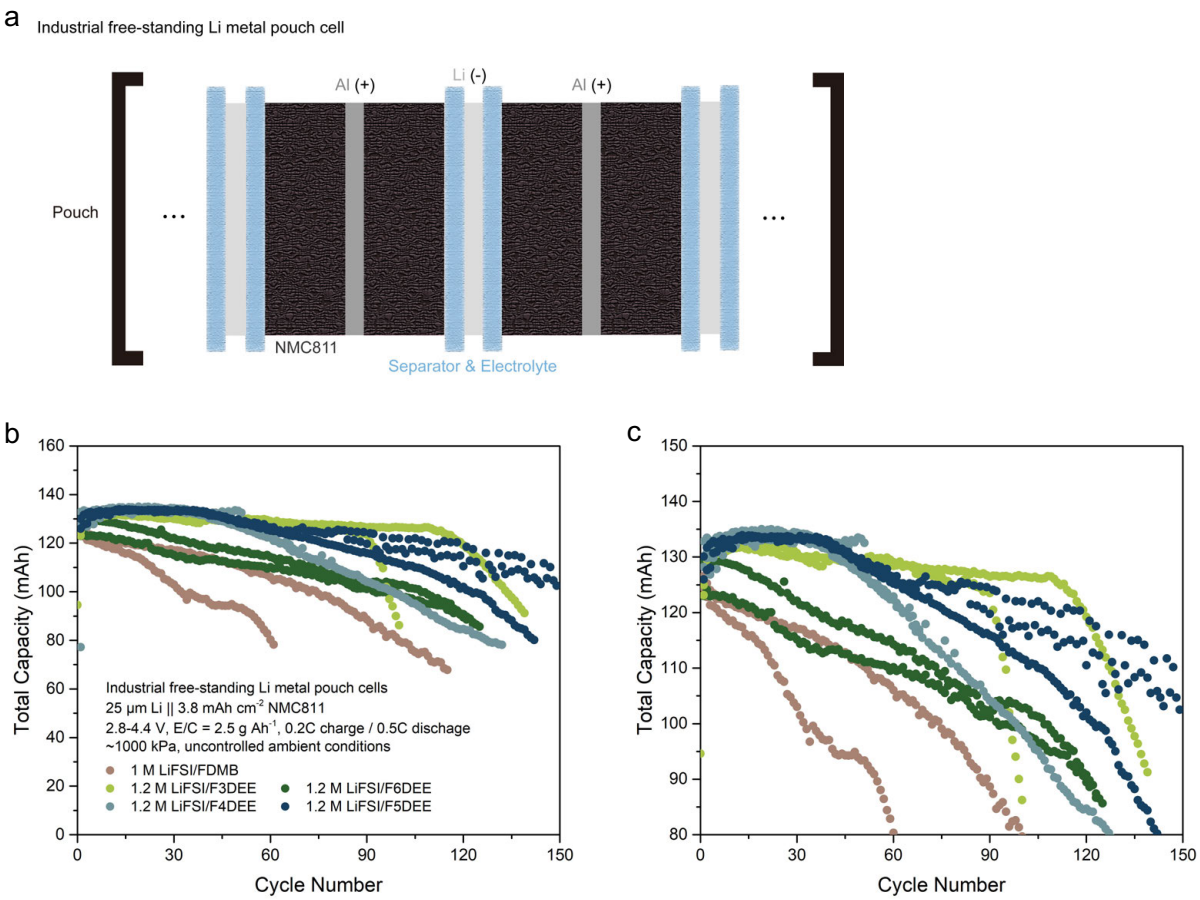

Supplementary Fig. 33. Battery structure (a) and cycling performance (b,c) of 25 µm Li || 3.8 mAh cm^{-2} NMC811 industrial free-standing pouch cells using fluorinated-DEE electrolytes. (c) is the zoomed-in scale of (b).

Note: The free-standing Li metal foil used in these industrial pouch cells was 50 µm thick but it faced two NMC811 electrodes with its both sides; therefore, we counted it as 25 µm Li || 3.8 mAh cm^{-2} NMC811.

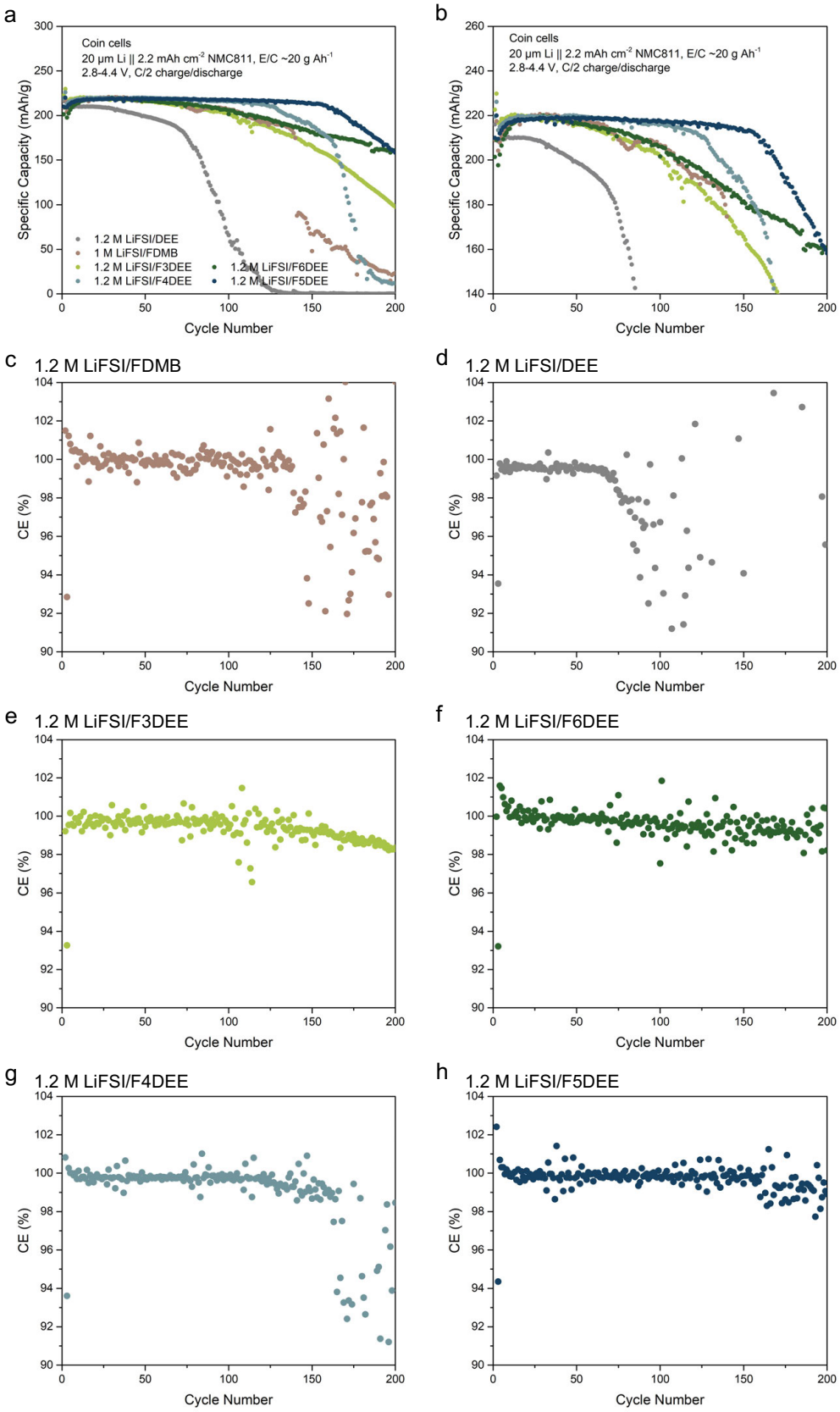

Supplementary Fig. 34. Cycling performance of 20 µm Li || ~2.2 mAh cm^{-2} NMC811 coin cells using fluorinated-DEE electrolytes at 0.5C charge 0.5C discharge: capacity retention (a,b) and CE (c-h) with cycle number. (b) is the zoomed-in scale of (a).

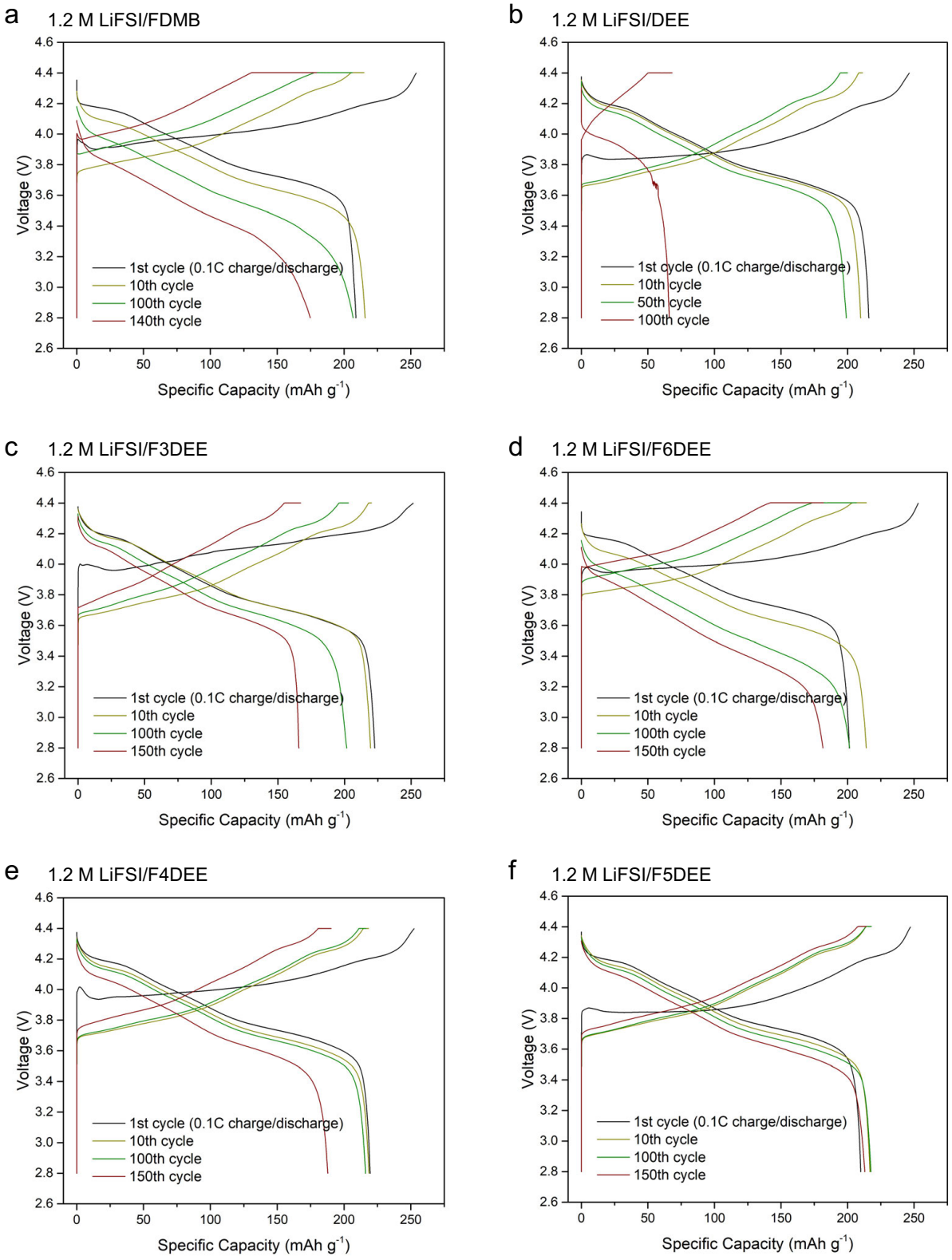

Supplementary Fig. 35. Charge/discharge curves of 20 μm Li || ~2.2 mAh cm^{-2} NMC811 coin cells using fluorinated-DEE electrolytes at 0.5C charge 0.5C discharge.

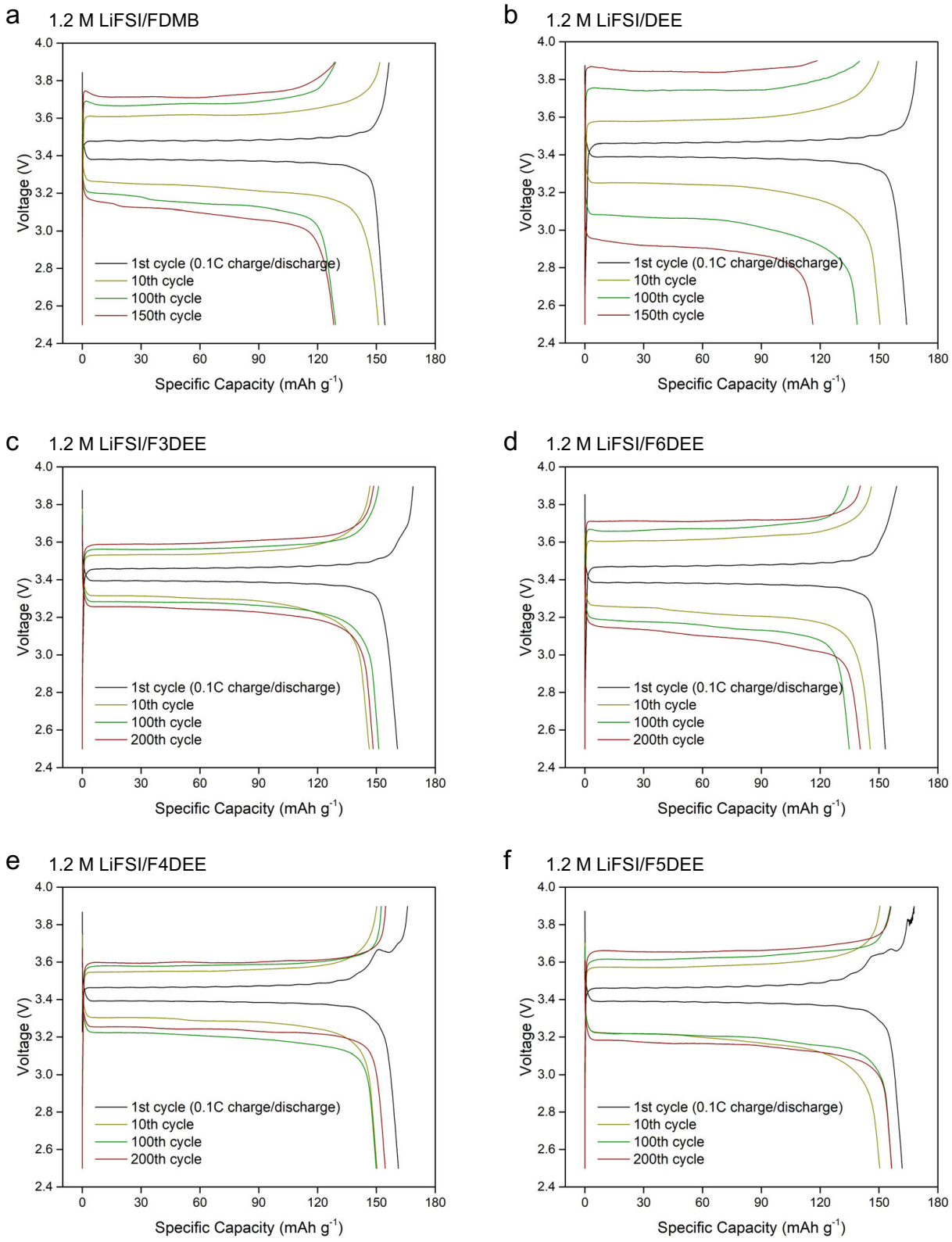

Supplementary Fig. 36. Charge/discharge curves of 750 μm Li || ~2 mAh cm^{-2} microparticle-LFP coin cells using fluorinated-DEE electrolytes at 0.5C charge 0.5C discharge.

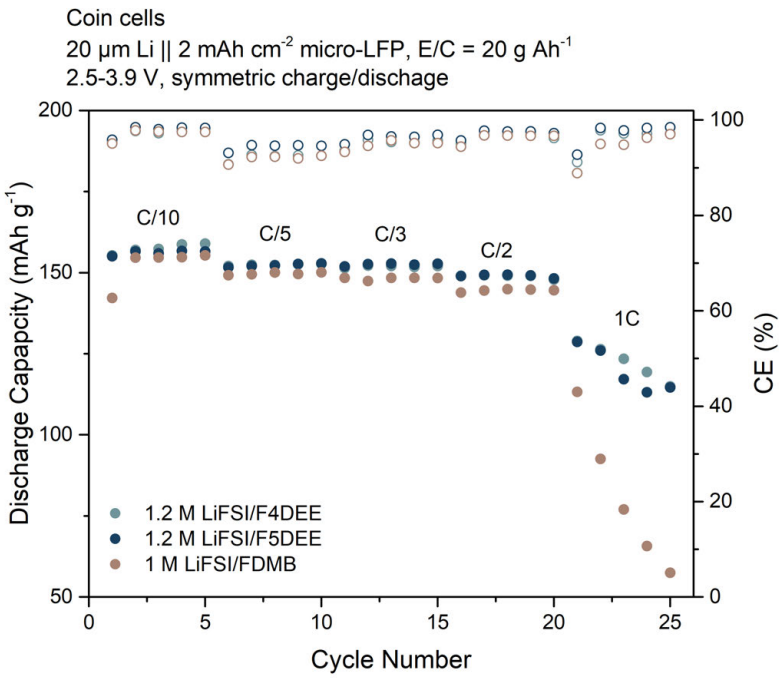

Supplementary Fig. 37. Rate capability tests fluorinated-DEE electrolytes using 20 µm Li || ~2 mAh cm^{-2} microparticle-LFP coin cells. Symmetric charge and discharge were applied.

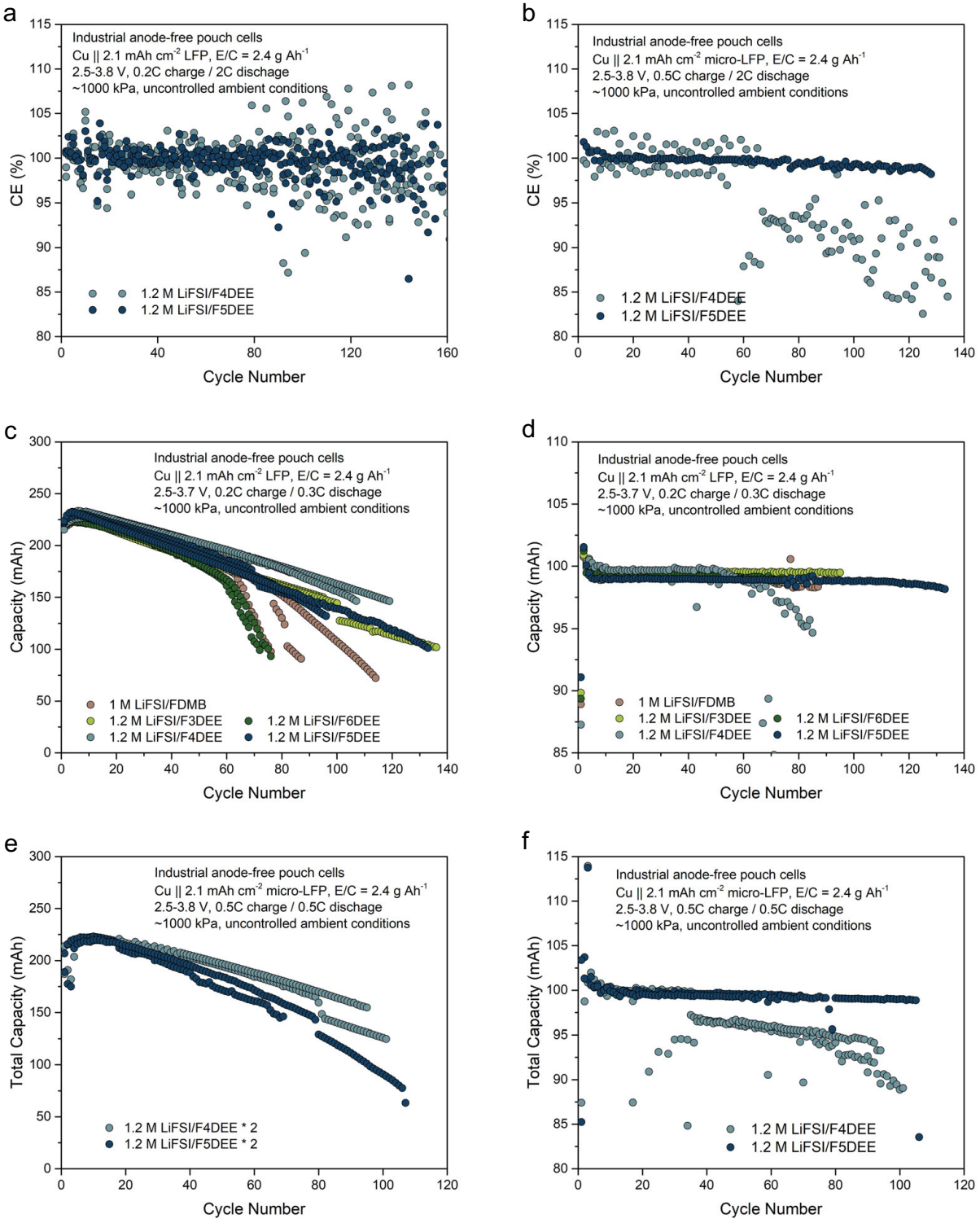

Supplementary Fig. 38. Cycling performance of Cu || ~2.1 mAh cm^{-2} microparticle-LFP anode-free pouch cells using fluorinated-DEE electrolytes. (a) CE of cells cycled at 0.2C charge 2C discharge. (b) CE of cells cycled at 0.5C charge 2C discharge. (c,d) Capacity retention and CE of cells cycled at 0.2C charge 0.3C discharge. (e,f) Capacity retention and CE of cells cycled at 0.5C charge 0.5C discharge.

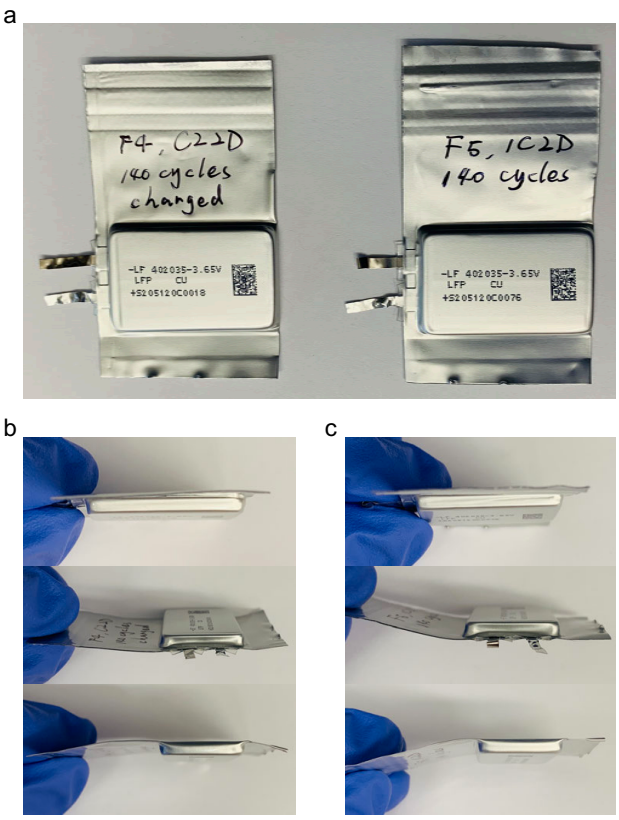

Supplementary Fig. 39. Optical images of the Cu || microparticle-LFP pouch cells using 1.2 M LiFSI/F4DEE (left of a and b) and 1.2 M LiFSI/F5DEE (right of a and c) after 140 cycles.

Note: No obvious gassing issue was observed for both electrolytes under different yet fast cycling conditions (0.5C charge 2C discharge for F4DEE and 1C charge 2C discharge for F5DEE), even though no degassing procedure was implemented after initial cycles.

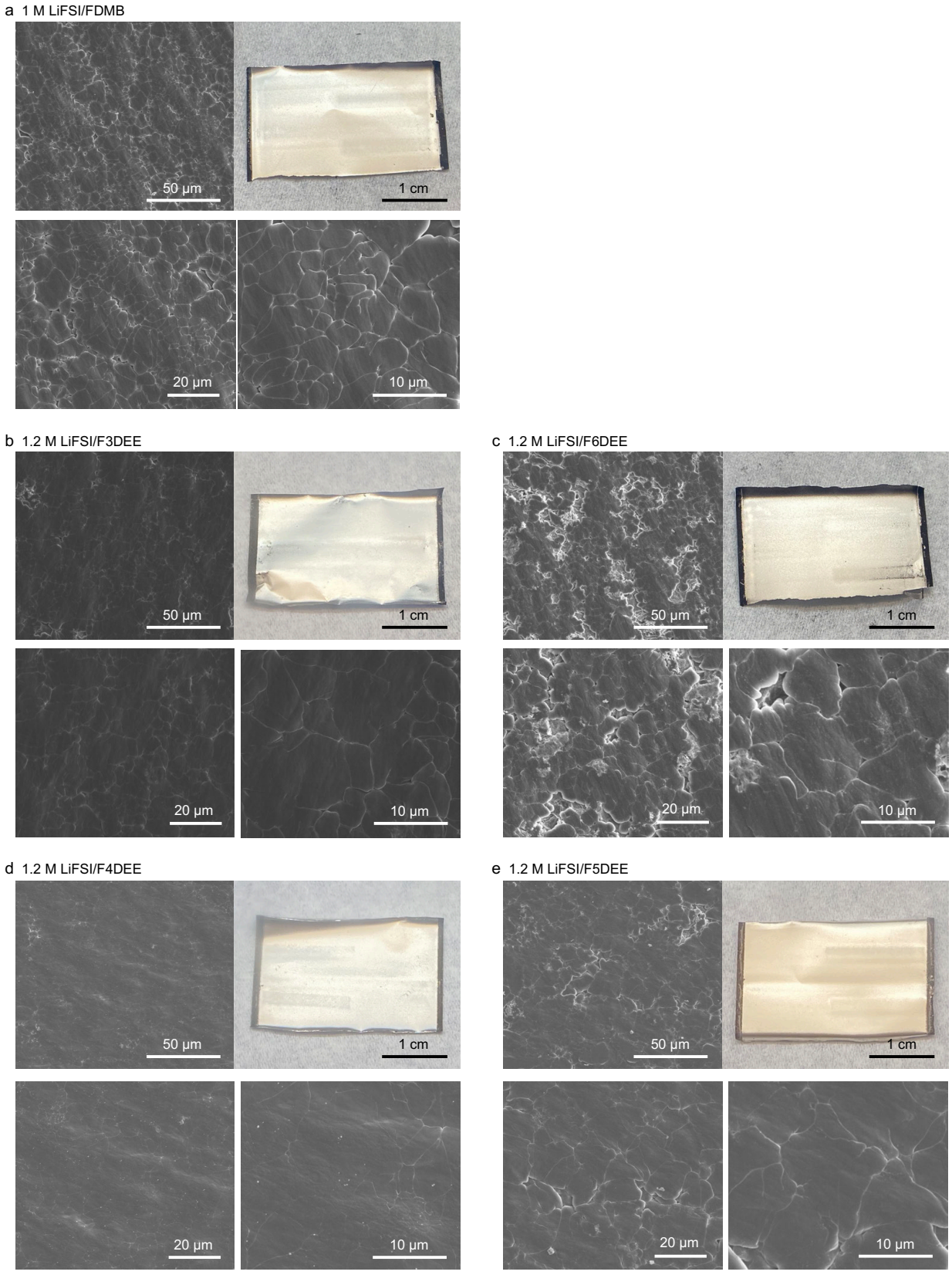

Supplementary Fig. 40. SEM and optical images of the Cu side in Cu || microparticle-LFP pouch cells cycled at 0.2C charge 0.3C discharge for 80 cycles (kept at charged state at last).

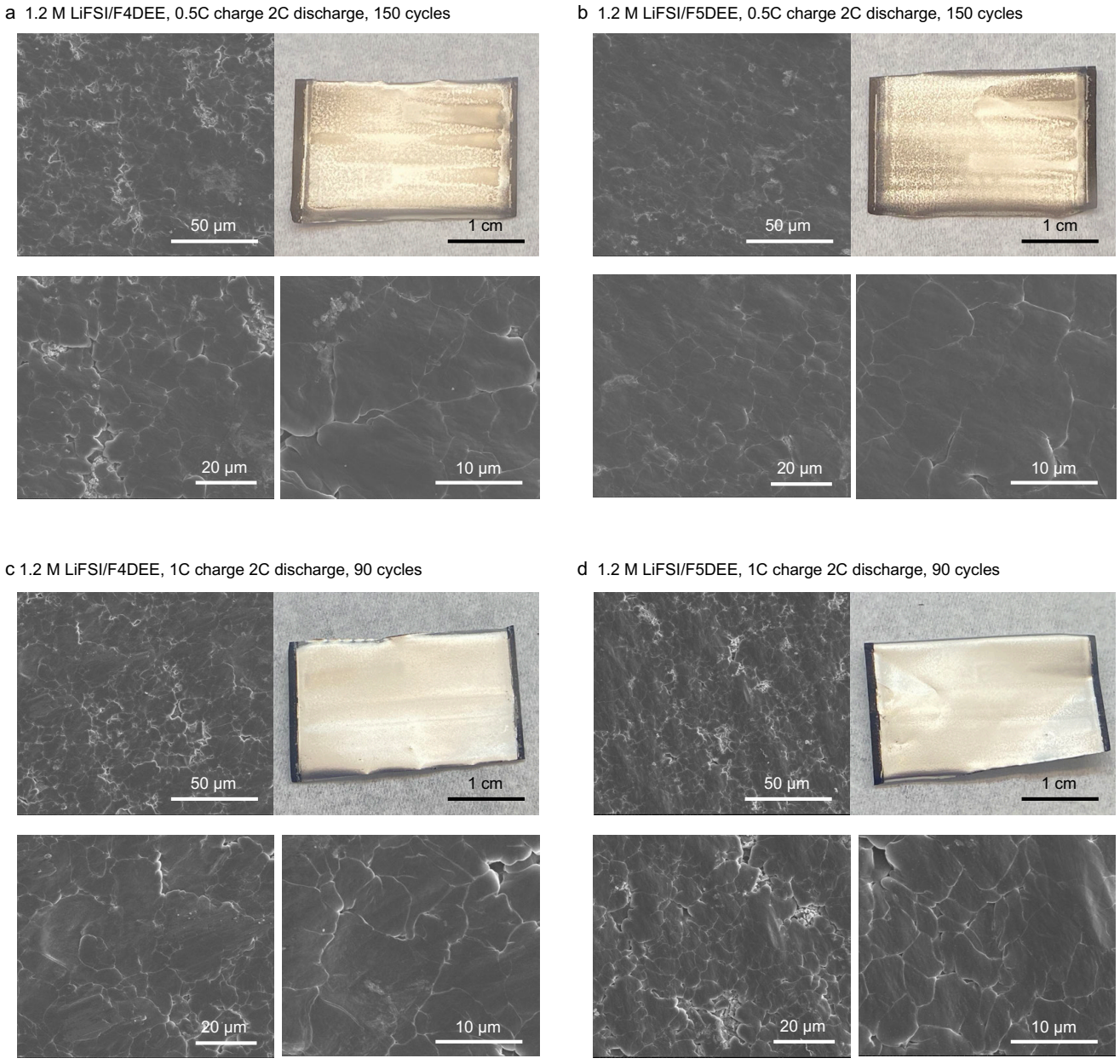

Supplementary Fig. 41. SEM and optical images of the Cu side in Cu || microparticle-LFP pouch cells under fast cycling (kept at charged state at last). (a) 1.2 M LiFSI/F4DEE at 0.5C charge 2C discharge for 150 cycles. (b) 1.2 M LiFSI/F5DEE at 0.5C charge 2C discharge for 150 cycles. (c) 1.2 M LiFSI/F4DEE at 1C charge 2C discharge for 90 cycles. (d) 1.2 M LiFSI/F5DEE at 1C charge 2C discharge for 90 cycles.

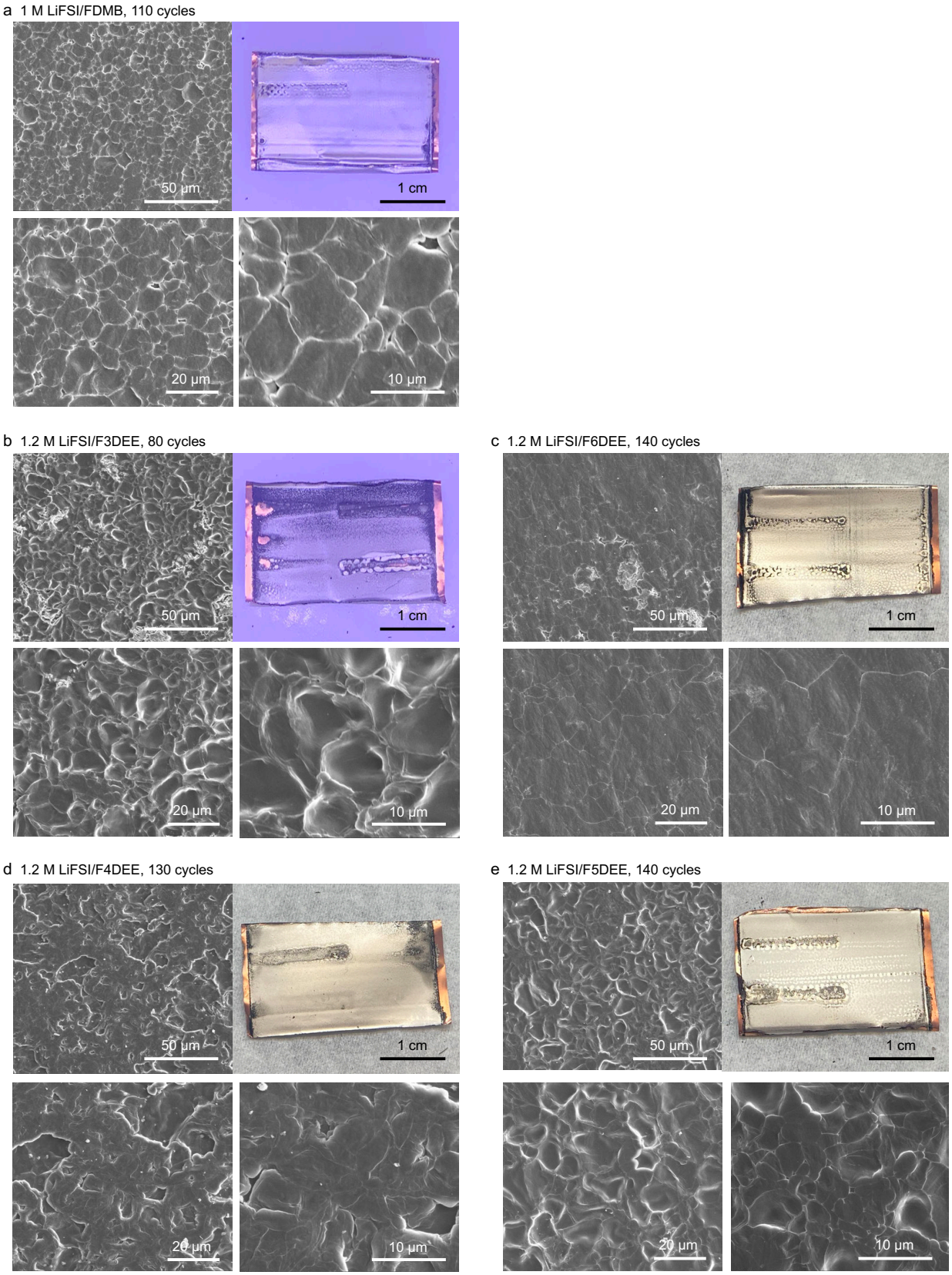

Supplementary Fig. 42. SEM images of the Cu side in Cu || NMC532 pouch cells cycled at 0.2C charge 0.3C discharge (kept at charged state at last).

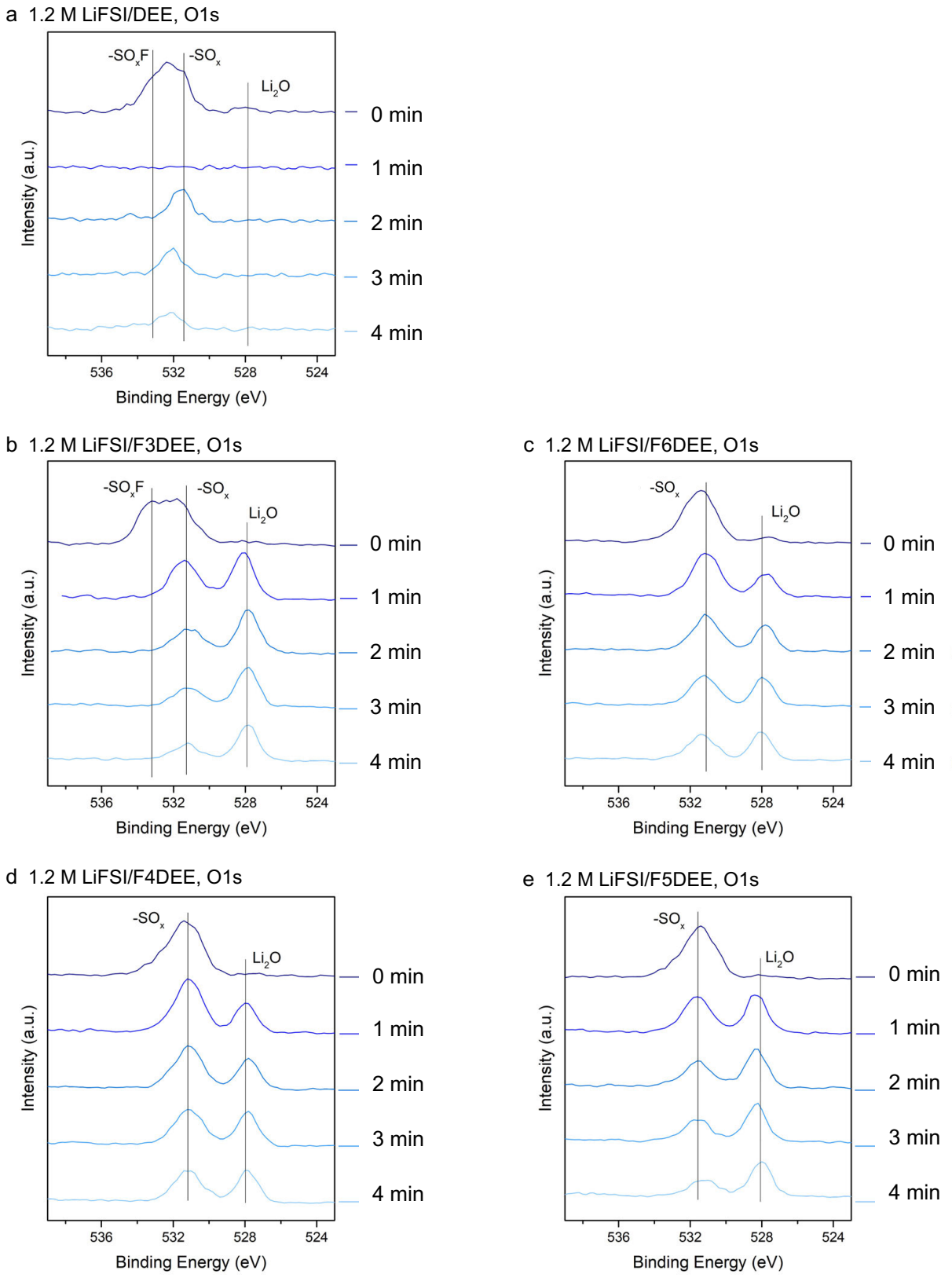

Supplementary Fig. 43. XPS O1s depth profiles of cycled Li metal electrodes using fluorinated-DEE electrolytes.

Note: The O1s signals revealed that Li_2O and $–SO_x$ species dominated in fluorinated-DEE electrolytes. This feature is consistent with cryo-EDS results and has been reported to be both highly interfacial conductive[29,30] and Li metal compatible[8,31].

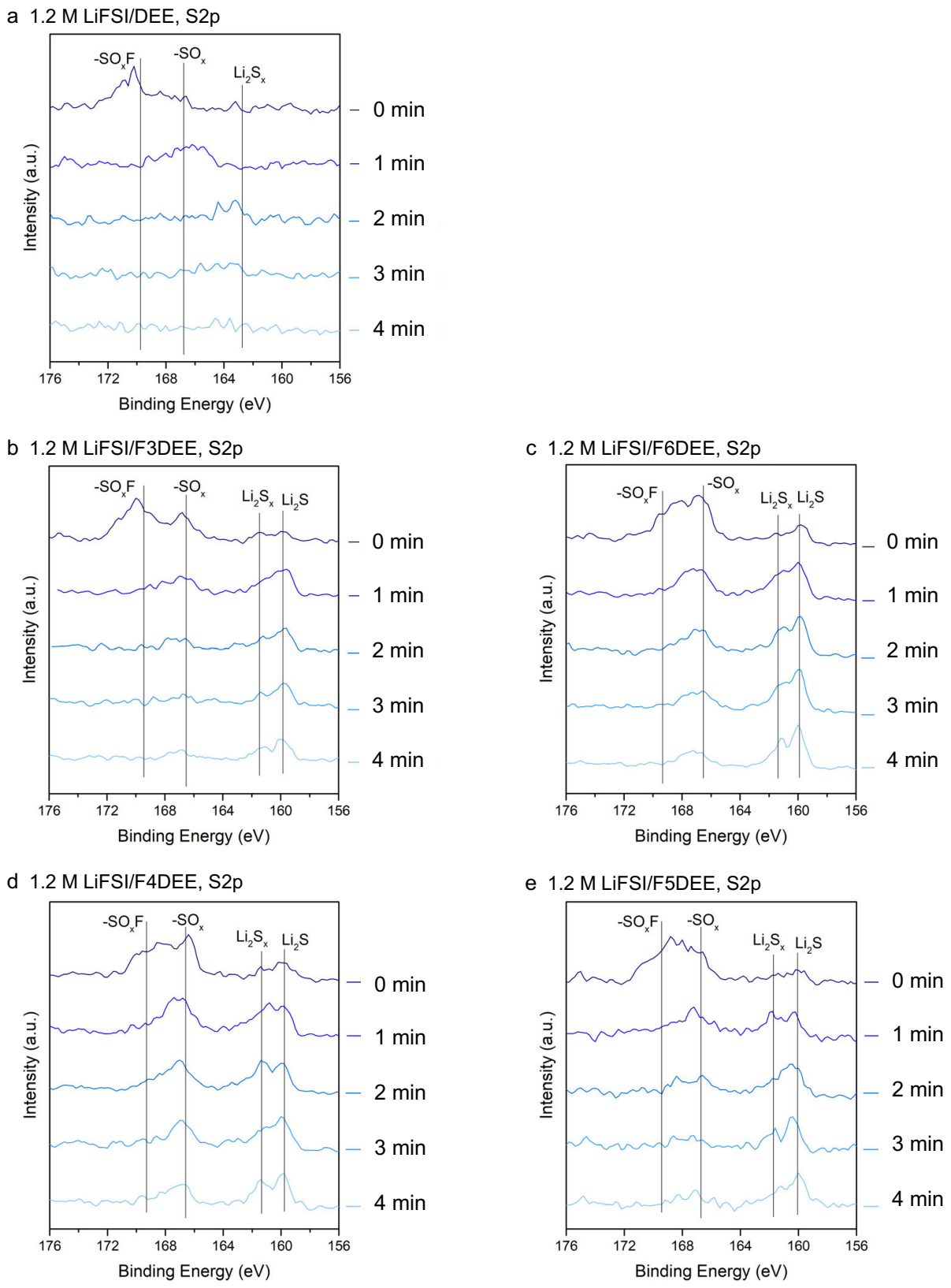

Supplementary Fig. 44. XPS S2p depth profiles of cycled Li metal electrodes using fluorinated-DEE electrolytes.

Note: The S2p signals showed uniformly distributed Li_2S and Li_2S_x species with depth profiling in fluorinated-DEE electrolytes, indicating anion-derived robust SEIs[24,31]; by contrast, only trivial S2p signals existed in the DEE electrolyte.

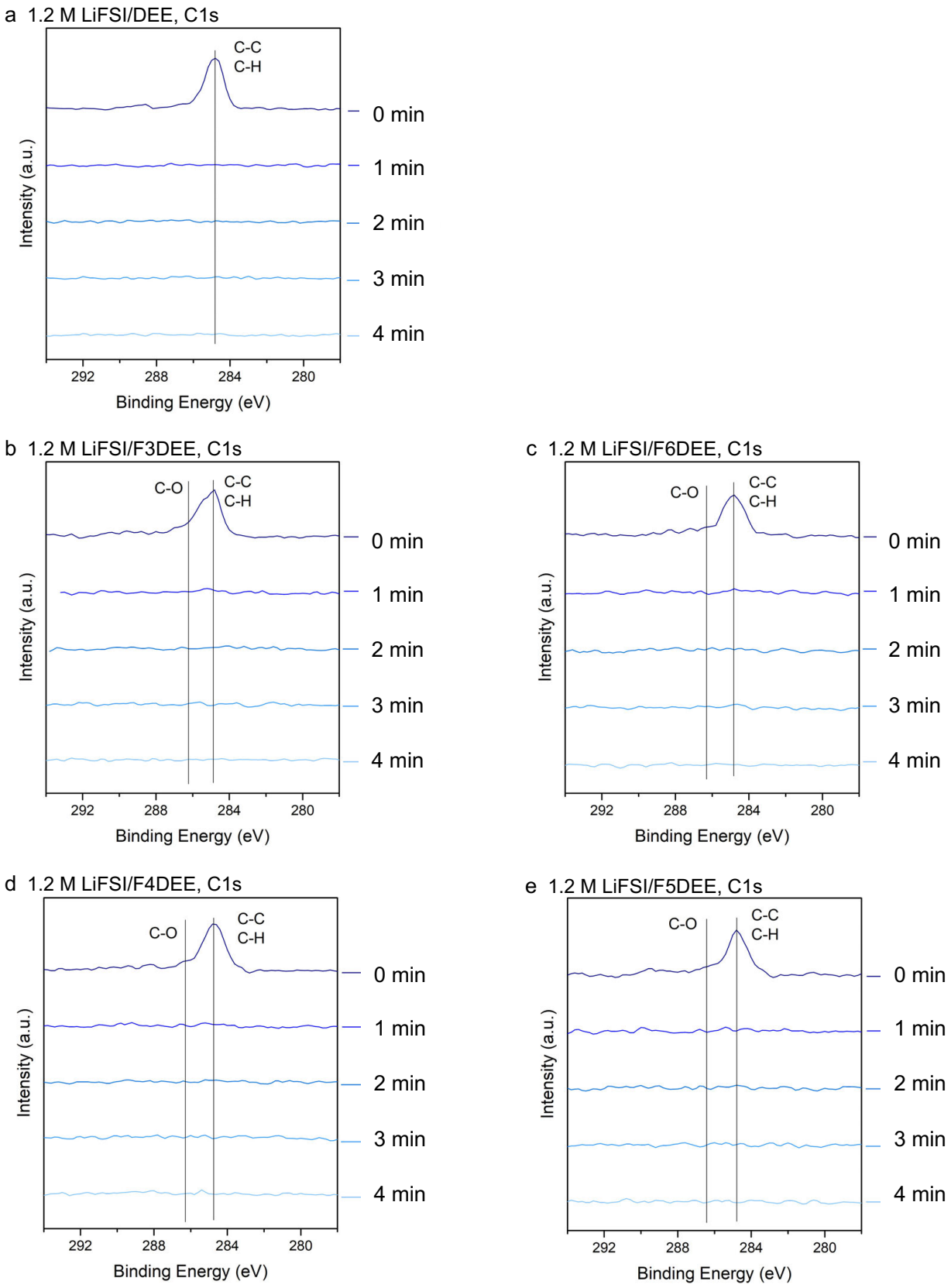

Supplementary Fig. 45. XPS C1s depth profiles of cycled Li metal electrodes using fluorinated-DEE electrolytes.

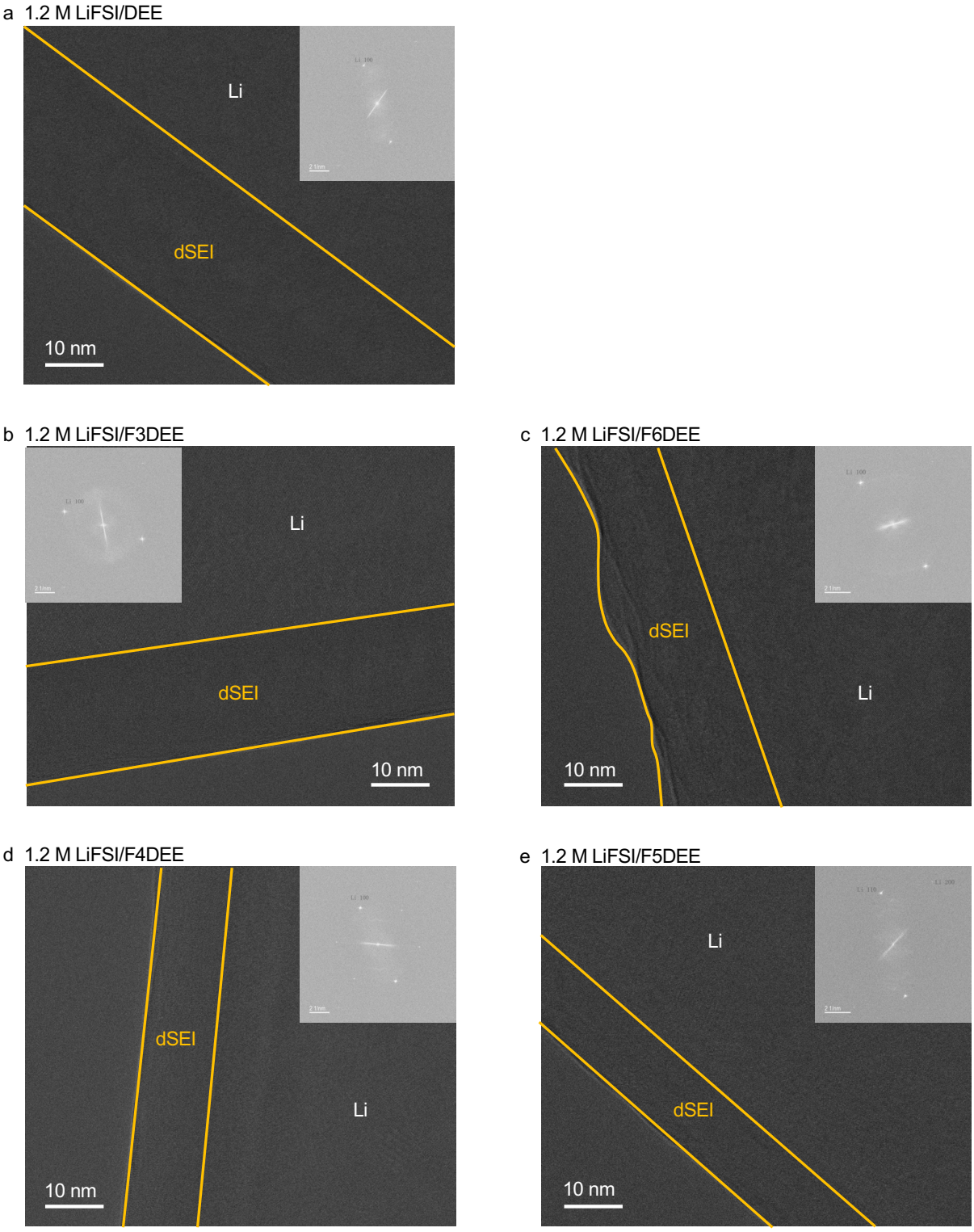

Supplementary Fig. 46. Cryo-TEM images of Li metal deposits using fluorinated-DEE electrolytes.

Note: The direct SEIs (dSEIs) on Li surface in F4DEE and F5DEE electrolytes were thinner than others while that in F6DEE showed wavy structure (non-uniformity). The one in DEE electrolyte was the thickest dSEI. All these facts were consistent with our battery results especially Li metal CE.

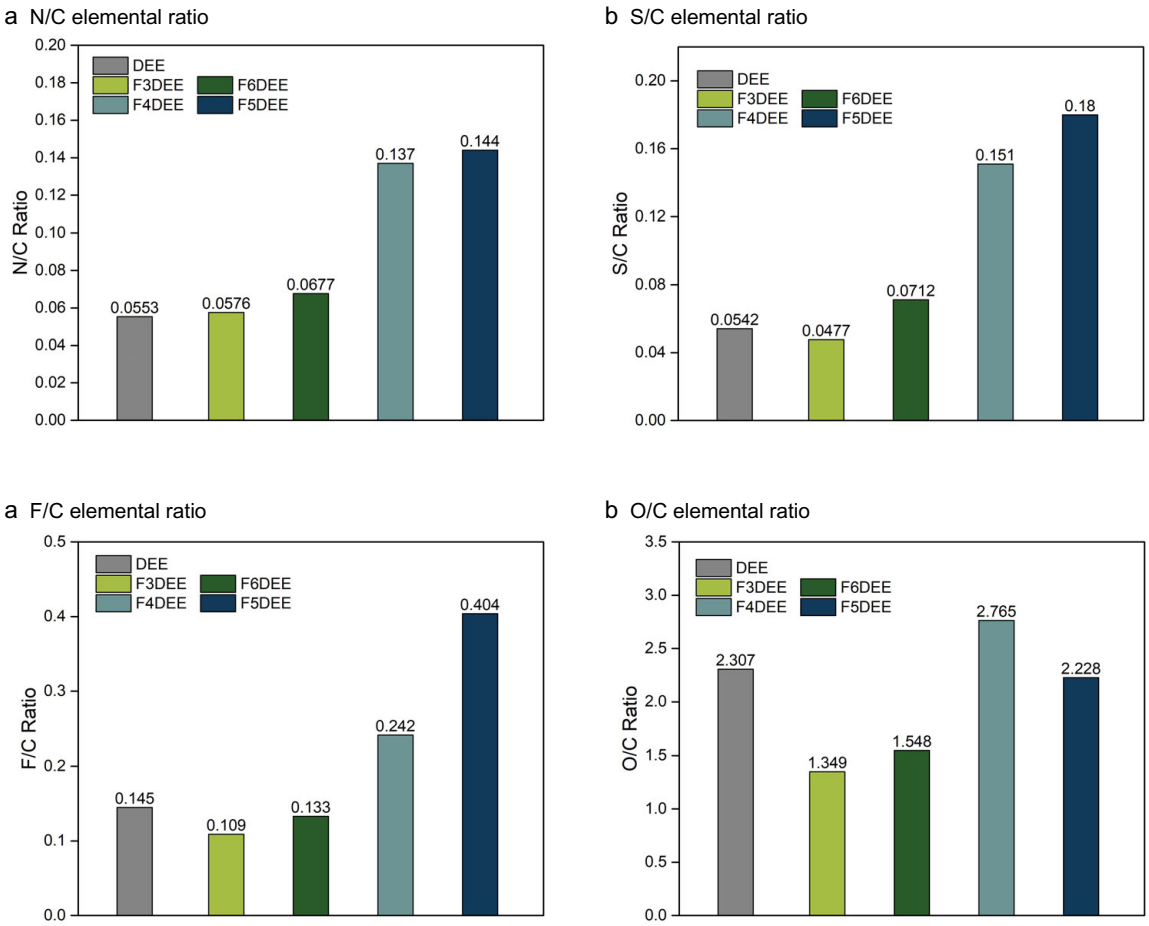

Supplementary Fig. 47. Different elemental ratios obtained from cryo-EDS of Li metal deposits using fluorinated-DEE electrolytes.

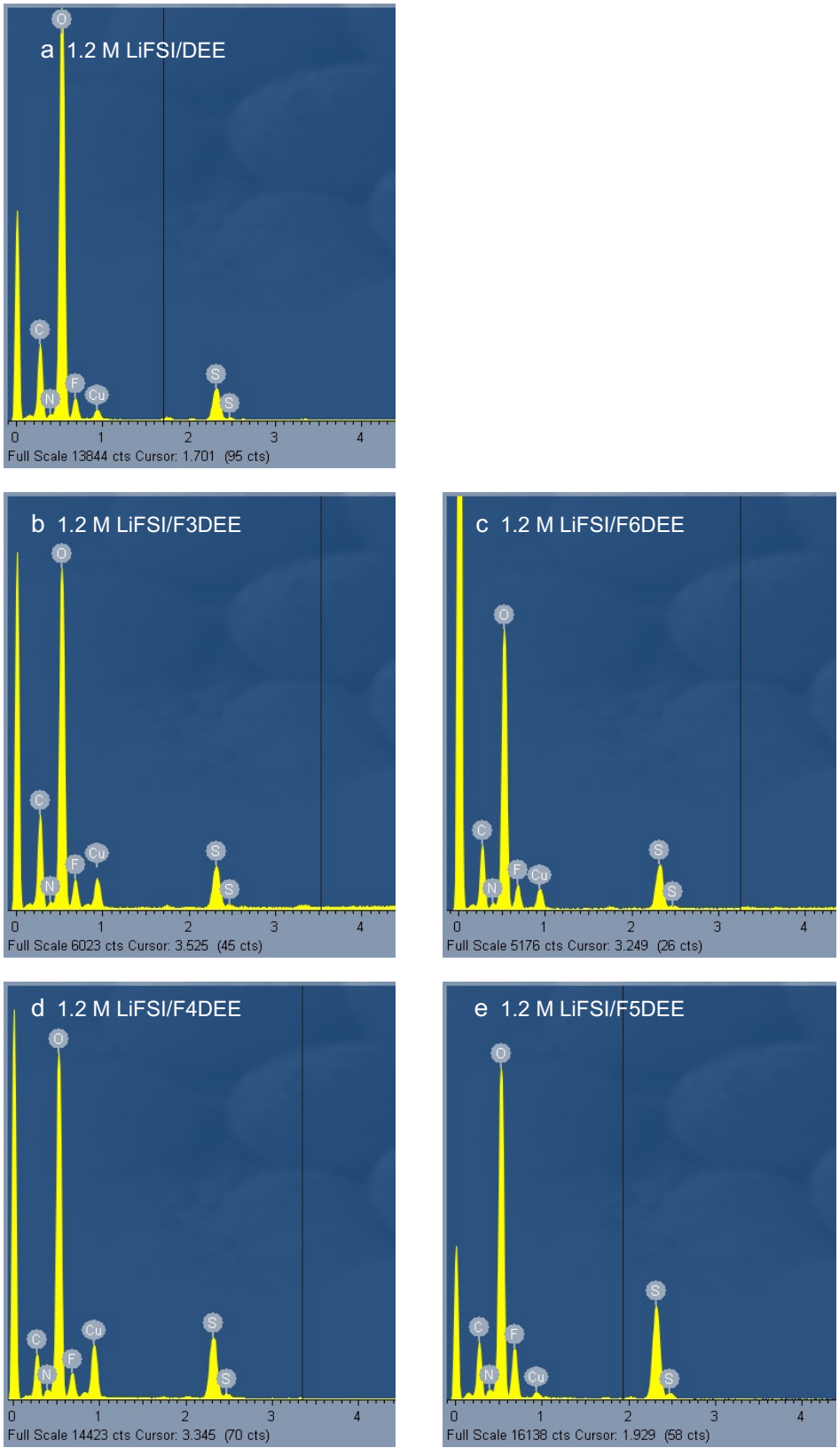

Supplementary Fig. 48. Cryo-EDS plots of Li metal deposits using fluorinated-DEE electrolytes.

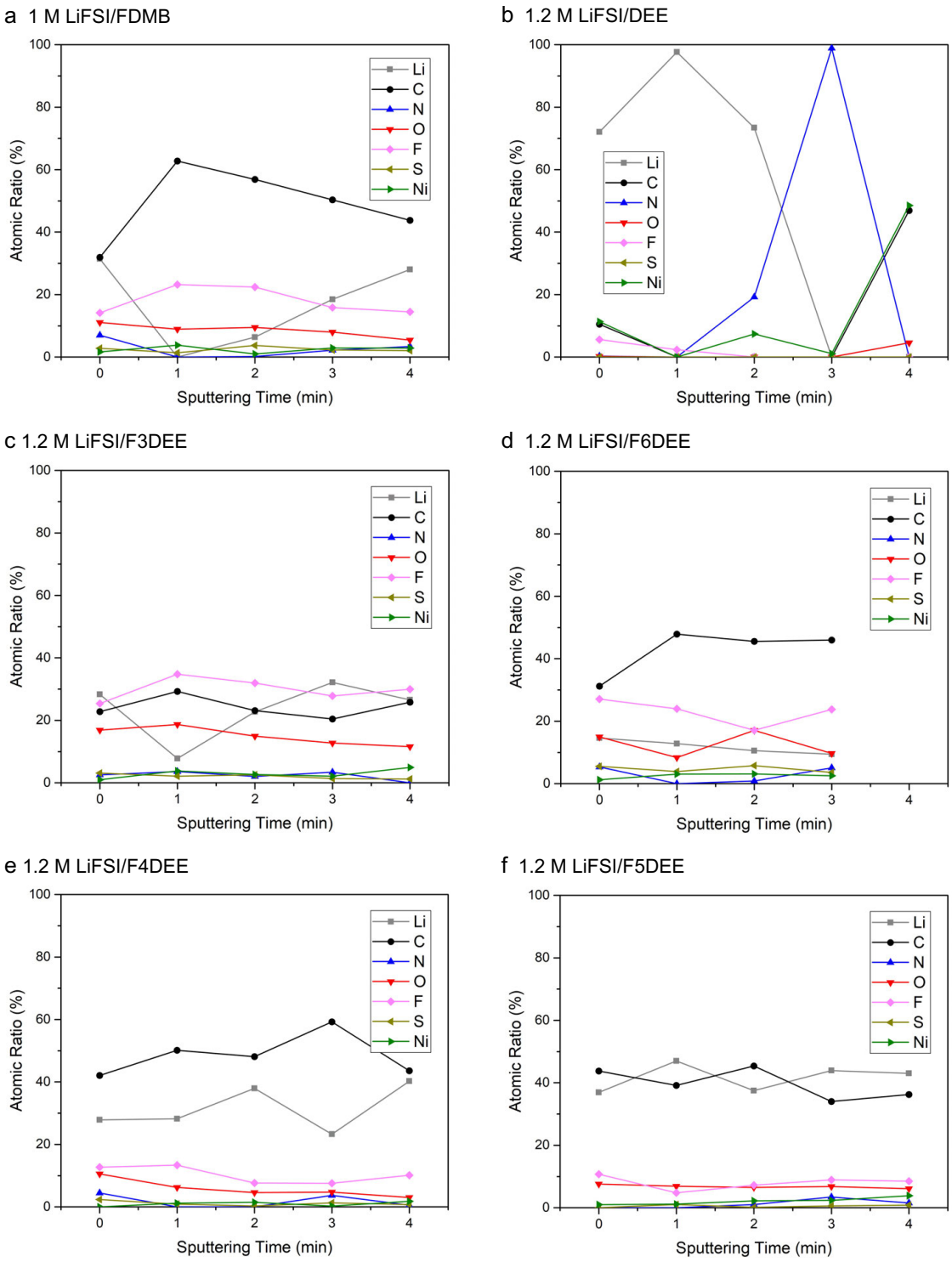

Supplementary Fig. 49. Atomic ratio by XPS with different depths of NMC811 cathodes after 30 cycles.

Note: The atomic ratio of CEI in 1.2 M LiFSI/DEE showed huge fluctuation with depth profiling, and particularly, high Ni content was observed on the initial surface (without sputtering) and after 4-min sputtering, showing the poor passivation of NMC811 in DEE. By contrast, all the fluorinated-DEE and FDMB electrolytes showed high F and C species and negligible Ni content in the CEI, indicating excellent cathode surface protection.

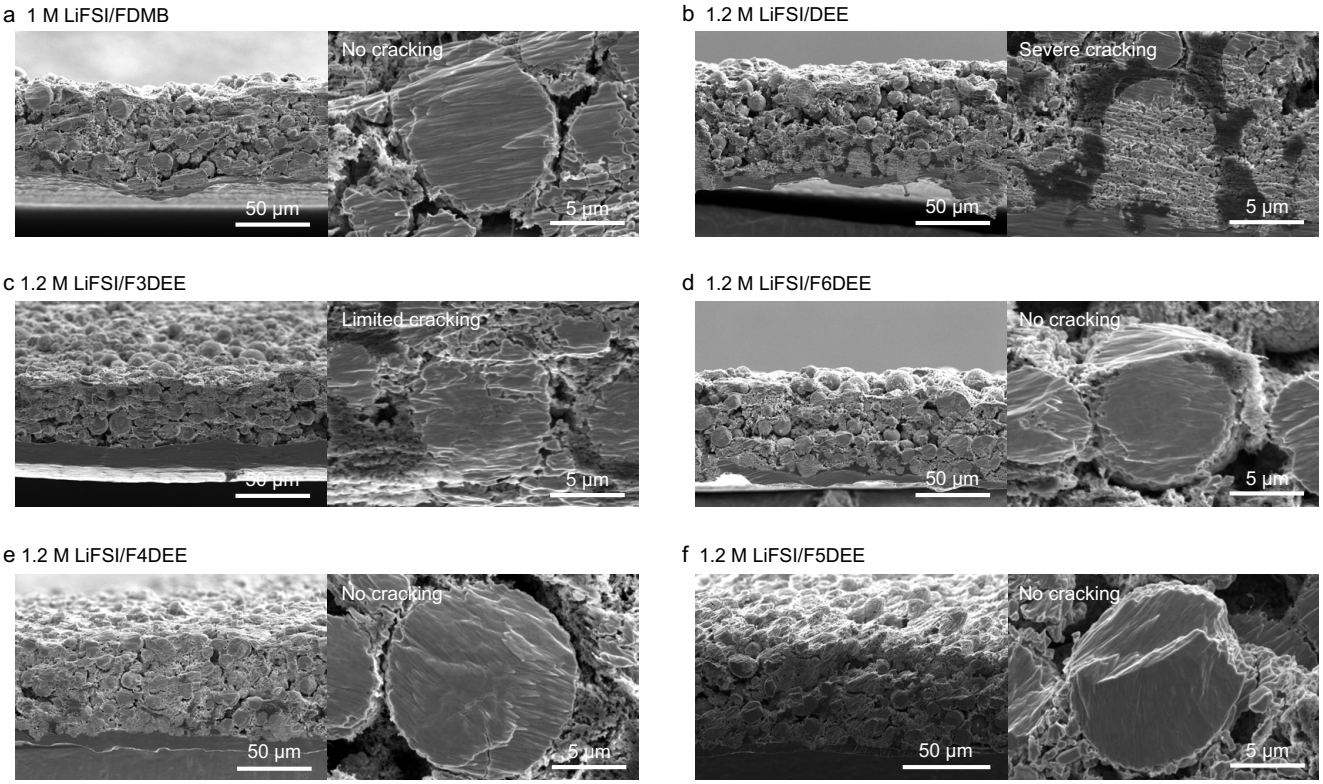

Supplementary Fig. 50. Cross-sectional SEM images of NMC811 cathodes after 30 cycles.

Note: The polycrystalline-NMC811 particles in the 1.2 M LiFSI/DEE electrolyte showed a universal cracking feature and some particles were completely pulverized. By contrast, the cycled NMC811 particles still maintained complete shape or only showed limited cracking in FDMB or fluorinated-DEE electrolytes.

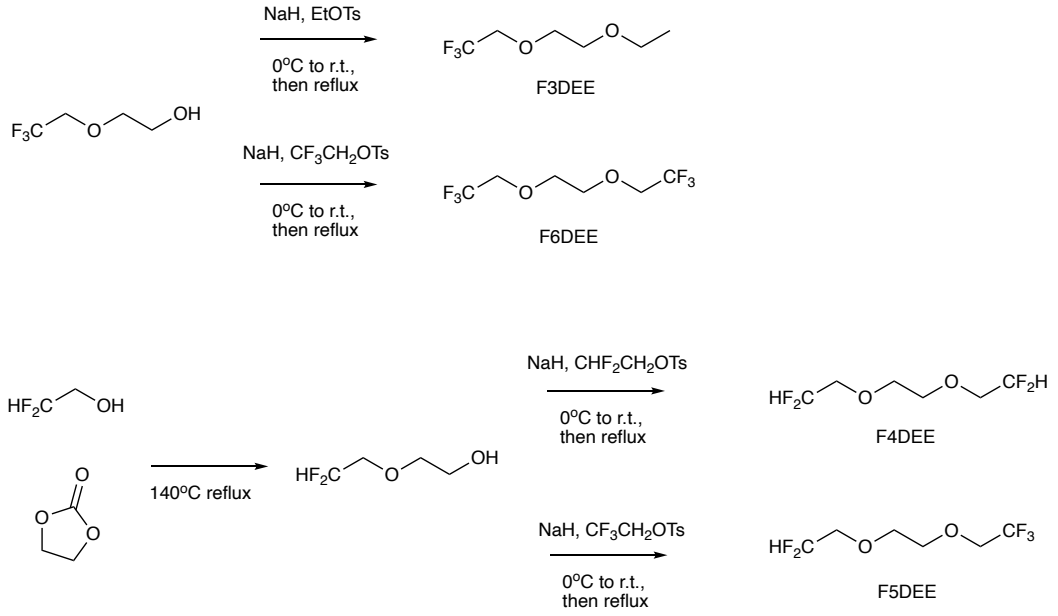

Supplementary Fig. 51. Synthetic scheme of fluorinated-DEEs studied in this work.

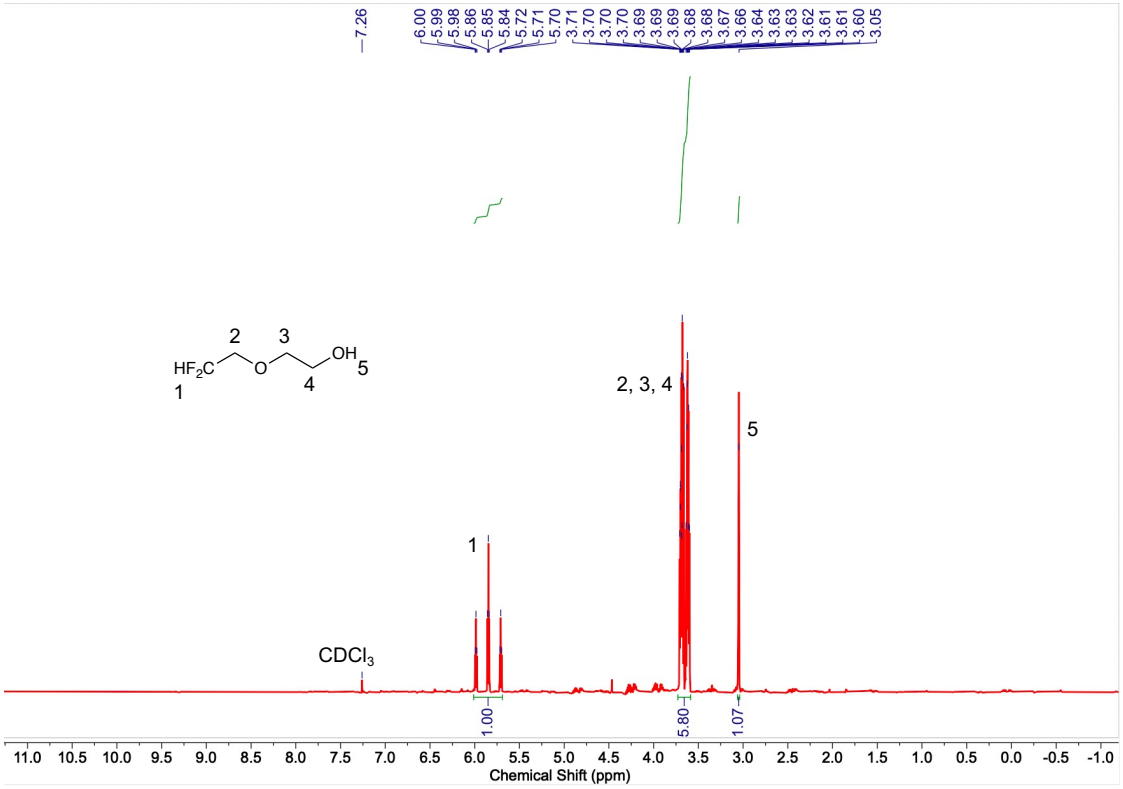

Supplementary Fig. 52. ^{1}H-NMR of 2-(2,2-difluoroethoxy)ethanol (400 MHz, $CDCl_3$, δ/ppm): 6.00 ~ 5.70 (tt, 2H), 3.71 ~ 3.60 (m, 6H), 3.05 (s, 1H).

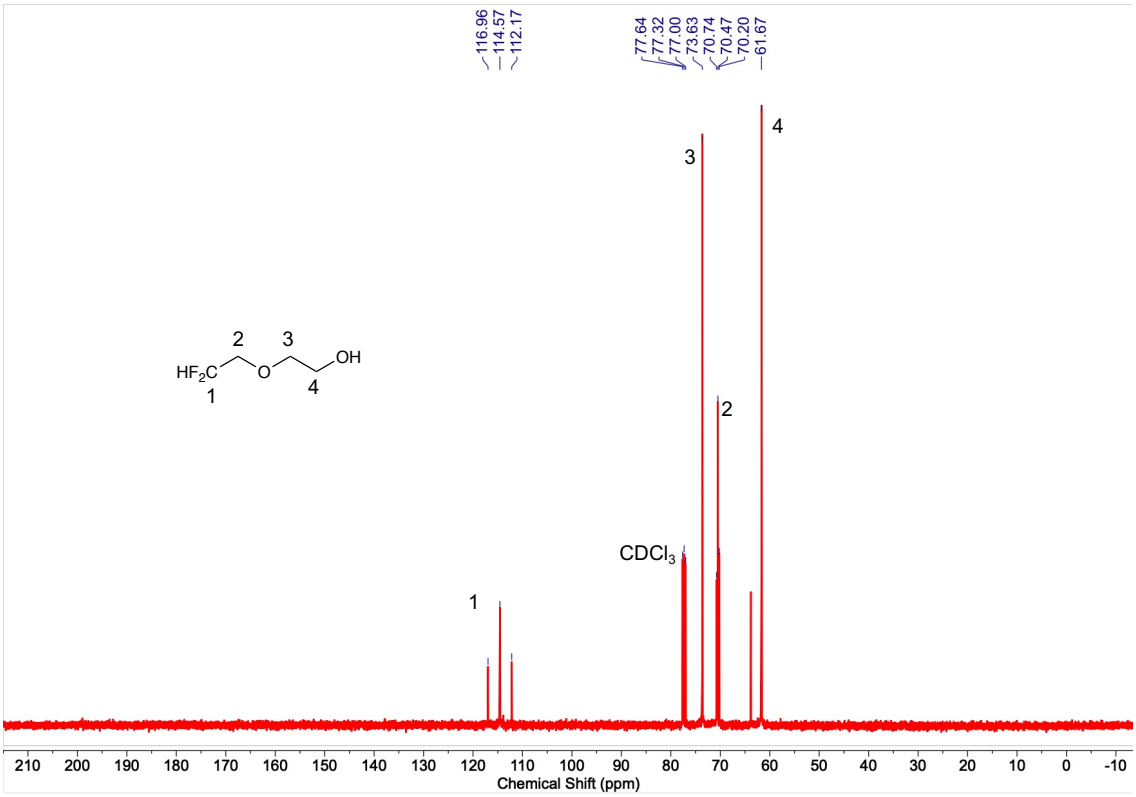

Supplementary Fig. 53. ^{13}C-NMR of 2-(2,2-difluoroethoxy)ethanol (100 MHz, $CDCl_3$, δ/ppm): 116.96 ~ 112.17, 73.63, 70.74 ~ 70.20, 61.67.

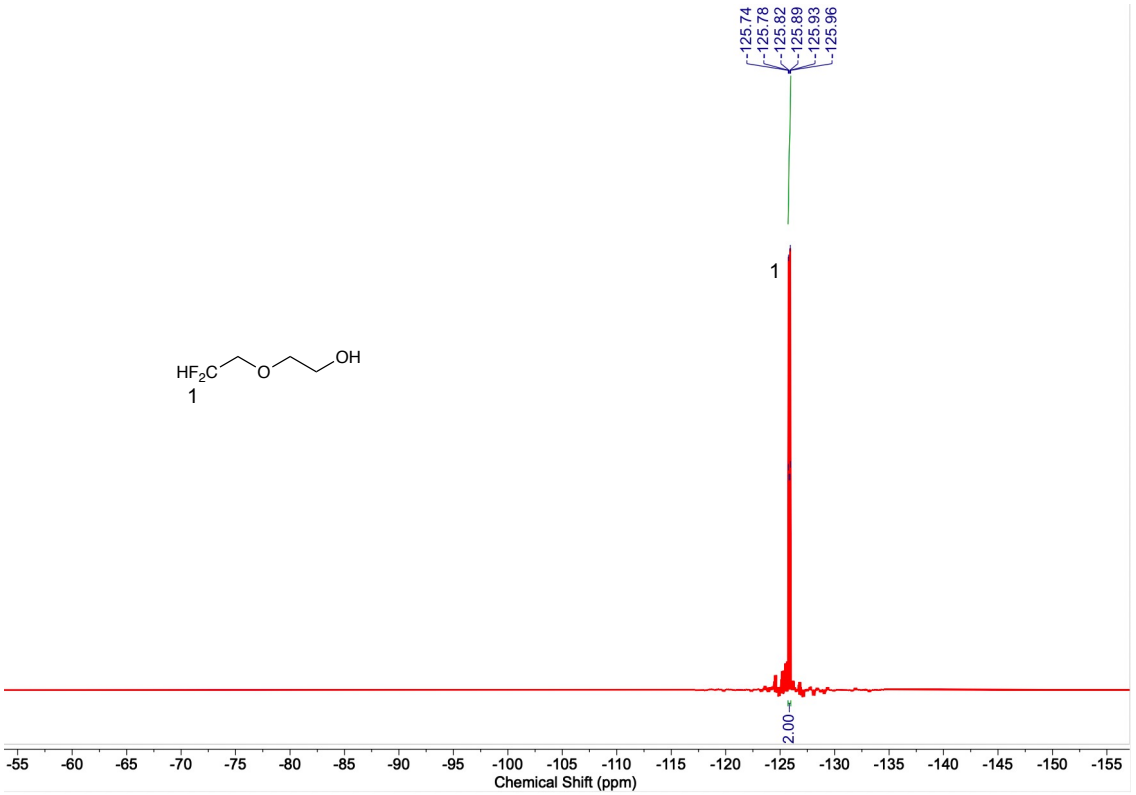

Supplementary Fig. 54. ^{19}F-NMR of 2-(2,2-difluoroethoxy)ethanol (376 MHz, $CDCl_3$, δ/ppm): –125.74 ~ –125.96 (dt, 4F).

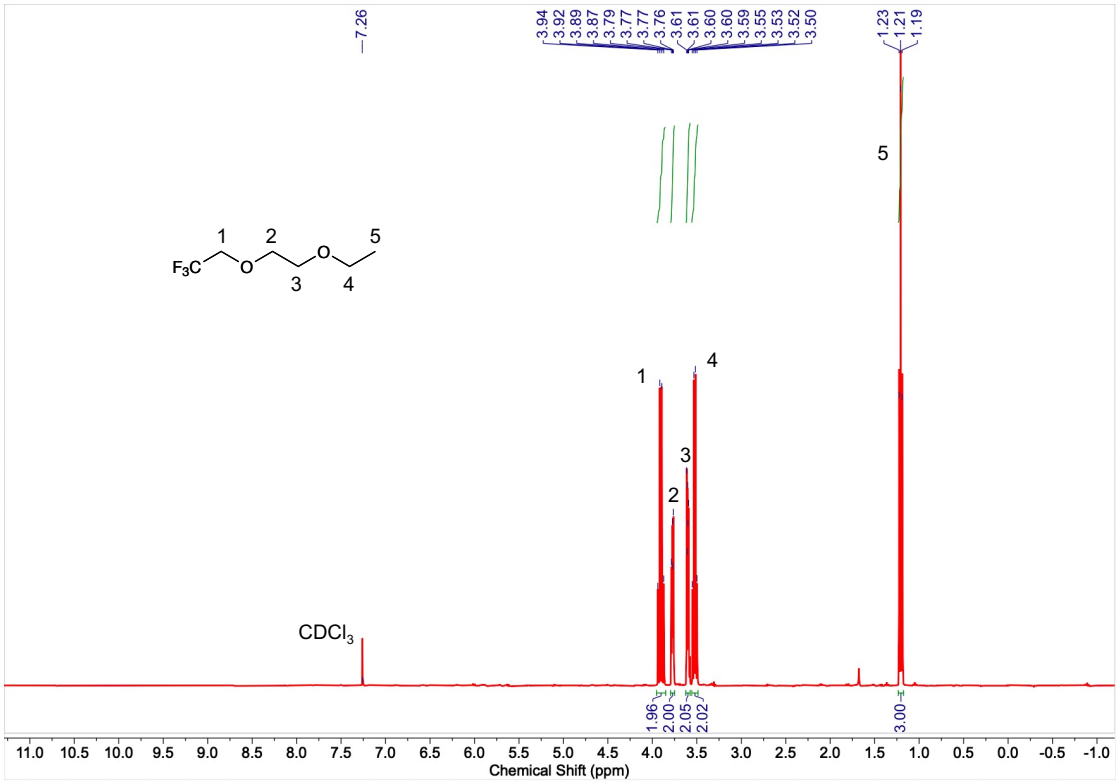

Supplementary Fig. 55. ^{1}H-NMR of F3DEE (400 MHz, $CDCl_3$, δ/ppm): 3.94 ~ 3.87 (q, 2H), 3.77 ~ 3.59 (m, 4H), 3.55 ~ 3.50 (q, 2H), 1.23 ~ 1.19 (3H).

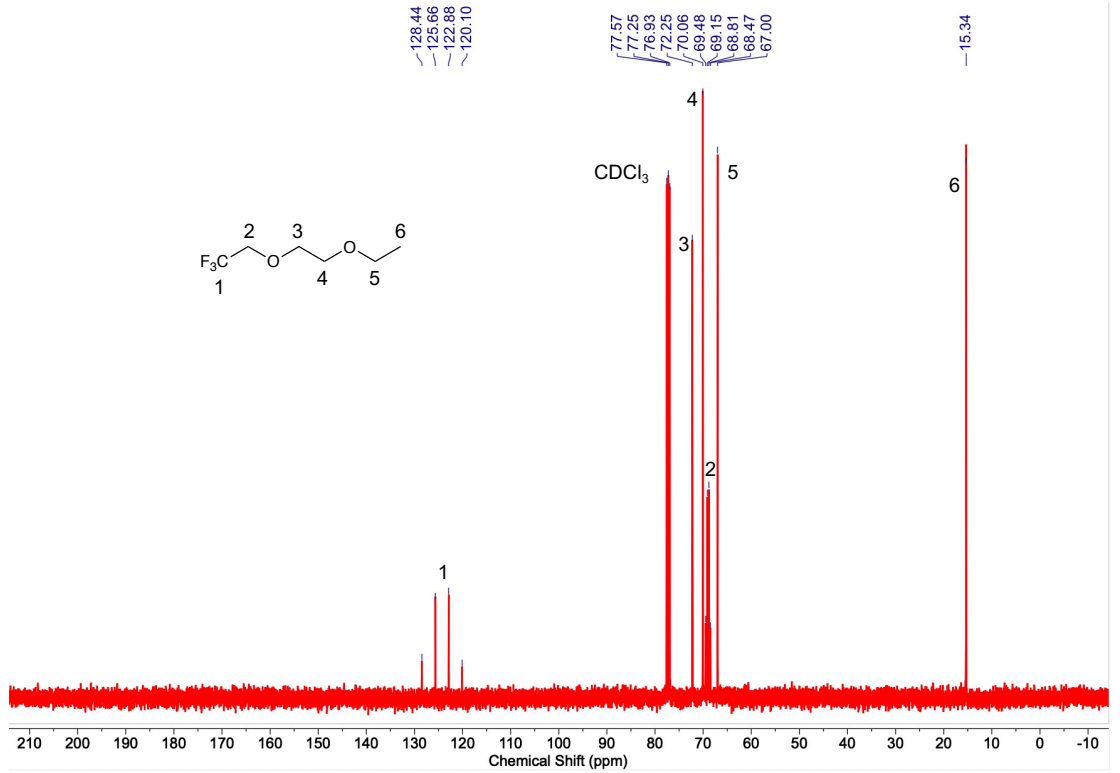

Supplementary Fig. 56. ^{13}C-NMR of F3DEE (100 MHz, $CDCl_3$, δ/ppm): 128.44 ~ 120.10, 72.25, 70.06, 69.48 ~ 68.47, 67.00, 15.34.

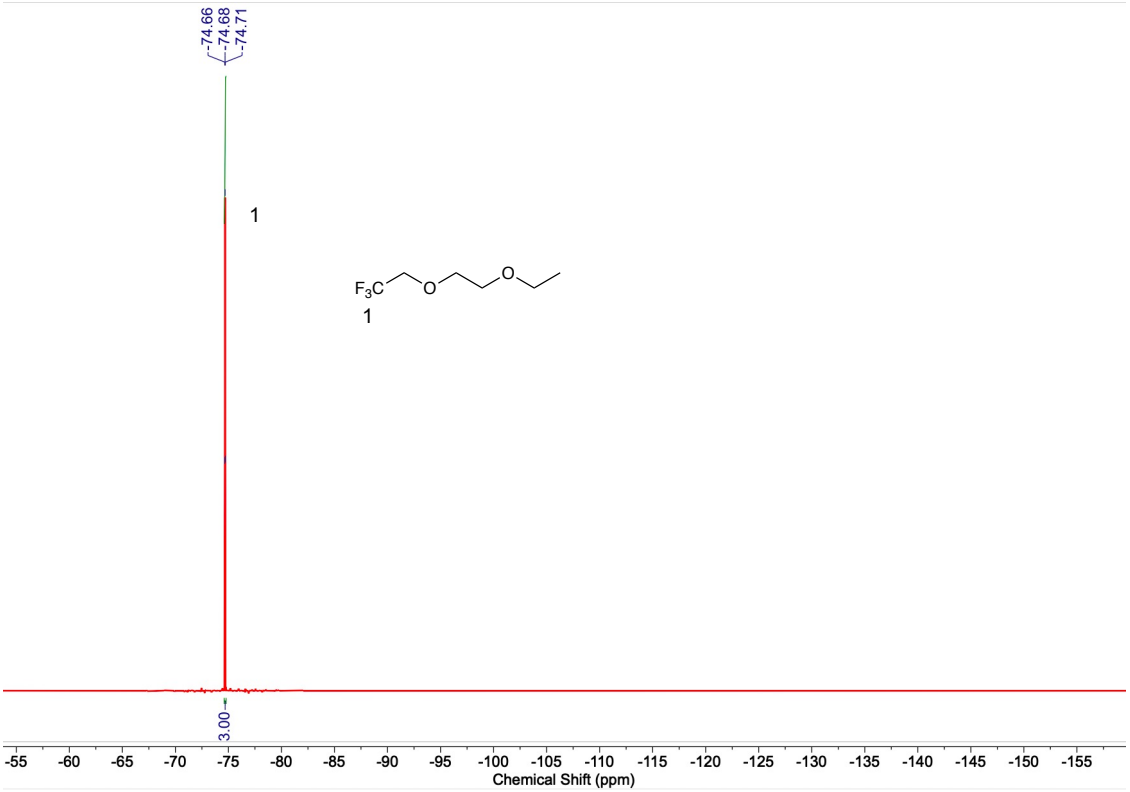

Supplementary Fig. 57. ^{19}F-NMR of F3DEE (376 MHz, $CDCl_3$, δ/ppm): –74.66 ~ –74.71 (t, 3F).

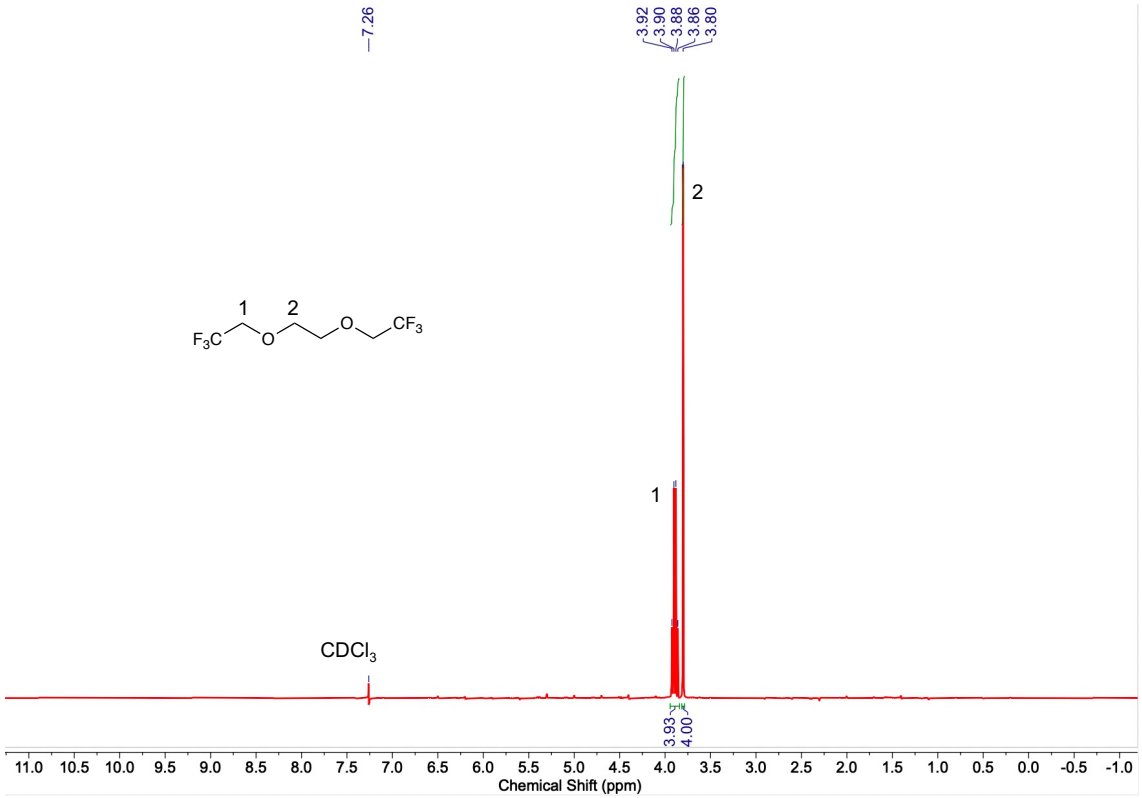

Supplementary Fig. 58. ^{1}H-NMR of F6DEE (400 MHz, $CDCl_3$, δ/ppm): 3.92 ~ 3.86 (q, 4H), 3.80 (s, 4H).

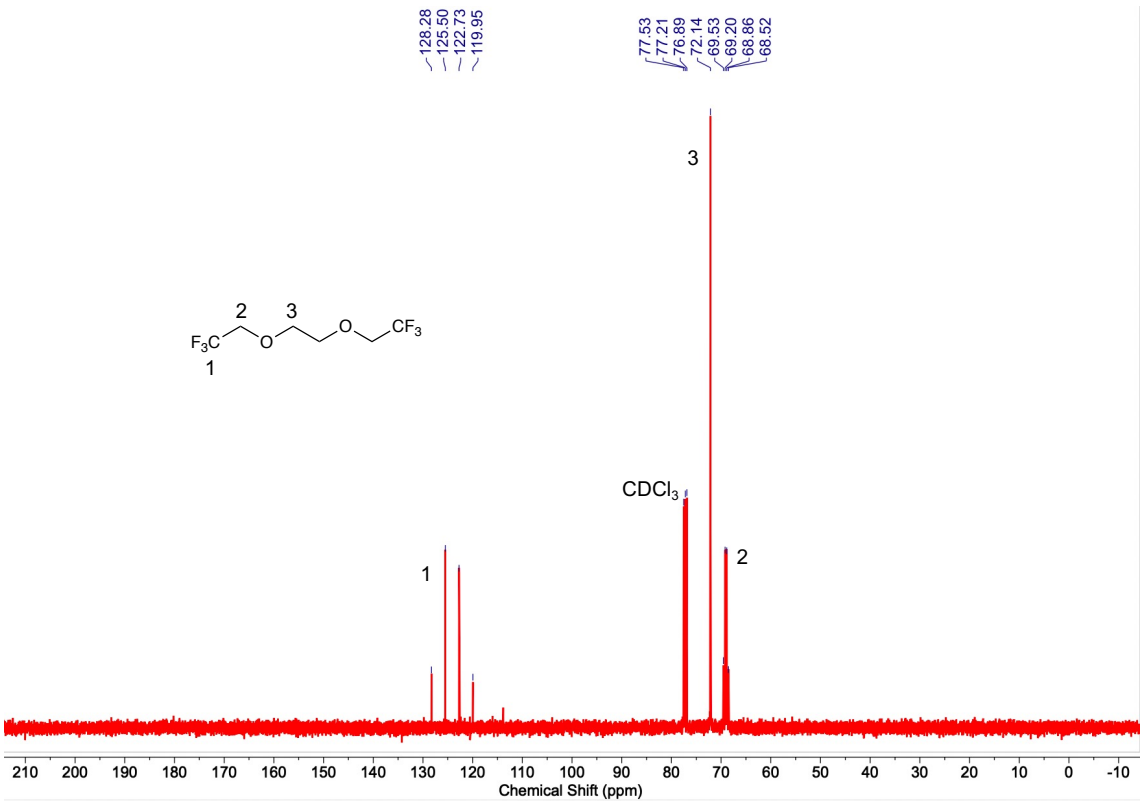

Supplementary Fig. 59. ^{13}C-NMR of F6DEE (100 MHz, $CDCl_3$, δ/ppm): 128.28 ~ 119.95, 72.14, 69.53 ~ 68.52.

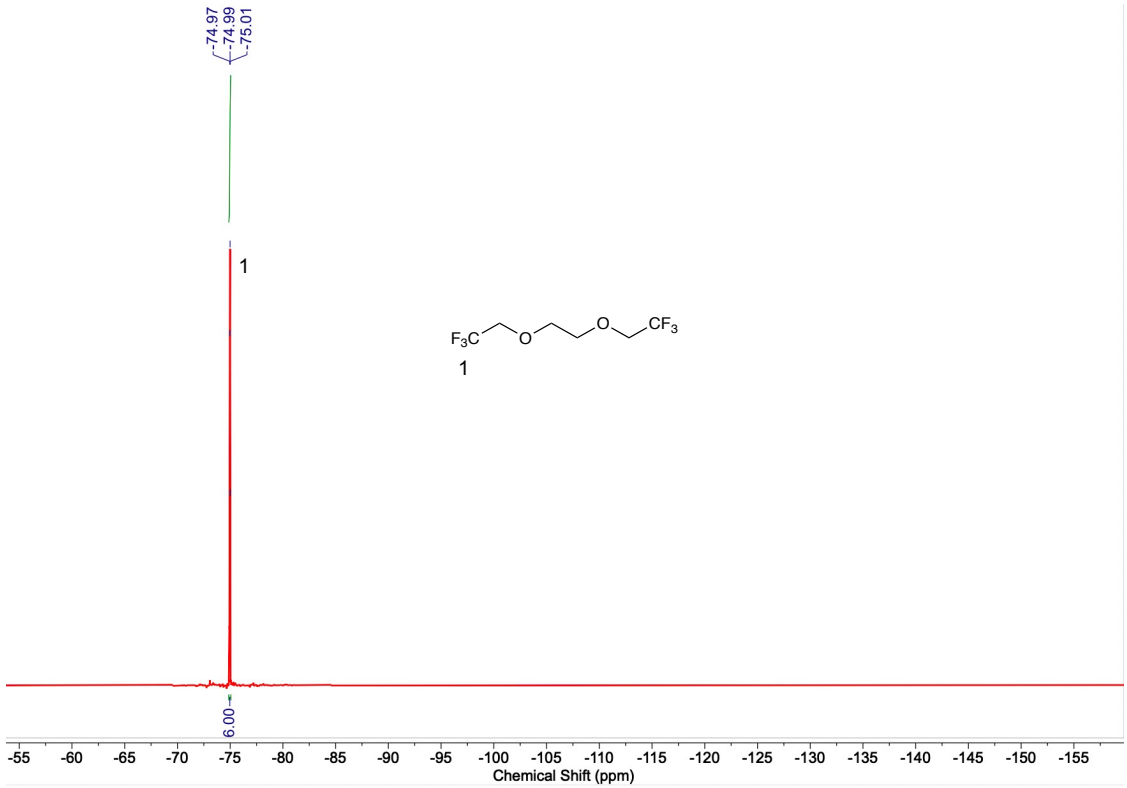

Supplementary Fig. 60. ^{19}F-NMR of F6DEE (376 MHz, $CDCl_3$, δ/ppm): –74.97 ~ –75.01 (t, 6F).

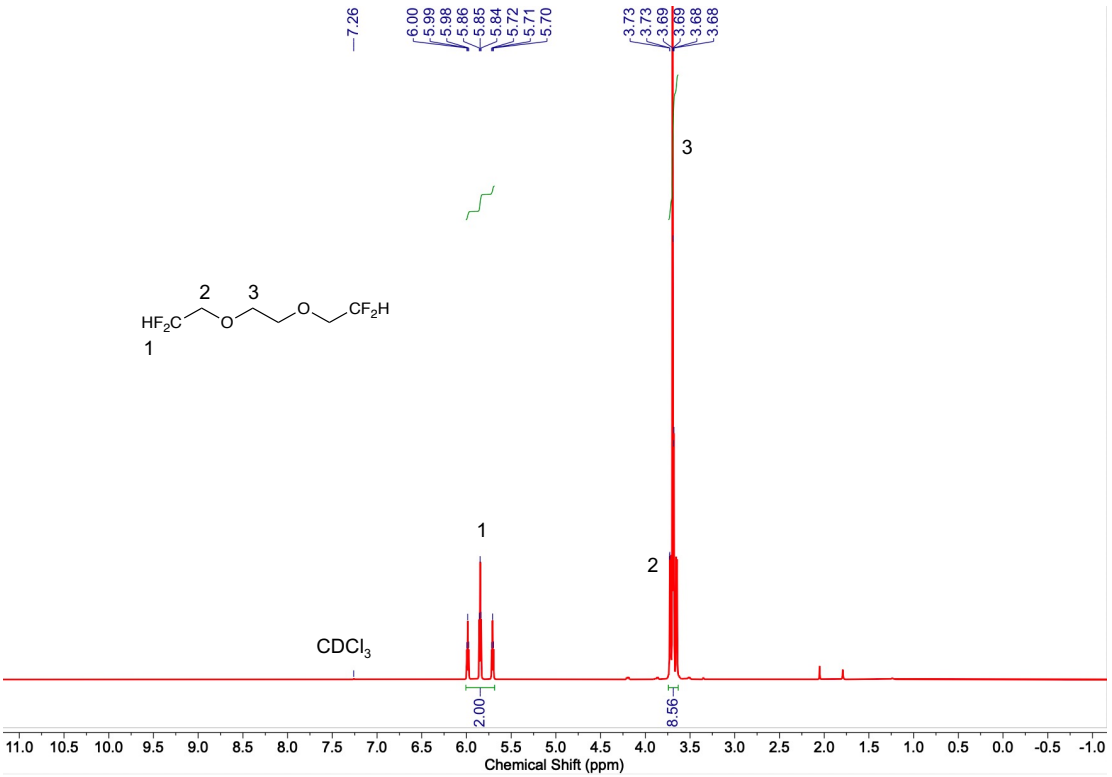

Supplementary Fig. 61. ^{1}H-NMR of F4DEE (400 MHz, $CDCl_3$, δ/ppm): 6.00 ~ 5.70 (tt, 2H), 3.73 ~ 3.68 (td, 4H), 3.69 (s, 4H).

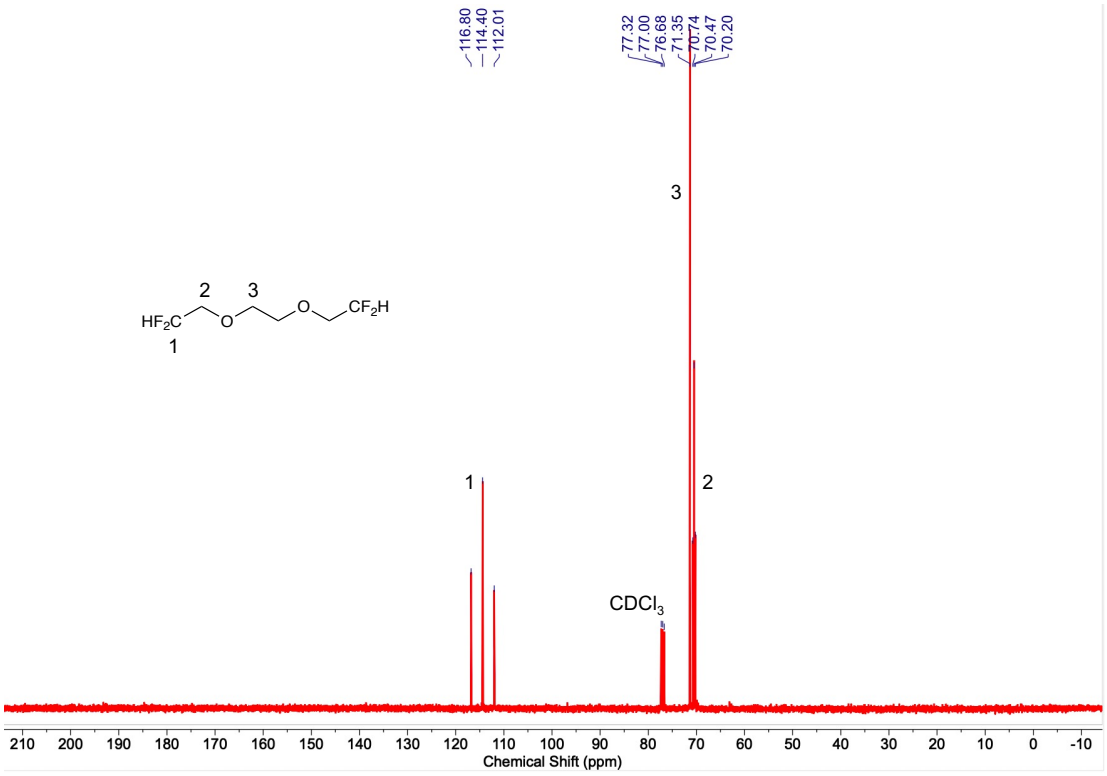

Supplementary Fig. 62. ^{13}C-NMR of F4DEE (100 MHz, $CDCl_3$, δ/ppm): 116.80 ~ 112.01, 71.35, 70.74 ~ 70.20.

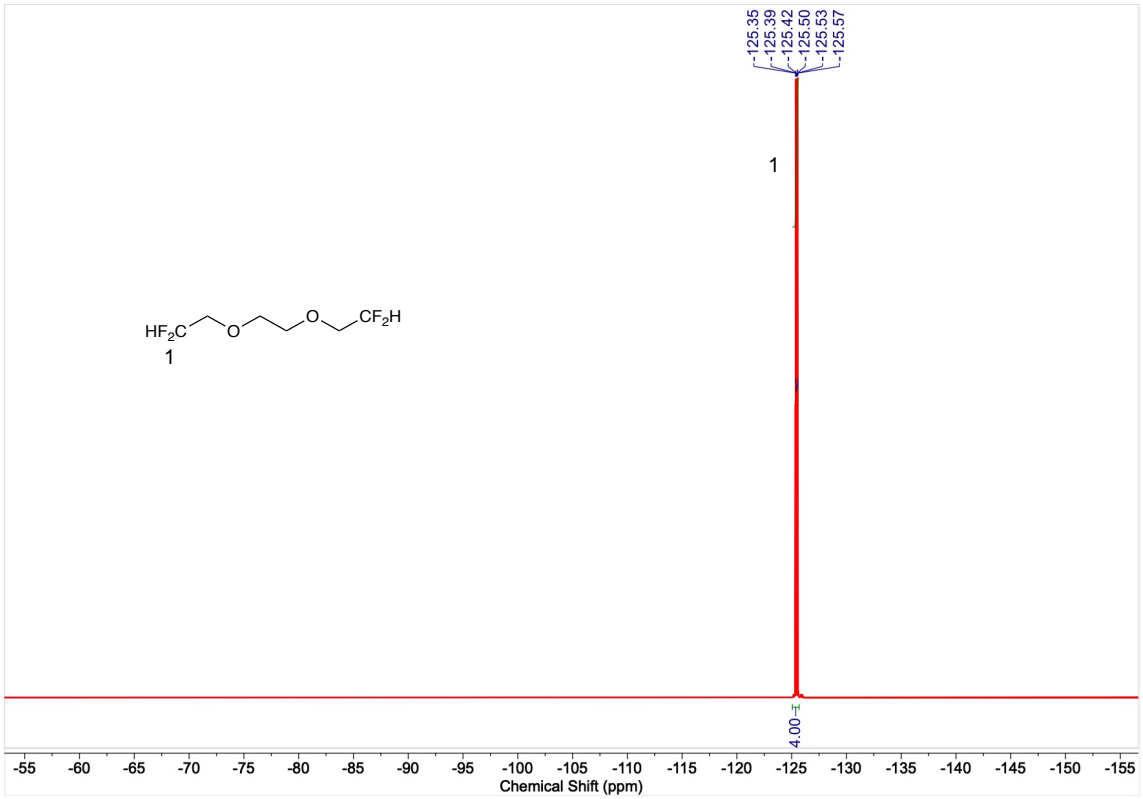

Supplementary Fig. 63. ^{19}F-NMR of F4DEE (376 MHz, $CDCl_3$, δ/ppm): –125.35 ~ –125.57 (dt, 4F).

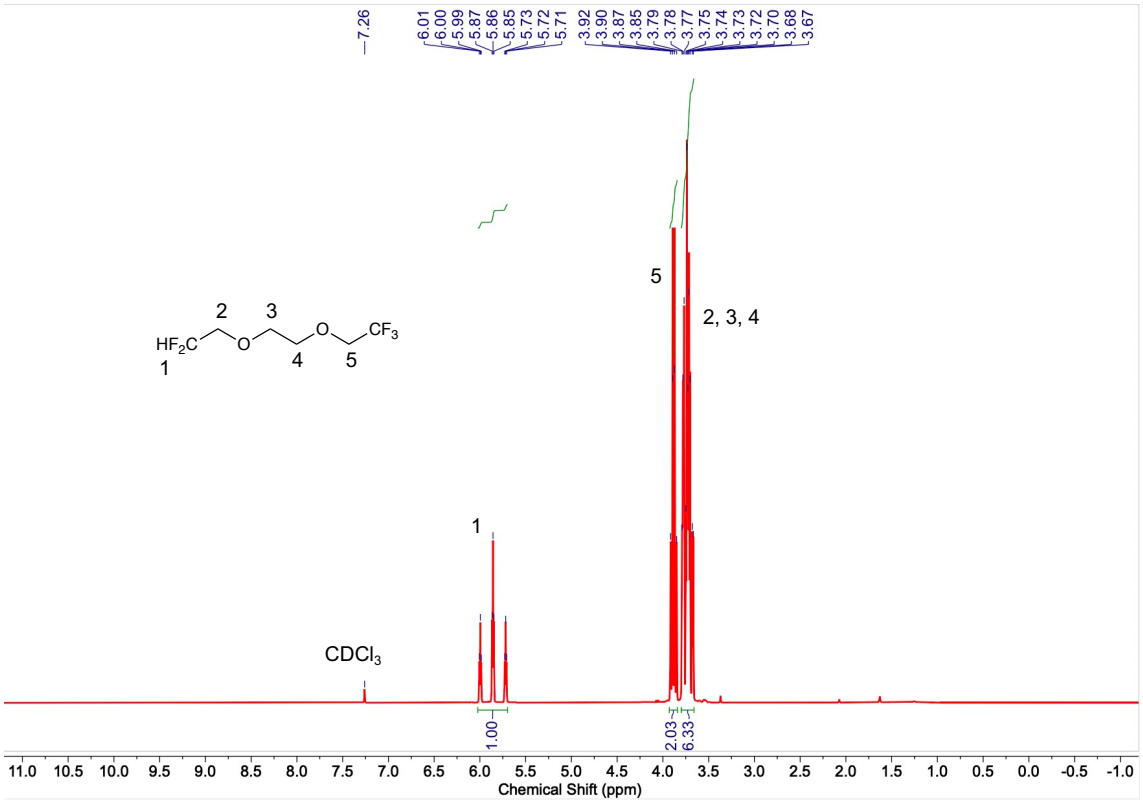

Supplementary Fig. 64. ^{1}H-NMR of F5DEE (400 MHz, $CDCl_3$, δ/ppm): 6.01 ~ 5.71 (tt, 1H), 3.92 ~ 3.85 (td, 2H), 3.79 ~ 3.67 (m, 6H).

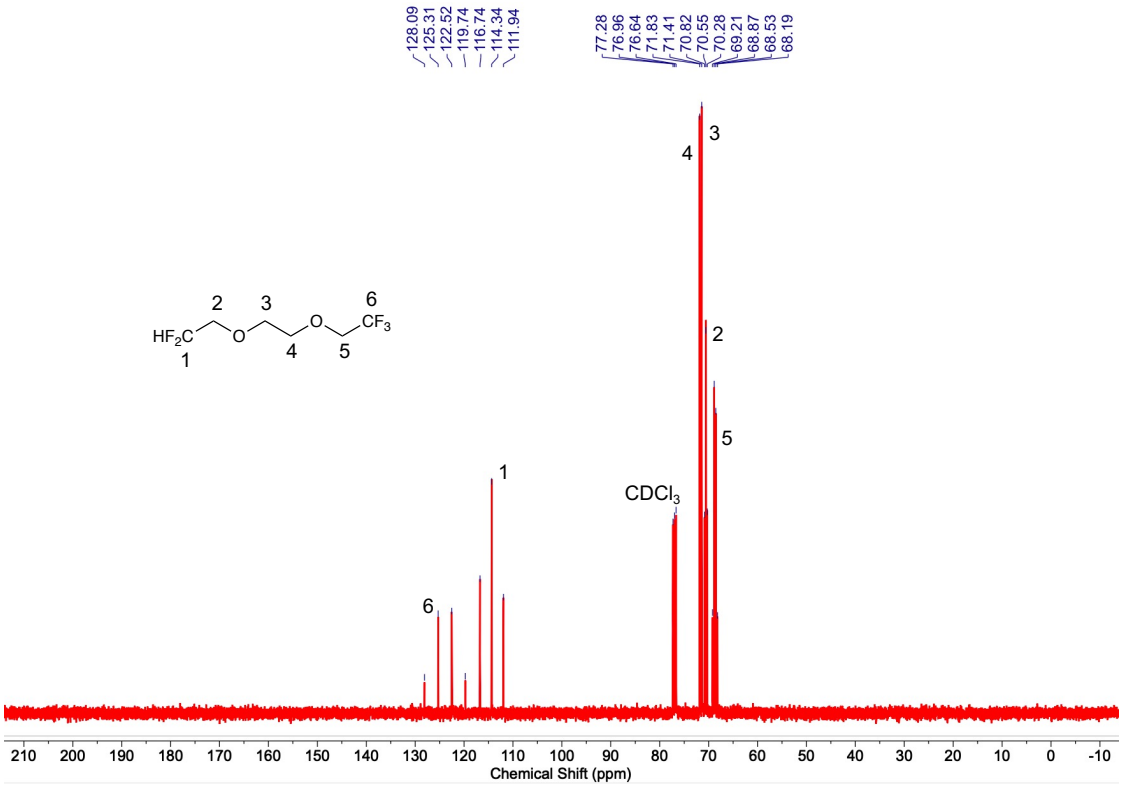

Supplementary Fig. 65. ^{13}C-NMR of F5DEE (100 MHz, $CDCl_3$, δ/ppm): 128.09 ~ 119.74, 116.74 ~ 111.94, 71.83, 71.41, 70.82 ~ 70.28, 69.21 ~ 68.19.

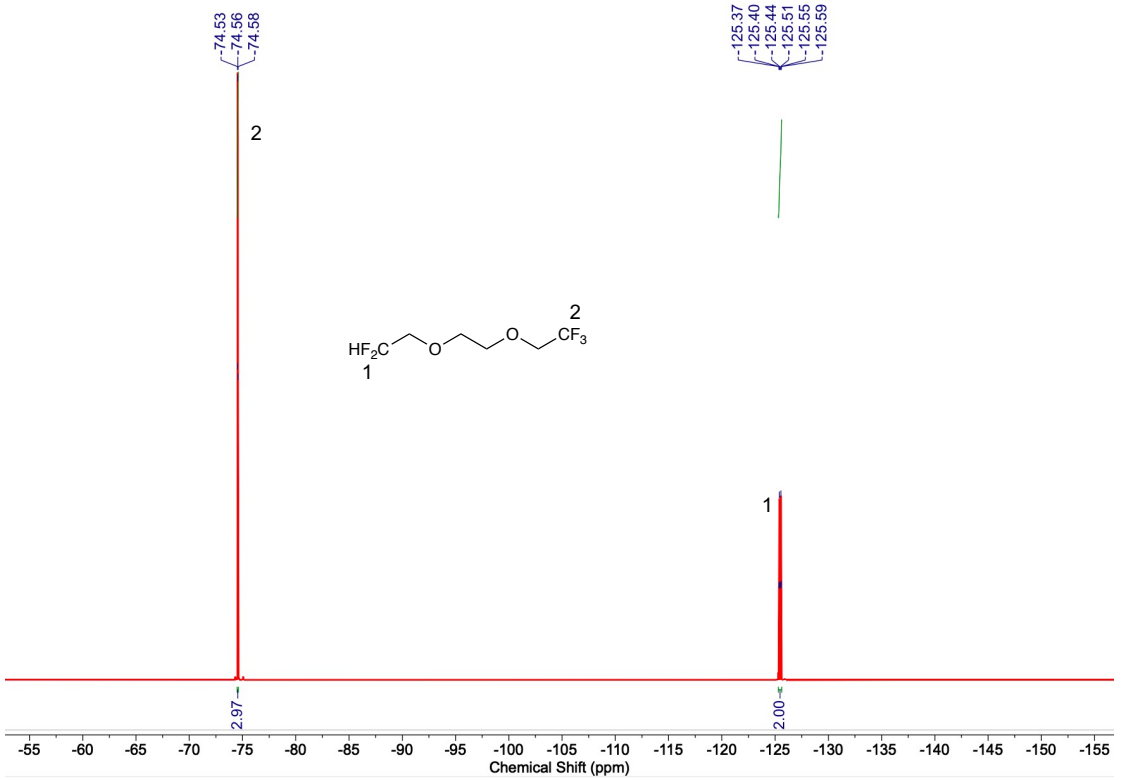

Supplementary Fig. 66. ^{19}F-NMR of F5DEE (376 MHz, $CDCl_3$, δ/ppm): –74.53 ~ –74.58 (t, 3F), –125.37 ~ –125.59 (dt, 2F).

3. Supplementary References

1. Yu, Z. *et al.* Molecular design for electrolyte solvents enabling energy-dense and long-cycling lithium metal batteries. *Nat. Energy* **5**, 526–533 (2020).
2. Su, C.-C. *et al.* Principle in developing novel fluorinated sulfone electrolyte for high voltage lithium-ion batteries. *Energy Environ. Sci.* **14**, 3029–3034 (2021).
3. Su, C.-C. *et al.* Solvating power series of electrolyte solvents for lithium batteries. *Energy Environ. Sci.* **12**, 1249–1254 (2019).
4. Suo, L. *et al.* Fluorine-donating electrolytes enable highly reversible 5-V-class Li metal batteries. *Proc. Natl. Acad. Sci.* **115**, 1156–1161 (2018).
5. Ren, X. *et al.* Localized High-Concentration Sulfone Electrolytes for High-Efficiency Lithium-Metal Batteries. *Chem* **4**, 1877–1892 (2018).
6. Chen, S. *et al.* High-Voltage Lithium-Metal Batteries Enabled by Localized High-Concentration Electrolytes. *Adv. Mater.* **30**, 1706102 (2018).
7. Fan, X. *et al.* Non-flammable electrolyte enables Li-metal batteries with aggressive cathode chemistries. *Nat. Nanotechnol.* **13**, 715–722 (2018).
8. Ren, X. *et al.* Enabling High-Voltage Lithium-Metal Batteries under Practical Conditions. *Joule* **3**, 1662–1676 (2019).
9. Cao, X. *et al.* Monolithic solid–electrolyte interphases formed in fluorinated orthoformate-based electrolytes minimize Li depletion and pulverization. *Nat. Energy* **4**, 796–805 (2019).
10. Cao, X. *et al.* Optimization of fluorinated orthoformate based electrolytes for practical high-voltage lithium metal batteries. *Energy Storage Mater.* **34**, 76–84 (2021).
11. Xue, W. *et al.* FSI-inspired solvent and "full fluorosulfonyl" electrolyte for 4 V class lithium-metal batteries. *Energy Environ. Sci.* **13**, 212–220 (2020).
12. Xue, W. *et al.* Ultra-high-voltage Ni-rich layered cathodes in practical Li metal batteries enabled by a sulfonamide-based electrolyte. *Nat. Energy* **6**, 495–505 (2021).
13. Zhang, W. *et al.* Engineering Wavy-Nanostructured Anode Interphases with Fast Ion Transfer Kinetics: Toward Practical Li-Metal Full Batteries. *Adv. Funct. Mater.* **30**, 2003800 (2020).
14. Li, S. *et al.* Synergistic Dual-Additive Electrolyte Enables Practical Lithium-Metal Batteries. *Angew. Chemie* **132**, 15045–15051 (2020).
15. Qian, J. *et al.* Anode-Free Rechargeable Lithium Metal Batteries. *Adv. Funct. Mater.* **26**, 7094–7102 (2016).
16. Qiu, F. *et al.* A Concentrated Ternary-Salts Electrolyte for High Reversible Li Metal Battery with Slight Excess Li. *Adv. Energy Mater.* **9**, 1803372 (2019).
17. Xu, R. *et al.* Design and Demystify the Lithium Metal Interface towards Highly Reversible Batteries. *Adv. Mater.* (2021) doi:10.1002/adma.202105962.
18. Hagos, T. T. *et al.* Locally Concentrated LiPF 6 in a Carbonate-Based Electrolyte with Fluoroethylene Carbonate as a Diluent for Anode-Free Lithium Metal Batteries. *ACS Appl. Mater. Interfaces* **11**, 9955–9963 (2019).
19. Weber, R. *et al.* Long cycle life and dendrite-free lithium morphology in anode-free lithium pouch cells enabled by a dual-salt liquid electrolyte. *Nat. Energy* **4**, 683–689 (2019).
20. Genovese, M. *et al.* Hot Formation for Improved Low Temperature Cycling of Anode-Free Lithium Metal Batteries. *J. Electrochem. Soc.* **166**, A3342–A3347 (2019).
21. Louli, A. J. *et al.* Diagnosing and correcting anode-free cell failure via electrolyte and morphological analysis. *Nat. Energy* **5**, 693–702 (2020).
22. Yu, Z. *et al.* A Dynamic, Electrolyte-Blocking, and Single-Ion-Conductive Network for Stable Lithium-Metal Anodes. *Joule* **3**, 2761–2776 (2019).
23. Jia, M. *et al.* Fluorinated Bifunctional Solid Polymer Electrolyte Synthesized under Visible Light for Stable Lithium Deposition and Dendrite-Free All-Solid-State Batteries. *Adv. Funct. Mater.* **31**, 2101736 (2021).

24. Wang, H. *et al.* Dual-Solvent Li-Ion Solvation Enables High-Performance Li-Metal Batteries. *Adv. Mater.* **33**, 2008619 (2021).

25. Zou, Y. *et al.* Interfacial Model Deciphering High-Voltage Electrolytes for High Energy Density, High Safety, and Fast-Charging Lithium-Ion Batteries. *Adv. Mater.* (2021) doi:10.1002/adma.202102964.

26. Aurbach, D., Gofer, Y. & Langzam, J. The Correlation Between Surface Chemistry, Surface Morphology, and Cycling Efficiency of Lithium Electrodes in a Few Polar Aprotic Systems. *J. Electrochem. Soc.* **136**, 3198–3205 (1989).

27. Adams, B. D., Zheng, J., Ren, X., Xu, W. & Zhang, J.-G. Accurate Determination of Coulombic Efficiency for Lithium Metal Anodes and Lithium Metal Batteries. *Adv. Energy Mater.* **8**, 1702097 (2018).

28. Meddings, N. *et al.* Application of electrochemical impedance spectroscopy to commercial Li-ion cells: A review. *J. Power Sources* **480**, 228742 (2020).

29. Guo, R. & Gallant, B. M. Li2O Solid Electrolyte Interphase: Probing Transport Properties at the Chemical Potential of Lithium. *Chem. Mater.* **32**, 5525–5533 (2020).

30. May, R., Fritzsching, K. J., Livitz, D., Denny, S. R. & Marbella, L. E. Rapid Interfacial Exchange of Li Ions Dictates High Coulombic Efficiency in Li Metal Anodes. *ACS Energy Lett.* **6**, 1162–1169 (2021).

31. Wang, H. *et al.* Efficient Lithium Metal Cycling over a Wide Range of Pressures from an Anion-Derived Solid-Electrolyte Interphase Framework. *ACS Energy Lett.* **6**, 816–825 (2021).